Electrolyte Design for All-Solid-State Lithium Metal Batteries

by

Qianyi Ma

A thesis

presented to the University of Waterloo

in fulfilment of the

thesis requirement for the degree of

Master of Applied Science

in

Chemical Engineering

Waterloo, Ontario, Canada, 2022

Author's Declaration

This thesis consists of material all of which I authored or co-authored: see Statement of Contributions included in the thesis. This is a true copy of the thesis, including any required final revisions, as accepted by my examiners.

I understand that my thesis may be made electronically available to the public.

Statement of Contributions

The body of this thesis is based upon a combination of published works and unpublished works.

Chapter 1, 2, 3, 4, 5 of this thesis of a review paper that was first-authored by myself, my supervisor, Dr. Zheng Yun, Dr. Dan Luo, Dr. Tyler Or, Yizhou Liu, Dr. Liexin Yang, Dr. Haozhen Dou, Jiequan Liang, Yihang Nie, Dr. Xin Wang, and Dr. Aiping Yu. I am the first author of this paper. I conceptualized study design and performed data collection and manuscript writing. My coauthors reviewed the manuscript and provided feedback on draft manuscript.

Ma, Qianyi, Yun Zheng, Dan Luo, Tyler Or, Yizhou Liu, Leixin Yang, Haozhen Dou et al. "2D Materials for All‐Solid‐State Lithium Batteries." *Advanced Materials* 34, no. 16 (2022): 2108079.

Chapter 6 is the research work in the current state which is not already published. I conceptualized study design and performed data collection and manuscript writing.

Chapter 7 of this thesis consists of some paragraphs from the research paper that I was co-authored with my supervisor, Dr. Leixin Yang, Dr. Dan Luo, Dr. Yun Zheng, Dr. Tingzhou Yang, Yihang Nie, Dr. Haozhen Dou, Dr. Yongguang Zhang, Dr. Rong Huang, Dr. Aiping Yu, Dr. Lingling Shui, Dr. Xin Wang, Dr. I am the co-author of these papers. In these works, I performed with cathode preparation, electrochemical tests and non–destructive synchrotron X–ray tomography analyses and involved in the writing of the manuscript.

Yang, Leixin, Dan Luo, Yun Zheng, Tingzhou Yang, Qianyi Ma, Yihang Nie, Haozhen Dou et al. "Heterogeneous Nanodomain Electrolytes for Ultra‐Long‐Life All‐Solid‐State Lithium‐Metal Batteries." *Advanced Functional Materials* (2022): 2204778.

Abstract

Although one of the most mature battery technologies, lithium-ion batteries still have many aspects that have not reached the desired requirements, such as energy density, current density, safety, environmental compatibility, and cost-effectiveness. To solve these problems, all-solid-state lithium batteries (ASSLB) based on lithium metal anodes with high energy density and safety have been proposed and become a research hotspot in recent years. Due to the advanced electrochemical properties of two-dimensional materials (2DM), they have been applied to mitigate some of the current problems of ASSLBs, such as high interfacial impedance and low electrolyte ionic conductivity. In this work, the background and fabrication method of 2DMs are reviewed initially. The improvement strategies of 2DMs are categorized based on their application in the three main components of ASSLBs: The anode, cathode, and electrolyte. Finally, to elucidate the mechanisms of 2DMs in ASSLBs, the role of in-situ characterization, synchrotron X-ray techniques and other advanced characterization are discussed.

Acknowledgements

I would like to express my sincere gratitude to my supervisor, Professor Zhongwei Chen, for his support, motivation, guidance, and advice during my MASc studies. I would also like extend thanks to my MASc exam committee members, including Professor Ali Elkamel, and Professor Eric Croiset from the University of Waterloo, for their valuable time and insights.

I would also like to thank all the group members who were always there to help in my project. I also received help from my colleagues who include, but are not limited to, Dr. Dan Luo, Qiao Cu, Dr. Zhen Zhang, Dr. Leixing Yang, Dr. Haozhen Dou, Dr. Rui Gao, Dr. Xin Wang, and Dr. Yun Zheng. Thanks a lot for all your help and support in the past four years. Moreover, I would like to acknowledge my parents, family members, and friends. I am grateful for their unconditional love, support, and sacrifice.

Finally, I would like to mention my gratitude to the Natural Science and Engineering Research Council of Canada (NSERC), the Waterloo Institute for Nanotechnology, and the University of Waterloo for their financial support.

Table of Contents

List of Figures

List of Abbreviations

LIB	Lithium-ion battery
ASSLB	All-solid-state lithium battery
2DM	Two-dimensional material
CEI	Cathode-electrolyte interface
SEI	Solid-electrolyte interface
GO	Graphene oxide
rGO	Reduced graphene oxide
TMC	Transition metal chalcogenides
BN	h-boron nitride
COF	Covalent organic framework
LDH	Layered double hydroxides
CVD	Chemical vapor deposition
BNNS	2D boron nitride nanosheet
LATP	$Li_{1.3}Al_{0.3}Ti_{1.7}(PO_4)_3$
GF	fluorinated graphene
CZTS	Cu_2ZnSnS_4
Li_xVS_2	lithiated VS_2
PEO	polyethylene oxide
PAN	poly(acrylonitrile)
PVDF	poly (vinylidene fluoride)
MOF	metal−organic framework
XRD	X-ray Powder Diffraction
SEM	Scanning Electron Microscopy

XPS	X-ray photoelectron spectroscopy
TEM	Transmission electron microscopy
NMR	Nuclear Magnetic Resonance
XANES	X-ray near-edge absorption structure
EXAFS	Extended X-ray absorption fine structure
CV	Cyclic voltammetry
EIS	Electrochemical impedance spectroscopy
NMP	N-Methyl-2-pyrrolidone
EDX	Energy dispersive X-ray spectroscopy
HNE	Heterogeneous nanodomains electrolyte
SPE	Solid polymer electrolyte
EO	Ether oxygen
Pebax	Poly(ether-block-amide)
PA	Polyamide
NMC 811	$LiNi_{0.8}Mn_{0.1}Co_{0.1}O_2$
LFP	$LiFePO_4$
SAXS	Small-angle X-ray scattering
LSV	Linear sweep voltammetry
FT-IR	Fourier-transform infrared spectroscopy
Li-ion	Lithium ion
EV	Electric vehicles

Chapter 1

1. Introduction

1.1 Introduction of all-solid-state lithium battery

The lithium battery is one of the most important energy storage technologies, which has been widely studied and applied in electric vehicles (EVs), portable electronic devices, and other energy storage products due to their unique advantages including light weight, high specific energy density, and long cycle life.[1–3] However, further development of traditional liquid electrolyte-based lithium batteries is limited due to some shortcomings. The typical organic electrolyte material used in current commercial lithium batteries is flammable and prone to explosion.[4,5] Once a lithium battery generates heat due to long-term operation or damage to its internal structure, organic electrolysis can lead to combustion and explosion.[6] Besides, due to the characteristics of the electrolyte liquid state, the growth of lithium dendrites is likely to occur, resulting in the explosion of lithium batteries due to short circuits.[7–9] Moreover, the electrolyte solution can generate side reactions and affect the reversible capacity and stability of the battery.[10]

In order to relieve or even completely solve these problems, solid state electrolytes (SSEs) without any liquid composition in the electrolyte have been proposed and implemented in lithium batteries, which are called all-solid-state lithium batteries (ASSLBs).[11] Compared with the liquid electrolyte based batteries, ASSLBs have some unique advantages, including inherently non-flammable, sufficient mechanical strength to well suppress lithium dendrites, and good chemical stability to effectively reduce side reactions.[12–14] Besides, the long-term electrochemical and thermal stabilities, as well as

the energy density can be further improved by using lithium metal anode in an ASSLB system.[15] Nevertheless, despite the merits of solid-state batteries, there are still some challenges or some key points need to be considered to widely extend the practical application of ASSLBs.[16–19]

To be specific, with the application of the lithium metal anode, the side reactions between the SSEs and lithium metal anode cannot be ignored, which will result in failure of the lithium anode. Moreover, lithium dendrite protrusions from the anode can cause a short circuit thus should be suppressed. Moreover, the high interfacial resistance between the anode and SSE should be addressed.[20–23] In the cathode side, the low lithium ionic conductivity, poor electronic conductivity, and high interfacial resistance between electrolyte and cathode will limit the specific capacity of active materials during charge and discharge process. Second, the volume change of active materials during operation process will reduce the solid-solid interface contract.[24–26]

In the electrolyte, low ionic conductivity in SSEs is one of the limitations of ASSLBs especially for polymer-based SSEs such as polyethylene oxide (PEO). Meanwhile the mechanical strength of SSEs is one of the key parameters to suppress the growth of lithium dendrites.[27–29] The last serious problem is the mechanical stability of the entire solid-state lithium battery. During the charging and discharging process, the cathode and anode material of the lithium battery's volume will change. Because it is a solid material, it produces irreversible deformation, resulting in poor contact between the electrode and the electrolyte.[30–33]

1.2 The application of two-dimensional materials for all-solid-state lithium battery

To solve the above-mentioned issues and further improve the electrochemical

performance of ASSLBs, various advanced materials and structures have been developed in recent years. Among those advanced materials, two-dimensional materials (2DMs) comprised of a single layer of atoms have become a prominent research topic due to their outstanding electrical, electrochemical, thermal, and mechanical properties.[34–36]

To be specific, in the anode side, due to the high chemical stability of 2DMs, 2DMs are applied to alleviate side reactions between the lithium metal anode and electrolyte. In order to deal with the poor interface contract between the anode and electrolyte, 2DMs with high lithium ionic conductivity can be used to form a solid electrolyte interface to reduce the interface resistance and suppress the growth of lithium dendrites.[37,38] In the cathode side, the high specific surface area of 2DMs will enhance the cathode active material loading mass and energy density of ASSLBs.[39] The defect engineering in 2DMs will provide various catalytic active site for active material transformation during charging/discharging process, which is especially necessary for all-solid-state Li-S battery solid phase catalysis.[40] The remarkable electron conductivity of 2DMs can enhance the poor electron conductivity of some active materials to fully utilize the theoretical capacity.[41,42] As for the electrolyte, the high mechanical properties of 2DMs will enhance the mechanical strength of SSEs, especially polymer-based SSEs to suppress the growth of lithium dendrites and extend the cycle life of ASSLBs. Due unique properties of 2DMs, it will provide or enhance the lithium ionic conductivity of SSEs. On the one hand, high specific surface area can provide extra lithium ionic conductivity channel to enhance the lithium transport. On the other hand, for the polymer-based electrolyte, the addition of the 2DMs can reduce the crystallinity of the polymer electrolyte itself to reduce the grain boundary resistance to promote lithium ion transport.[43–45]

Since the discovery of graphene in 2004, various 2DMs have been developed and applied to lithium battery technology, used in electrode materials and electrolytes. In recent years, 2DMs have been continuously applied to ASSLBs and gradually become a research hotspot, however, to the best of our knowledge, there is still no comprehensive summary for 2DMs in ASSLBs. As shown in Figure 1, the fundamentals of 2DMs used in ASSLBs including the material classification and synthetic strategies will be first discussed in detail.[46] Then, the latest research progress of 2DMs in material design of ASSLBs will be reviewed systematically, which involves the electrodes, electrolyte, and their interfacial regions. Additionally, a few emerging advanced characterization technologies will be discussed that deepen the understanding of the structure-function relationship in 2DMs for ASSLBs.[47–49] Finally, future research directions are proposed to accelerate the technology developments, from the fundamental understanding of mechanisms to the improvement of materials and applications.

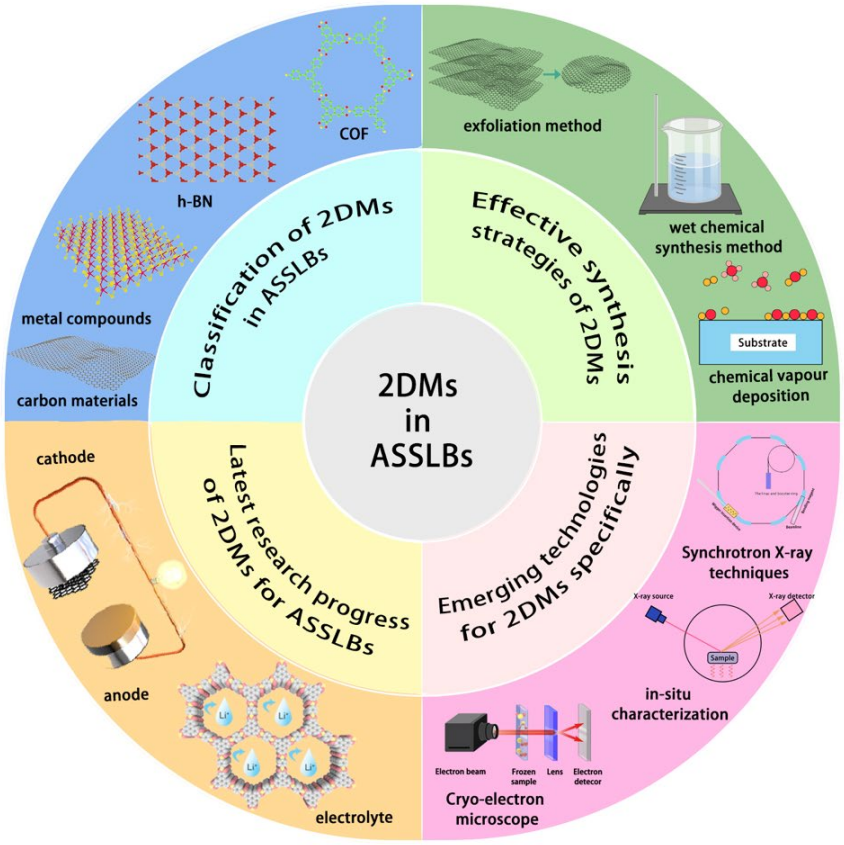

Figure 1. The application of 2DMs in ASSLBs

Chapter 2

2. Fundamentals of 2DMs for ASSLBs

2.1. Classification of 2DMs used in ASSLBs

Different element compositions will have different effects on the properties and structure of 2DMs. Accordingly, 2DMs are divided into the following categories: carbon-based materials, metallic material, and other 2DMs (Figure. 2). In this section, the characteristics, and properties of different kinds of 2DMs will be explained.

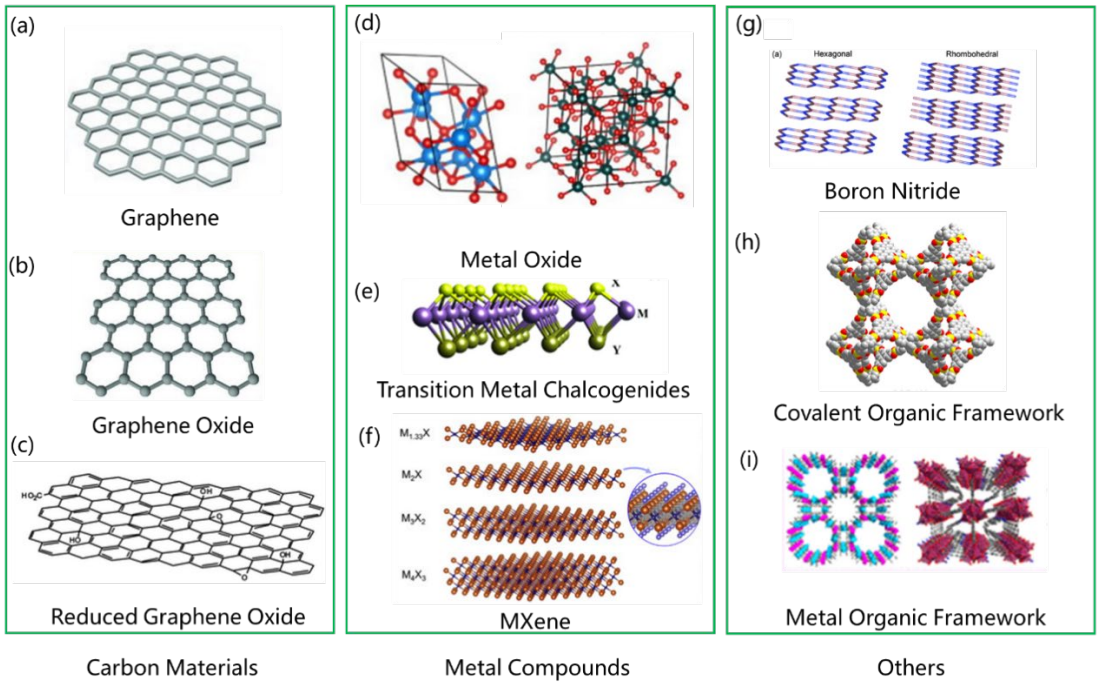

Figure 2. Classification of 2DMs in ASSLBs (a) graphene. Reproduced by permission.[50] Copyright 2012, Wiley-VCH. (b) graphene oxide. Reproduced by permission.[51] Copyright 1998, American Chemical Society. (c) reduced graphene oxide. Reproduced by permission.[52] Copyright 2011, Royal Society of Chemistry. (d) metal oxide. Reproduced by permission.[53] Copyright 2021, Elsevier. (e) transition metal chalcogenides.

Reproduced by permission.[54] Copyright 2018, Wiley-VCH. (f) MXene. Reproduced by permission.[55] Copyright 2020, Elsevier. (g) boron nitride. Reproduced by permission.[56] Copyright 2014, Royal Society of Chemistry. (h) covalent organic framework. Reproduced by permission.[57] Copyright 2015, American Chemical Society. (i) metal organic framework. Reproduced by permission.[58] Copyright 2020, American Chemical Society.

2.1.1 Carbon materials

2D carbon materials especially graphene, GO, rGO, et al. have attracted significant interest due to their large specific surface area, low cost, rich resource, high electrical conductivity, and great biocompatibility. These new carbon materials have many excellent physical and chemical properties and are widely used in many fields, especially in the electrochemical field showing their unique advantages.[59] Especially for the application of electrode materials, two-dimensional carbon materials have more unique applications. For specific, the large surface area, and high electrical conductivity can enhance the uniform electron distribution in the electrode structure. Low cost and rich resource can extend the field of the usage of the 2DMs. Biocompatibility can deal with the high interface resistant between electrolyte and electrode.

Graphene was the first discovered and developed 2DM, which is a single layer of graphite comprised of sp^2-hybridized carbon atoms arranged in a hexagonal lattice.[60–62] Based on its special structure, graphene has desirable electrochemical properties like high electrical conductivity, high specific surface area, broad electrochemical window, and high reversible Li storage capacity.[63] In ASSLBs, graphene is used as an artificial SEI or

cathode-electrolyte interface (CEI) for greater interface contract, and as a conductive material for the anode and cathode.[64] Graphene oxide (GO) and reduced graphene oxide (rGO) are the relevant materials for graphene, which has similar properties. In ASSLBs, it is applied to provide extra electronic and ionic transport channel, and deal with the interface problem as CEI.[65–67]

2.1.2 Metal compounds

Metal compounds are a major portion of inorganic materials applied in ASSLBs that can be divided into three main parts. Metal oxides are often used as cathode materials with high specific capacity and are widely studied. Therefore, the research of metal oxides in the electrochemistry has always been one of the major directions. For 2D metal oxides, such as MnO_2, Co_3O_4, V_2O_5, Li_xMnO_4, each atom within a layer is connected by covalent bonds, while each layer is connected by van der Waals forces.[68] The composition of each layer is metal-oxygen clusters and by sharing corners, edges and few faces to carry out expansion structure assembly.[69] The covalent bonds and atomic thickness provide the 2D metal oxides some unique properties such as excellent mechanical strength, high active surface, optical transparency, and flexibility.[70,71] Moreover, when 2D metal oxides are arranged in 3D structure, 2D metal oxides strengthen the materials' ability to contain large ions like Li^+.[72,73] In the cathode, metal oxides are used as active material to provide high theoretical capacity and greater interface contract. In the electrolyte, they provide higher mechanical strength and ionic conductivity as the one of electrolyte components.

With the development of the Li-S battery, research in transition metal chalcogenides (TMCs) has gradually become one of the hotpots, as a result, TMC has been studied and

applied in ASSLBs. TMCs such as MoS_2, FeS, TiS_2, Fe_3S_4, VS_2, VS, are a chemical species obtained by the combination of chalcogenide anions with metals.[74] Due to its tunable stoichiometric compositions, unique crystal, rich redox sites, and high electrical conductivity, TMCs attract interest as potential materials for energy storage devices and electrode materials.[75,76] Because of the more lithium insertion/deinsertion site with the high specific surface area, TMCs have higher theoretical special capacity compared with graphite.[77,78] In addition, 2D TMCs are used as the active material in cathode to provide high theory capacity, suppress the side reaction between electrode and electrolyte (especially sulfide-based and oxide-based electrolyte), reduce the percent of crystal region and provide extra lithium transport channel to enhance ionic conductivity. Moreover, when TMCs are used in sulfur-cathode ASSLBs, the "shuttle effect" will be suppressed because the nano-structured TMCs as a polar host can provide stronger affinity with soluble polysulfides, which is because of the polar sulfiphilic surface of TMCs, so that ASSLBs have higher sulfur utilization rate and long cycle life.[79,80]

MXene is one of the newer kinds of 2D transition metal carbides/nitrides. Due to their terminal groups, MXenes are hydrophilic, which is different from most 2DMs. For ASSLBs, with the application of MXene, the terminal group can enhance the interaction between polymer chains and MXene to improve the ionic conductivity of electrolyte.[69]

2.1.3 Other 2DMs

h-boron nitride (BN), one of the forms of BN, is a two-dimensional material with the same structure as graphene, where the carbon position in the graphene is alternatingly replaced by an equal number of B and N atoms.[81,82] In recent work, h-BN is widely

focused on due to its unique properties. First, compared with the graphene, h-BN shows excellent stability in high temperature without the decrease of the layer thick.[83] Second, due to the perfect single atomic layer structure of h-BN, it has excellent high mechanical strength to suppress the growth of the lithium dendrites.[84] Third, h-BN has larger thermal conductivity compared with the bulk h-BN, because when the thickness of the material is scaled down, the phonon-phonon scattering decreases.[85] Moreover, it has chemical inertness, which can help keep it stable against chemicals like Li metal and oxygen.[84,86] Based on its unique properties for SEs, h-BN is used as an additive in PEO to provide extra lithium-ionic transport channels, reduce the crystallinity, and enhance mechanical strength. It also used to suppress side reactions, improving the interfacial contact between the electrode and electrolyte.[87–89]

As the core of energy materials, porous materials are under constant development, where covalent organic framework (COF) has been designed as one of the new porous materials. 2D COF is one kind of porous polymer nanosheets which have highly crystalline structures, tunable function, and high charge-carrier transfer ability.[90] Two-dimensional sheets are held together by covalent bonds that constitute the structure of 2D COFs, which are stacked together by non-covalent forces.[91–93] By regulating the types of functional groups, COFs are used individually or as one of the part of electrolyte to transport lithium ions in ASSLBs.[94]

Similar with COFs, as a new generation of materials, 2D MOFs are receiving increasing attention due to their high surface area, structural diversity and high adsorption site density.[95] The metal sites and organic linking groups in MOFs have high chemical bonding and high activity with LiPSs.[96] Through the metal-ligand coordination covalent bond, the active organic substance can be immobilized.[97] In fact, many MOFs can

significantly increase the battery capacity retention capacity of lithium batteries. The ion and electron transport in the framework are significantly improved due to application of the porous structure and electrical conductivity of MOFs in solid electrolytes.[98,99]

2.2 Effective synthesis strategies of 2DMs

The discovery of graphene immediately made the research of 2DMs the center of materials research. The research on 2DMs with excellent electrochemical properties has gradually become a potential material for the next generation of high-performance ASSLBs.[100] The approaches to prepare various 2DMs can be divided into three parts: (1) exfoliation method (2) chemical vapor deposition (3) wet chemical synthesis method.[101,102]

2.2.1 Exfoliation methods

Exfoliation method is one of the major methods to fabricate the 2DMs. The mechanism of exfoliation method is to weaken the interaction between nanosheets' layers. Based on the mechanism, the exfoliation can be divided into some parts, such as interaction-assisted expansion and exfoliation, mechanical force-assisted exfoliation and exfoliation of layered materials containing ions or molecules between the layers, etc.[103,104]

Intercalation-assisted expansion is one of the methods to weaken the interaction between layers using various intercalation agents (Figure. 3a). Oxidation-based intercalation and reduction-based intercalation method are two major methods to achieve intercalation. Oxidation-based intercalation and exfoliation method involves using strong

oxidative agents to intercalate the host gallery of layered materials, which can expand the interlayer spacing of the material to prepare 2DMs such as GO, graphene, h-BN etc. The main exfoliation conditions can be divided into two kinds with different advantages. One is that by the usage of normal oxidation agents such as $KMnO_4$, KNO_3, and concentrated H_2SO_4, where production in this condition will be scalable and rich with functional groups. Another one is in the gas phase intercalation using other oxidation agents such as halogen intercalants, metal halides, halides, and super strong oxidizers. The production in this condition will well preserve the in-plate structure and control the intercalation stage. Reduction-based intercalation and exfoliation method involves the assistance of reduction reactions to prepare 2DMs such as metal chalcogenides, graphene, h-BN. The main exfoliation conditions can be divided into four types and each one has its own advantages. [105] First, the fabrication process in the vacuum condition by gas intercalation of pure alkali metals can prepare TMCs with good conductivity and high percentage of metallic phase with high monolayer yield. Second, the fabrication process is in the liquid phase condition such as n-BuLi, hexane solution, or naphthalide, which can produce TMCs with tunable percentage of metallic phase, semi-conductivity, and high monolayer yield. Third, 2DMs can be fabricated by electrochemical intercalation of lithium ions. Reduction-based intercalation and exfoliation based on this condition is safe and suitable for most 2DMs fabrication process. Fourth, in polar aprotic organic solvents conditions, alkali metal atoms are applied to weaken the interaction between layers to produce 2DMs, which is widely applicable for most 2DMs, and easy for assembly without the help of external forces.[106,107]

Mechanical force-assisted exfoliation is one of the fabrication methods to produce 2DMs, which uses external forces to break the internal interaction force between layers.

It can be divided into several approaches, such as sonication assisted-exfoliation and shear force-assisted liquid phase exfoliation (Figure. 3b), ball milling-assisted exfoliation (Figure. 3c), ion exchange-assisted exfoliation, etching and intercalation-assisted exfoliation, etc. The mechanism of sonication assisted-exfoliation and shear force-assisted liquid phase exfoliation is to match the surface energy between the layers to separate it, higher energy to increase the yield and produce 2DMs with well persevered structure and scalable size, such as graphene, h-BN, MoS_2, metal oxide, MOFs, etc. To prepare large quantities 2DMs, ball milling is used to exfoliate layer materials, in which the mechanism is based on a shear force parallel to the layers to weaken the interaction between layered materials. It is also used to produce scalable materials with low cost and large quantities, such as graphene, h-BN, MoS_2.[108,109]

With the assistant of ions and molecules to weaken the interlayer interaction between materials, some special 2DMs can be prepared. It can be divided into two parts, one is ion exchange-assisted exfoliation, another one is etching and intercalation-assisted exfoliation. To deal with produce 2DMs that are difficult to exfoliate by the application of oxidation or reduction agents, ion exchange-induced intercalation is applied. To mute the electronic interaction between layers with protons, anionic ions is exchanged with proton to produce 2DMs which are monolayers, with high yield and intrinsically charged sheets, such as layered double hydroxides (LDH). Based on the similar mechanism, the 2DMs which has strong bond between layers such as MXene should be prepared by etching with HF or other organic bases. The production of this method is water soluble and this method is suitable to many materials.[110,111]

2.2.2 Chemical vapor deposition

Chemical vapor deposition (CVD) is a technology with a long history and one of the most common technologies to produce 2DMs, which is traditionally used for the preparation of high-quality thin films, such as W, Ti, Ta, Zr, and Si on substrates (Figure. 3d).[112] Here, the researchers use CVD to produce single crystal graphene as an example to briefly introduce this technology. The key point in this regard is the need to anneal under relatively high temperature hydrogen, so that the grains are quickly deposited on the substrate and inhibit normal CVD growth. The specific production conditions are hydrogen, methane and argon as gas conditions, copper foil as a substrate and catalyst, and hydrogen as a cocatalyst, and then single crystal graphene is produced by the CVD process.[113–116] In recent years, 2DMs such as silicene, borophenes, h-BN nanosheets, are always produced by CVD. In addition, compared with other methods, CVD method can fabricate 2D heterostructures. CVD procedures have been used to fabricate both vertical and lateral heterostructures.[117] Vertical heterostructures are mainly synthesized by the following techniques: two-dimensional crystal growth, vapor-solid reactions, and van der Waals epitaxy. Based on its controllable thickness of 2DMs, some micro-ASSLBs have been fabricated by this method.[118,119]

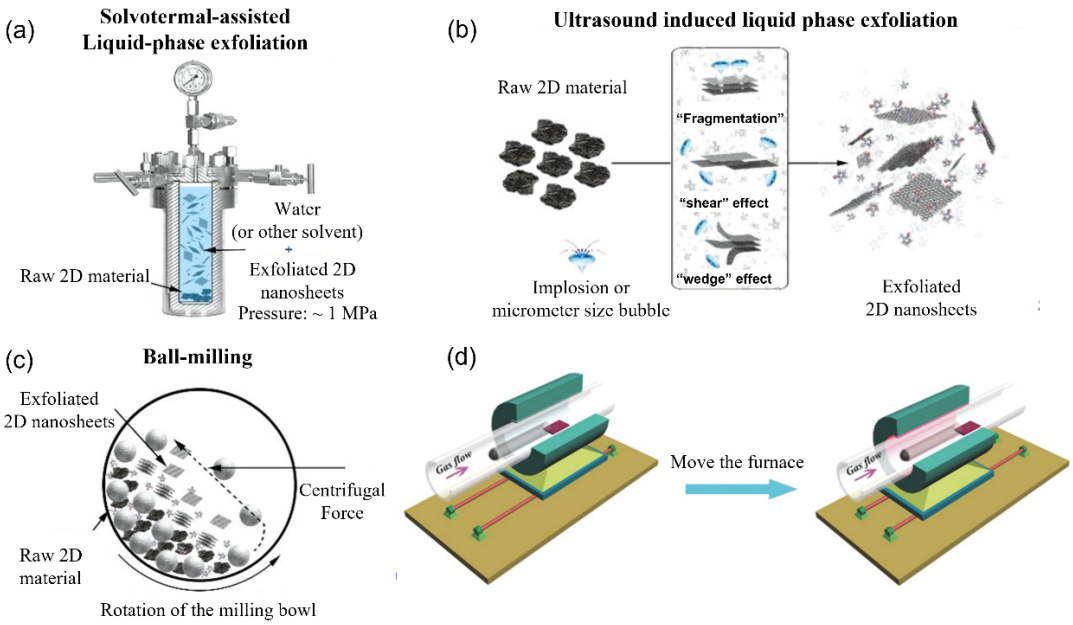

Figure 3. (a) solvothermal-assisted liquid-phase exfoliation; (b) ultrasound induced liquid-phase exfoliation; (c) ball-milling. Reproduced by permission.[120] Copyright 2019, Wiley-VCH. (d) chemical vapor deposition for 2DMs. Reproduced by permission.[121] Copyright 2018, Wiley-VCH.

2.2.3 Wet chemical synthesis method

Wet chemical synthesis is a low-cost method that can effectively synthesize several types of carbonaceous and non-carbonaceous 2DMs. The chemical synthesis process is a bottom-up approach in which atoms/molecules are deposited on the substrate and a two-dimensional layered structure is formed through a step-by-step deposition process. Although solvent stripping has been well optimized and is commonly used to synthesize two-dimensional nanostructures, chemical synthesis methods are still under active investigation for further optimization. Basically, these are wet chemistry methods, which react chemically and deposit onto substrates to produce two-dimensional

nanostructures.[102,107]

Chapter 3

3 Research progress of 2DMs used in ASSLBs

3.1 2DMs in electrodes design for ASSLBs

In order to meet the performance requirements of materials used in ASSLBs, 2DMs have been introduced into various components of ASSLBs, which includes electrodes, electrolyte, and their interfacial regions. The latest research progress of 2DMs in electrode design of ASSLBs is summarized systematically in this section.

3.1.1 Anode

The anode is one of the key compositions of ASSLBs. Compared with conventional Li ion batteries, requirement of the anode in ASSLBs is higher and more complex. Beside excellent porosity, great chemical stability with electrolytes, light weight, good durability, low cost, voltage match with preferred cathode, good conductivity, high theoretical capacity and high irreversible capacity, the interface resistance between anode and different type of electrolytes also needs to be considered. Since lithium metal itself has high activity, it will inevitably produce side reactions with the electrolyte, which will increase the interface resistance. In addition, suppressing the growth of lithium dendrites is another serious problem. For Li metal batteries, the uniform deposition of lithium not only improve the coulombic efficiency but also deal with interface contract problem.[122] In this article, the method to develop the anode is to modify the surface of anode or composite electrode by using 2DMs.

3.1.1.1 Graphene

Graphene is a promising electrode material in lithium-ion batteries due to its high conductivity (~10^6 S cm^{-1}), high specific surface area (~2630 m^2 g^{-1}) and high lithium capacity.[66,123] In general, the research of graphene in ASSLBs anode can be divided into two main categories: 1. Anode active material 2. Current collector. According to its feature and function, graphene can be used as high-performance anode for high energy density ASSLBs due to its stratified structure, low mass, and superior electronic conductivity by methods like magnetron sputtering CVD. In this regard, Jie Lin et al. deigned a micro ASSLBs based on pure graphene anode where the electrolyte is LiPON and the cathode is $LiCoO_2$. A thin graphene anode layer was grown via CVD and subsequently sputtered with the electrolyte and cathode layers to obtain a 600 nm thick ASSLB with high energy density.[124] Di Wei et al. also use CVD method to grow a monolayer graphene onto the surface of Cu to fabricate ASSLBs, in which its energy and power density reaches 10 W h L^{-1} and 300 W L^{-1} respectively.[66]

On the other hand, due to its high affinity with lithium metal, graphene can be used to modify the surface of Cu to improve the uniform deposition of lithium metal in the anode and the interfacial contact between the anode and electrolyte. For instance, Shaobo Huang et al. applied vertical graphene on 3D commercial copper mesh to improve the uniformity of lithium deposition, which is due to the dual 3D structure and defects in the vertical structure (Figure. 4a). Uniform lithium deposition and nuclear growth can be verified by XPS and EDS methods. As a result, the assembled ASSLBs with 3D Cu/graphene structure anode shows better cycle stability and lower polarization.[125]

3.1.1.2 BN

Boron nitride (BN) has similar properties with graphite. It has high chemical and mechanical stability and low electronic conductivity. As a result, the major applications of BN in ASSLBs can be divided into two parts.[126,127] One is to improve the interface contract between the anode and electrolyte due to its high ionic conductivity and low electronic conductivity, where the low electronic conductivity can suppress the growth of lithium. Jiayun Wen et al. applied 2D boron nitride nanosheets (BNNS) with Li metal to make a composite anode to improve the interface contact between Li metal anode and solid electrolytes (Figure. 4b). Only 5 wt% BNNS can significantly improve the mechanical contact between Li metal and garnet-type SSE. As a result, the interfacial resistance is only 9 Ω cm^{-2} which is much lower than without BNNS (560 Ω cm^{-2}). In addition, by using BNNS, the electrochemical plating and striping process is stable for 380 hours and shows a high critical current density of 1.5 mA/cm^2.[126] Another approach is to use BN as anode protection layer to suppress side reactions between the electrolyte and lithium anode due to its high mechanical and chemical stability. For example, Qian Cheng et al. coated the BN on the anode surface to protect the $Li_{1.3}Al_{0.3}Ti_{1.7}(PO_4)_3$ (LATP) solid electrolyte from reaction with lithium metal by CVD (Figure. 4c). In addition, Li|Li symmetrical cell with 1-2 mm of PEO polymer electrolyte at the Li/BN interface shows 500 hours of cycle life at 0.3 mA cm^{-2}. The solid-state batteries fabricated with Li|LATP/BN/PEO|$LiFePO_4$ retains 96.6% capacity after 500 cycles (Figure. 4d). By the application of in-situ TEM and cross-sectional SEM, during the charge and discharge process, there is no structural change with the LATP/BN particle, which indicates no side reaction between the LATP and Li anode.[127]

3.1.1.3 2D MoS_2

MoS_2 has low electronic conductivity, high ionic conductivity, and high selective ion transport, which is suitable to be used as the protection interface on the surface of lithium anode to prevent the direct contact between the anode and cathode. For example, Abdulkadir Kızılaslan et al. applied 2D MoS_2 as the protective interface to replace the bilayer solid electrolyte design in ASSLBs. By the application of MoS_2, the ASSLBs exhibits 675.8 mA h g^{-1} initial capacity and 584.1 mA h g^{-1} final capacity at 0.4 mA cm^{-2}, and after 200 cycles, MoS_2 ASSLBs fade by 13.58% while ASSLBs without MoS_2 fade 27.3% (Figure. 4e).[128,129]

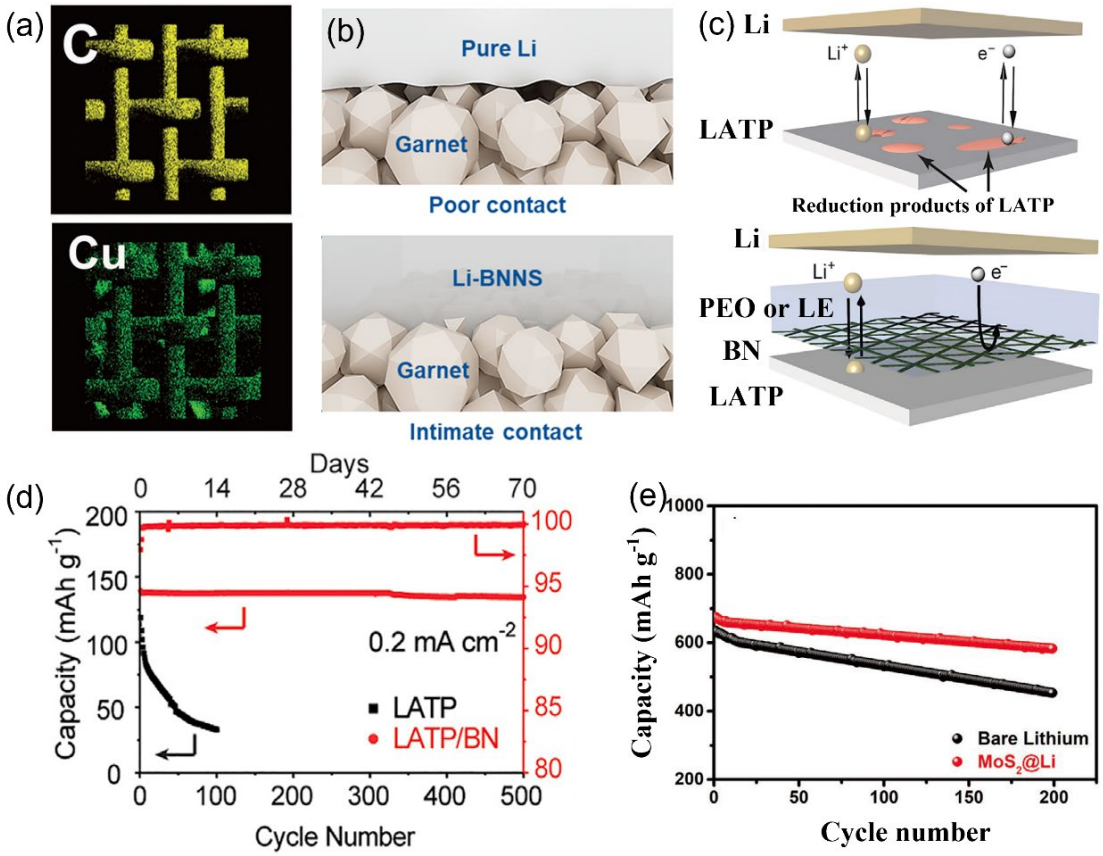

Figure 4. (a) 3D Cu/Graphene 3D current collector. Reproduced by permission.[125] Copyright 2019, Wiley-VCH. (b) BNNS/Lithium metal composition anode. Reproduced

by permission.[126] Copyright 2019, American Chemical Society. (c) BN-based anode protection SEI; (d) cycling performance of Li|PEO/LATP|LFP cells with and without BN coating. Reproduced by permission.[127] Copyright 2019, Elsevier. (e) Cycling performance of Li|MoS_2/$Li_7P_3S_{11}$|S cell. Reproduced by permission.[128] Copyright 2019, Wiley-VCH.

3.1.2 Cathode

The cathode is a key component of ASSLBs and the interfacial contact between the cathode and electrolyte is also an essential challenge in ASSLBs. Ionic diffusion is influenced by the poor interface contract between the electrode and electrolyte. Due to the volume change of active materials during the lithiation and delithiation process, physical degradation occurs which will cause increased interface resistance, heterogeneous ion transport, and poor mechanical contact. In order to deal with these problems, 2DMs are used in ASSLBs.[130]

3.1.2.1 Graphene relevant

(1) Graphene

Due to the excellent electrochemical properties and the layered structure of graphene, it is one of the most promising materials for the cathode of ASSLBs. The major effects of graphene can be divided into three parts.

First, due to the high specific surface area and flexibility of graphene, it is used to modify the surface of cathode to improve the surface contract with solid electrolytes. For

instance, Yingxiang Li et al. use electrochemical pre-lithiation to construct a LiF/graphene inorganic composite interface on the interface between cathode and garnet electrolyte, which is in-situ converted from fluorinated graphene (GF) and the cathode materials (Figure. 5a). Graphene is used to improve the surface mechanical contact between LiF and the garnet electrolyte. The effect of LiF is to enhance the transport of Li-ions in the cathode side due to its high chemical/thermal stability and low surface diffusion. Li|garnet/ICI|$LiFePO_4$ ASSLBs were tested at 0.05 C at 60 ˚C, which retains 90% capacity after 60 cycles, indicating that the LiF/graphene inorganic composite interface can improve interface issues between the cathode and garnet.[131]

Second, because graphene has high electronic conductivity, graphene is used to enhance the electronic conductivity, which is similar to the application of graphene in the anode of ASSLBs. Liangting Cai et al. used $CuCo_2S_4$/graphene/10%$Li_7P_3S_{11}$ as the cathode for high performance ASSLBs (Figure. 5b). $Li_7P_3S_{11}$ is coated to deal with the contact problem between the cathode and electrolyte, while graphene is used to improve the electronic conductivity. The combination of $CuCo_2S_4$ and graphene is to balance the electronic and ionic conductivities. The ASSLBs with composite cathode yields 556.41 mA h g^{-1} reversible capacity at 500 mA g^{-1} after 100 cycles, which shows great cycling stability and high performance.[132] In order to fully present the ability of graphene to construct a 3D ionic and electronic network, Hongli Wan et al. designed Cu_2SnS_3/graphene/$Li_7P_3S_{11}$ nanocomposite cathodes, where Cu_2SnS_3 nanoparticles are evenly distributed in graphene nanosheets (Figure. 5c). The major effect of graphene is to ensure the high electronic conduction of cathode. The nanoparticles and nanosheets contribute to the high electron and ionic conductivities which enable high energy density in ASSLBs and reduce the volume change to extend the cycle life of ASSLBs. At 100 mA

g^{-1}, the ASSLBs with Cu_2SnS_3/graphene/$Li_7P_3S_{11}$ nanocomposite cathodes show high reversible discharge specific capacity of 813.2 mA h g^{-1} and after 60 cycles, it retains 732.0 mA h g^{-1}. At 500 mA g^{-1} after 200 cycles, it retains 363.5 mA h g^{-1}.[133]

Third, aside from being an additive material to enhance the electronic conductivity and surface contact between the cathode and electrolyte, graphene can also be used as a promoter to inhibit material aggregation and improve material contact. For instance, Hongli Wan et al. applied graphene into Cu_2ZnSnS_4 (CZTS) to fabricate the composite anode with enhanced electrochemical performance and stability. To be specific, compared with pure CZTS, the addition of graphene can provide electronic conductivity pathways, mitigate anode active material degradation caused by the volume changes, inhibit the aggregation of active materials, and improve the contract between the electrolyte and active materials. As a result, good electrochemical performance has been achieved, the capacity of the CZTS/graphene is 760.4 mA h g^{-1}, which is higher than that of pure CZTS (632.3 mA h g^{-1}), and the ASSLB shows a discharge capacity of 645.4 mA h g^{-1} after 50 cycles and an energy density of 346.2 W h kg^{-1} (Figure. 5d).[134]

(2) GO

GO is the oxidized derivative of graphene. It has similar structure with graphene which can provide extra ionic channel. As a result, it has potential to be used in the ASSLBs. The major application of GO can be divided into two parts.

Due to its layered structure, the GO provides extra ionic transport channels. Cheng Zhang et al. designed a carbon matrix (GO-PEG) with lithium-ion conductor (PEG) as the cathode to load sulfur for all-solid-state lithium–sulfur batteries. The surface of the GO-PEG contains evenly distributed sulfide GO–PEG@C/S cathode through a one-pot

reaction. In addition, by the application of GO, it enables the uniform distribution of super P to improve the electronic conductivity. At 0.2 C and 80 ˚C, the ASSLBs with GO–PEG@C/S cathode shows an initial capacity of 1225 mA h g^{-1}. At 2C and 80 ˚C, this ASSLB retains 86.6% capacity after 100 cycles.[135]

On the other hand, GO has high ionic conductivity to be used at the surface interface, which will not influence the electrochemical performance of ASSLBs. GO can prevent the direct contact between cathode and electrolyte to suppress side reactions. For example, Zilong Zhuang et al. applied graphene oxide at the interface to suppress side reactions. They studied the reaction between the cathode-$LiNi_{0.5}Co_{0.2}Mn_{0.3}O_2$ and polymer electrolyte-PPE, where the oxidized products Ni^{3+} and Co^{4+} will cause the decomposition of PPE. In order to avoid the side reaction, graphene oxide was used to coat the $LiNi_{0.5}Co_{0.2}Mn_{0.3}O_2$ cathode, as a result, the ASSLB shows higher initial capacity, cycle life and interface contract. After 300 cycles, it retains 69.2% capacity at 0.3 C.[136]

(3) rGO

rGO has a structure that is highly similar to graphene, therefore it has similar properties to graphene, with high electronic conductivity, large surface area, excellent mechanical strength, and excellent flexibility. High surface area, excellent flexibility and great mechanical strength can buffer the volume changes in the cathode, which can significantly improve the interfacial contact and cycle life of the ASSLBs. As a result, The main effects of rGO in the cathode can be divided into two parts.[137]

Based on the similar structure with graphene, rGO can be used to modify the surface of cathode to improve the interfacial contact between the cathode and electrolyte. For instance, Xiayin Yao et al. coated 2nm of sulfur on the surface of rGO to reduce the

interface resistance, strain and stress between the sulfur cathode and SSEs in ASSLBs, where the sulfur is uniformly distributed on the surface of rGO (Figure. 5e). Compared with the Li-sulfur battery that utilizes liquid electrolyte, rGO@S-$Li_{10}GeP_2S_{12}$-acetylene black composite cathode shows similar electrochemical performance in ASSLBs. At 0.1, 0.5, 1.0, 2.0 and 5.0 C it respectively achieves 1384.5, 1336.3, 903.2, 502.6 and 204.7 mA h g^{-1} capacity. After 50 cycles at 1.0 C, a capacity of 830 mA h g^{-1} was retained. By the application of rGO, the volume change process during lithiation and delithiation becomes uniforms, which extends the cycle life of ASSLBs because of reduced stress and strain.[138]

In addition, the layered structure of rGO can provide extra electronic and ionic channels to enhance electronic performance. In preliminary work, Zhang Yue et al. simply combined rGO with V_2O_5 nanowires to fabricate an rGO composite paper cathode to increase the electronic conductivity of ASSLBs, where uniform distribution of the V_2O_5 nanowires was observed by SEM. PEO-MIL-53(Al)-LiTFSI lithium−vanadium batteries whose cathode is V_2O_5 nanowire−rGO composite paper were produced, which can work at high temperature and has high safety. Under the condition of 17 mA g^{-1}, the average capacity of the lithium battery can reach 329.2 mA h g^{-1}, and the capacity remains stable after 40 cycles. In addition, the lithium ion storge performance is fast and stable at 80 ºC with a voltage window of 1.0-4.0 V.[139] To further improve the combination of rGO and active materials, Qiang Zhang et al. designed a new 10% rGO-VS_4@$Li_7P_3S_{11}$ nanocomposite as the cathode of ASSLBs, where the VS_4 grows smoothly on the surface of rGO nanosheets. At 0.1 A g^{-1}, Li|75%Li_2S-24%P_2S_5-1%P_2O_5|$Li_{10}GeP_2S_{12}$/ 10%rGO-VS_4@$Li_7P_3S_{11}$ ASSLBs show a high reversible capacity of 611 mA h g^{-1} after 100 cycles.[140] In addition, in order to systematically evaluate the effect of rGO in cathode,

Qiang Zhang et al. also applied MoS_3 nanoparticles onto the surface of the rGO as the cathode by the replacement of VS_4. By the application of nanoparticle and 2DMs, the volume change becomes smaller, and electronic conductivity is improved due the addition of 2DMs. At 0.1 A g^{-1}, after 100 cycles, the Li|75%Li_2S–24%P_2S_5–1%P_2O_5|$Li_{10}GeP_2S_{12}$/rGO-MoS_3 ASSLBs show 553.4 mA h g^{-1} reversible capacity. The improvement is more significantly at high currents, at 1.0 A g^{-1}, after 500 cycles, it retains 414.1 mA h g^{-1} (Figure. 5f).[141]

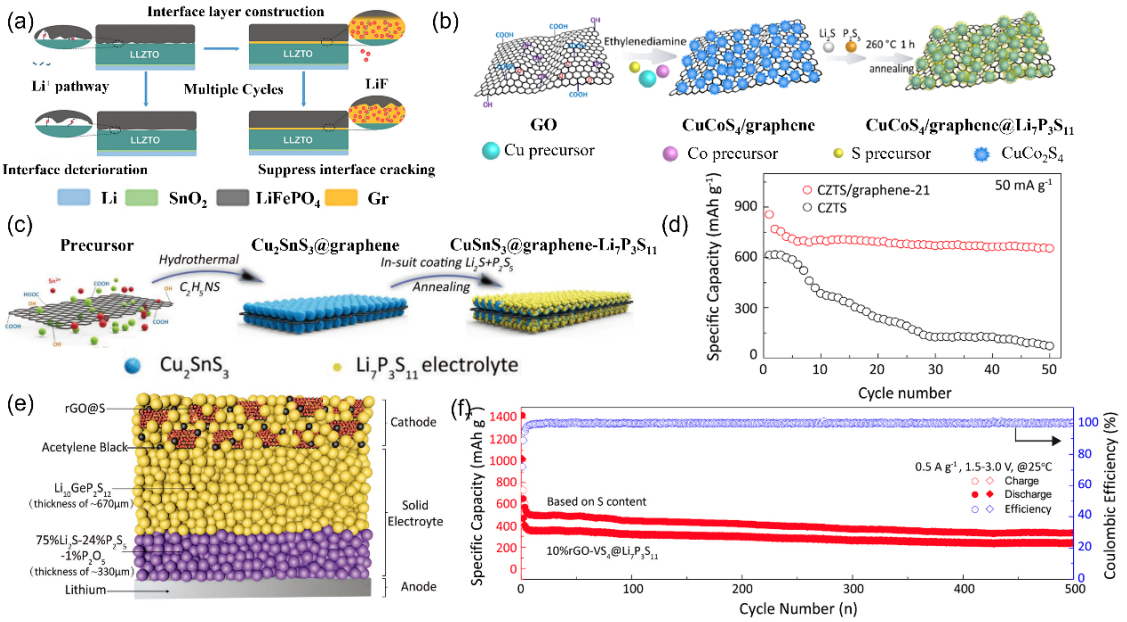

Figure 5. (a) LiF/graphene inorganic composite interlayer. Reproduced by permission.[131] Copyright 2020, Royal Society of Chemistry. (b) $CuCo_2S_4$/Graphene@$Li_7P_3S_{11}$ nanocomposite. Reproduced by permission.[132] Copyright 2020, American Chemical Society. (c) Cu_2SnS_3@graphene-$Li_7P_3S_{11}$ nanocomposite. Reproduced by permission.[133] Copyright 2019, Wiley-VCH. (d) cyclic performances for CZTS and CZTS/graphene-21. Reproduced by permission.[134] Copyright 2016, Elsevier. (e) rGO@S-$Li_{10}GeP_2S_{12}$-acetylene black (AB) composite cathode. Reproduced by permission.[138] Copyright 2017,

Wiley-VCH. f) 10%rGO-VS_4@$Li_7P_3S_{11}$ cathodes between 1.5 and 3.0 V at 0.5 A g^{-1}. Reproduced by permission.[141] Copyright 2019, Elsevier.

3.1.2.2 2D transition metal chalcogenides (TMC)

2D TMC is another potential material used in ASSLBs. Compared with traditional cathode materials, the application of transition metal sulfides will significantly decrease the interface resistance between cathode and electrolyte. Besides, TMCs can be used as active material to provide the high reversible capacity density and moderate operating voltage of ASSLBs. Moreover, based on its 2D structure, 2D TMCs can provide extra lithium-ion transport compared with bulk transition metal sulfide. The major feature of different TMCs can be divided into three kinds.

Initially, some kinds of 2D TMCs are used to provide high ionic conductivity and great interface compatibility, which is essential to deal with the low conductivity and high resistance problem. Santhosha, A. L. et al. compared bulk MoS_2 with 2D layered MoS_2 to show the superiority of 2DMs in ASSLBs (Figure. 6a). 2D MoS_2 is excellent and suitable for ASSLBs, which has 670 mA h g^{-1} theoretical capacity, 1.54 V theoretical redox potential, and 10^{-4} Ω cm^{-1} electronic conductivity. Moreover, 2D MoS_2 has small volume change compared with typical cathode materials, which is essential for ASSLBs to deal with the loss of contact resulting in high resistance.[142,143] In theory, based on the nanostructure of 2D layered MoS_2, MoS_2 will have high specific surface area, which can lower the contact resistance with the electrolyte . 2D layered MoS_2 also enables 2D diffusion because of its 2D structure for the intercalation process of Li. MoS_2 was used to prepare the composite cathode. The cathode uses 3 tons and contain 60 wt% MoS_2, 30

wt% β-Li_3PS_4 solid electrolyte, and 10 wt % carbon blacks by cold-pressing. The SE use β-Li_3PS_4 while the anode uses Li-In alloy. The initial specific capacity is 439 mA h g^{-1} in 67 mA g^{-1} in the 0.01-3.0 V range. After 500 cycles, it retains a battery capacity of 312 mA h g^{-1}. By substituting the 2D layer MoS_2 with bulk MoS_2, the initial discharge capacity is only 259 mA h g^{-1}.[143]

Other kinds of transition metal sulfide are desirable due to their affordable cost, environmentally benignity, and abundant resources. As the representative transition metal, Fe has been extensively explored. Qiang Zhang et al. designed an FeS based cathode which has high theoretical specific capacity of about 609 mA h g^{-1} and stable reversible capacity.[144] FeS nanoparticles were synthesized by a polyvinyl alcohol precipitation method. Based on SEM observations, the morphology comprised a flower-like structure which is about 300 nm and with some sheet-like subunits. This special structure provides some void space, which can buffer the electrode's volume change in the charge and discharge process that can cause losses of mechanical contract.[145,146] With the application of thin FeS nanosheets, the Li ion pathway will become shorter, and the Li ion insertion and extraction kinetics will be improved. By using nitrogen adsorption-desorption measurements, the specific surface area of FeS nanosheets is 60.31 m^2 g^{-1}. The large specific surface generates more reaction sites for the Li ion insertion and extraction process. The obtained all-solid-state lithium battery displays a reversible discharge capacity of 550 mA h g^{-1} after 50 cycles at 0.1 A g^{-1}. Even if the current density is increased to 1.0 A g^{-1}, the specific discharge capacity is 403 mA h g^{-1}. To improve the interface contact between the electrolyte and cathode, Fe_3S_4 was also explored. As Fe_3S_4 has a combination of +2 and +3 valence of Fe, it shows excellent electrochemical performance compared to FeS. Qiang Zhang applied Fe_3S_4 ultrathin nanosheets, which

also serves as the cathode active material, onto $Li_7P_3S_{11}$ for ASSLBs by an in-situ approach. The interface contact of Fe_3S_4@$Li_7P_3S_{11}$ nanocomposites is better than pristine Fe_3S_4 nanosheets, which shows 1001 mA h g^{-1}capacity after 200 cycles.[144] Besides Fe, V-based cathode materials such as V_2O_5 have also been applied . As a 2D sulfide, a high-crystallinity VS_2 sheet with a thickness of 50 nm has been used as a new 2DMs to improve the performance of ASSLBs' cathodes (Figure. 6b). VS_2 has a hexagonal transition metal hydrogen disulfide structure, so VS_2 has high electronic conductivity and high specific surface area. Liangting Cai et al. applied hc-VS_2 as cathode materials, which demonstrates great interface compatibility with P_2S_5 sulfide electrolyte. The experimental results show that under the condition of 50 mA g^{-1}, the high crystallinity VS_2 sheet has high reversibility, and the capacity after 30 cycles is 532.2 mA h g^{-1}.[147,148] After 100 cycles, at 100 and 500 mA g^{-1}, the stable discharge capacity of the all-solid-state lithium battery is maintained at 436.8 and 270.4 mA h g^{-1} respectively.[149]

Furthermore, compared with bulk TMCs, 2D TMCs have high mechanical strength, which not only can used as host material for active material-sulfur, but also can deliver high reversible specific capacity for ASSLBs. Shiqi Xu et al. designed a new type of intercalation-conversion hybrid cathode with VS_2 nanosheets which was used in ASSLBs (Figure. 6c). In this design cathode, on the one hand, VS_2 not only provides electron transport channel like most 2DMs, but also contributes the extra capacity. One the other hand, lithiated VS_2 (Li_xVS_2) can provide extra Li transport channels. The sulfur utilization of Li|Li_3PS_4|S/VS_2/Li_3PS_4 ASSLBs is 85% and the coulombic efficiency is close to 100%. Moreover, the active material loading and an areal capacity of this kind of ASSLB reaches the practical requirement of Li-S batteries, which is 15.5 mg cm^{-2} and 7.8 mA h cm^{-2}, relatively.[149]

3.1.2.3 Other types of 2DMs

Other materials include organic, metal oxide, and carbon materials. The major application of these materials can be divided into two parts. One of major application of these kinds of 2DMs is to enhance the ionic conductivity of active materials as the additives. Organic materials are one kind active material which has high theoretical capacity. However, one the main disadvantage of organic cathodes is the low ionic conductivity which limits the performance of the lithium battery. In order to deal with this problem, Yuta Fujii et al. applied 2D HHP ($(CH_3(CH_2)_2NH_3)_2$-$(CH_3NH_3)2Pb_3Br_{10}$) in ASSLBs with sulfide solid electrolyte. The recent report shows the mechanism of the insertion and extraction of lithium, which implies the potential of this material applied in the ASSLBs. 2D HHP inherently has Li-ion conductivity, which can reach to about 10^{-3} S cm^{-1}. At 100 °C, the resistance between the electrode and solid electrolyte is only 13 Ω. The ASSLB retains 242 mA h g^{-1} after 30 cycles at 0.13 mA cm^{-2}.[150] Jiamin Shi et al. applied 2D Co_3S_4 hexagonal nanosheets as cathodes to improve the interface contact and Li-ion conductivity of ASSLBs. 2D Co_3S_4 hexagonal nanosheets were used in a liquid-phase method to coat the surface of $Li_7P_3S_{11}$ (Figure. 6d). This structure provides shorter Li-ion transport channels and excellent machine contact due to the large surface area of 2DMs. At 0.5 A, after 50 cycles, the ASSLBs with Co_3S_4@$Li_7P_3S_{11}$ composite cathode exhibits 685.9 mA h g^{-1} reversible capacity. At 1 A, after 100 cycles, it retains 457.3 mA h g^{-1}.[151]

Metal oxides are the conventional cathode material for lithium-ion batteries. In order to improve the ionic conductivity and energy density, Qiuying Xia et al. designed

Li_xMnO_2 nanosheets to fabricate a 3D-structured cathode for ASSLBs. This cathode design showed a high electrochemical tunnel intergrowth structure, which provides alternating 1 × 3 and 1 × 2 tunnels. In addition, this 3D structure provides shorter Li-ion transport length, better interface contract, and great mechanical strength. At 50 mA g^{-1}, the Li_xMnO_2/LiPON/Li ASSLB yields 185 mA h g^{-1} and retains 81.3% after 1000 cycles.[152]

Carbon nanosheets are used as the electronic conductive material to improve the interface contact in ASSLBs. V_2O_5 is one of the new lithium-free cathode materials. However, its high-volume change and poor contact with the electrolyte are challenges for implementation in ASSLBs. The nanomodification of V_2O_5 is insufficient to solve these problems. Thus, Liwei Su et al. coupled carbon nanosheets with the V_2O_5 cathode. Sub-10 nm V_2O_5/C nanosheets were used as the cathode, which shows excellent contact between the electrode and electrolyte and great interface stability. In addition, by the application of carbon nanostructure, the volume change of V_2O_5 is suppressed, which avoids cracking and pulverization of the surface and improves the electronic conductivity. The ASSLBs with V_2O_5/carbon nanosheet cathode is 228 mA h g^{-1} at 0.1 C and ~110 mA h g^{-1} at 2.0 C after 50 cycles.[153,154]

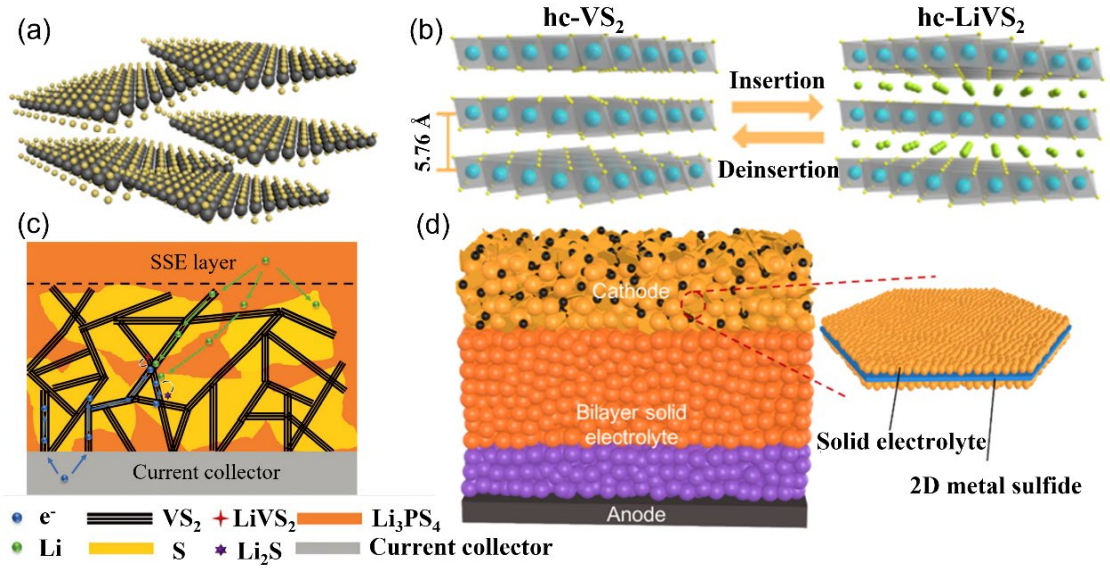

Figure 6. (a) exfoliated MoS_2 nanosheets. Reproduced by permission.[143] Copyright 2019, American Chemical Society. (b) highly crystalline layered VS_2 (hc-VS_2) nanosheets. Reproduced by permission.[147] Copyright 2018, American Chemical Society. (c) proposed microstructure and discharge mechanism for the solid-state hybrid Li-S/VS_2 battery. Reproduced by permission.[149] Copyright 2020, Wiley-VCH. (d) monodispersed 2D Co_3S_4 hexagonal platelets. Reproduced by permission.[151] Copyright 2020, American Chemical Society.

3.2 2DMs in electrolyte design of ASSLBs

The electrolyte in ASSLBs mainly includes three types of materials: polymers, oxides and sulfides. Due to different physical, chemical and electrochemical properties, these three kinds of SEs encounter different problems in ASSLBs. High-performance SEs require certain properties, such as high ionic conductivity in room temperature, high thermal stability, great chemical stability, good contract with electron in both physics and

chemistry. In this section we discuss how to use different 2DMs to solve the problems encountered by different solid electrolytes.[155]

3.2.1 Solid polymer electrolytes (SPE)

SPEs used in the ASSLBs such as polyethylene oxide (PEO), poly(acrylonitrile) (PAN), poly (vinylidene fluoride) (PVDF), have similar problems in ionic conductivity, low mechanical strength, and limited lithium ionic transport channels. Segmental motion is the main mechanism for the Li ions transport in the polymer-based electrolyte. Compared with the ion conduction in the liquid, this conduction mechanism is more dependent on temperature to reduce the grain boundary resistance of the polymer electrolyte. Therefore, at room temperature, the ionic conductivity of the polymer solid electrolyte is extremely low. In conclusion, high ionic conductivity, high chemical and thermal stability and great interface contract should be achieved in SPEs. This part will introduce the application of 2DMs to deal with these limitations.[130]

3.2.1.1 PEO based solid polymer electrolytes

PEO is a widely used polymer electrolyte which has high performance. Li ions can move in PEO through chain segmental motions.[127] Based on the mechanism of lithium-ion transport in PEO, the conductivity of Li ion is influenced by the motion of the amorphous phase of PEO. Due to the highly crystalline structure of PEO, the Li-ion conductivity of PEO is only 10^{-6}–10^{-8} S cm^{-1} at room temperature. At higher temperatures, PEO's Li-ion conductivity will be significantly enhanced, although high temperature will reduce the mechanical strength and chemical stability. In order to deal

these problems, 2DMs are used to improve the electrochemical performance by its unique structure. The effect of 2DMs in PEO can be divided into three parts.

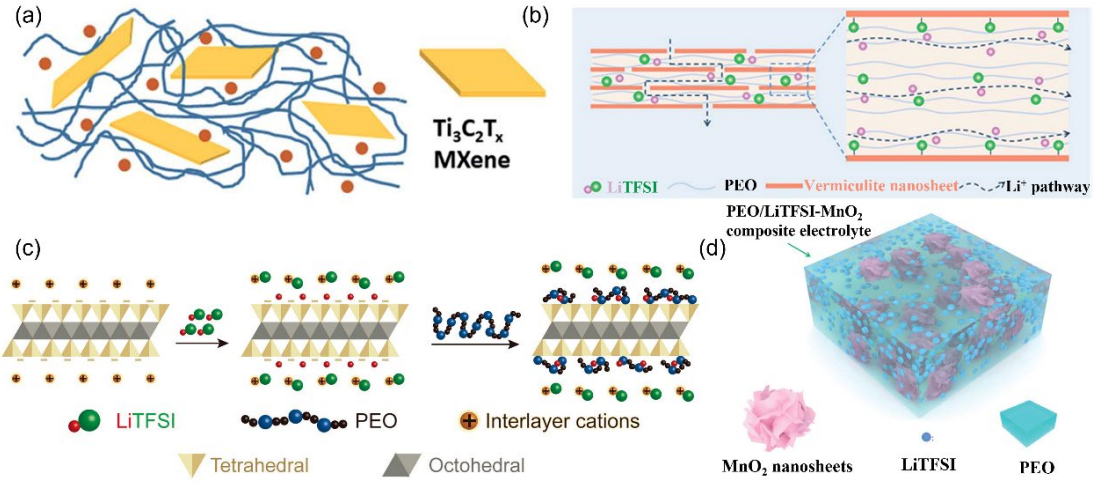

Figure 7. (a) MXene/PEO composition polymer electrolytes (CPEs). Reproduced by permission.[156] Copyright 2020, American Chemical Society. (b) the lithium ions transfer mechanism in Vr/PEO-LCSE. Reproduced by permission.[157] Copyright 2020, Royal Society of Chemistry. (c) mechanism for VS enhanced ionic conductivity in SPE. Reproduced by permission.[158] Copyright 2019, American Chemical Society. (d) composition of a PEO/LiTFSI/MnO_2 solid polymer electrolyte membrane. Reproduced by permission.[159] Copyright 2020, Royal Society of Chemistry.

First, 2DMs can reduce the crystallinity of PEO to enhance the ionic conductivity of PEO. There are two ways to incorporate 2DMs in PEO. One is due to the hydrophilic surface in materials to interact with oxygen through hydrogen bonds with PEO. In the first way, three main kinds of materials are listed here. The first material is MXene, where Qiwei Pan et al. added hydrophilic $Ti_3C_2T_x$ into PEO_{20}-LiTFSI to reduce the crystallinity of PEO and enhance the ionic conductivity (Figure. 7a). The PEO with 3.6 wt% MXene

shows great ionic conductivity which is 2.2×10^{-5} S m^{-1} at 28 °C. The $LiFePO_4/PEO_{20}$-LiTFSI/Li with 1.5 wt% MXene has been tested in here, it shows stable capacity (140 mA h g^{-1}) at 60°C after 50 cycles.[156] The second way is using carbon materials. Masoud Esfandeh et al. produced SSEs based on polyethylene oxide (PEO) which contains pristine graphene (GnP) or polyethylene glycol grafted graphene (FGnP)[160] The synthesized SSE was characterized using SEM, DSC, XRD and polarization state optical microscope (POM), which verifies that the crystallinity of the nanocomposite electrolyte was reduced.[161] The specific anti-nucleation effects of GnP and FGnP can be obtained through the image of POM. The specific properties of FGnP can be attributed to the fact that PEO molecules grafted on FGnP can interact with oxygen through hydrogen bonds and limit crystallization.[160] As a result, at room temperature, the ionic conductivity of SPE/FGnP (0.5%) is significantly improved (2.53×10^{-5} S cm^{-1}), and the mechanical stability is also improved.[160] The third material is MOF. Qingyue Han et al. incorporated nickel-based ultrathin metal−organic framework (MOF) nanosheets (NMS) into PEO. Due to the high aspect ratio of NMS, the application of NMS significantly reduces the crystallinity of the PEO, which enhances the ionic conductivity. Moreover, the dissociation of lithium salt can be enhanced by the Lewis acid-base interactions between Ni atoms in NMS and anions in the lithium salt, which can increase the concentration of Li-ion in PEO. The Li-ion transference value reaches to 0.378 and the ionic conductivity reaches 1.66×10^{-5} S cm^{-1} at 25 °C. Similar with other 2DMs, NMS can enhance the mechanical strength of the PEO. At 0.1 C at 30 °C after 50 cycles, the all-solid-state $Li/LiFePO_4$ battery with NMS/PEO shows a high reversible capacity of 130 mA h g^{-1}.[156]

Second, with the application of 2DMs, the mechanical strength of PEO can be enhanced significantly. 2D BN can be also used in polymer solid electrolyte due to its

excellent electrochemical properties. Based on the conventional properties of 2D BN, Zhenyu Zhang et al. designed a new ASSLB based on boron nitride enhanced polymer/salt (PVDF-HFP/LiTFSI) composite electrolytes. By the application of the 2D BN, the mechanical strength, ionic conductivity, and interface contact of the composite electrolyte was enhanced. The ionic conductivity of 1% BN composite electrolyte is 1.82 $\times 10^{-3}$ S/cm at room temperature. In order to test the mechanical strength of composite electrolyte, the hardness and Young's modulus were tested, which is 4.99 MPa and 0.133 GPa, relatively, which can significantly suppress the growth of lithium dendrites. [162] Furthermore, Xuedong Yin et al. proposed the importance of thermal uniformity for SSEs. After the addition of 2D BN, BN-PEO-PVDF's ionic conductivity and mechanical strength were improved significantly. Specially, 2D BN enables fast conduction and uniform distribution of heat in PEO. As a result, homogenous ionic conductivity is achieved in PEO, because the ionic conductivity of PEO depends on temperature. Finally, The deposition and extraction of lithium become more uniform, and thus the ASSLBs show long cycle life and high performance.[163] In order to significantly improve the mechanical properties of PEO, Pengfei Zhai et al. applied vermiculite nanosheets into PEO to fabricate Vr/PEO-LCSE. At 25 °C, the Vr/PEO-LCSE shows a high ionic conductivity of 1.22 $\times 10^{-5}$ S cm^{-1} (Figure. 7b). The specific resistance of Vr/PEO-LCSE is much lower than pure PEO which is 66 Ω cm^{-2} at 30 °C. In addition, the excellent compressive strength of Vr/PEO-LCSE is 131 MPa which is much higher than pure PEO and compared with other 2DM additives. As result, the high-rate performance of ASSLBs is improved, which has low capacity fading from 0.05C to 0.2C.[157]

Third, 2DMs such as 2D VS, lepidolite can provide extra ionic transport channels to enhance the ionic conductivity. Due to the high specific properties, most 2DMs can make

fast lithium-ion transport on the surface. To be specific, the properties of VS are similar with inactive ceramic fillers, VS has high chemical, thermal, machinal stability. Furthermore, the negative charge surface of the VS can be used to transport Li-ions. In order to study the effect of two-dimensional material arrangement on lithium-ion transmission, Wenjing Tang et al. first fabricated a PEO/LiTFSI/10% 2D VS layered composition electrolyte to improve the electrochemical performance of ASSLBs with disorderly arrangement (Figure. 7c). The Negatively charged surface of 2D VS layers provide more channels for lithium-ion transport. Thus, the lithium-ion conductivity is much higher than normal PEO. At 25, 60, and 100 °C, the ionic conductivity is 2.9×10^{-5}, 1.2×10^{-3} and 3.1×10^{-3} S cm^{-1}, respectively. In addition, at current density of 50 μA cm^{-2}, the Li/VS composition PEO/Li symmetrical cells work with stable voltage profiles over two months. The Li/$LiFePO_4$ cell is tested in this time, at 0.1 and 0.5 C, the capacity of this battery is 159.9 and 152.0 mA h g^{-1}, respectively.[164] In addition, Wenjing Tang designed another ASSLB using 2D VS layers. In this time, 2D VS is arranged in PEO in a vertical direction, which can generate continuous channels and larger surface area. As a result, Li^+ transference number close to 0.5 reaches an ionic conductivity as high as 1.89×10^{-4} S cm^{-1} at 25 °C.[165,166] A lithium symmetric battery using vertically aligned VS-based PEO composite electrolyte was tested over 1300 hours, which is stable with low overpotential. [167] The full battery test was also tested here to verify the performance of this electrolyte, at 0.1 C, 35 °C, the ASSLBs based $LiFePO_4$ showed a capacity of 167 mA h g^{-1} with the application VAVS–CSPE and retains 82% capacity after 200 cycles at 0.5 C.[165,168] PEO has shown improved thermal stability, high mechanical strength, ionic conductivity and electrochemical stability after the addition of 2D VS layers, and decreased flammability and interface resistance.[158]

Covalent nitrides with high thermal and chemical stability are always applied to stabilize the interface between the PEO-based electrolyte and lithium metal anode. By the application of nitrides in PEO, the highly electronegative N atoms will interact with $TFSI^-$ to enhance the and selectivity of ion transport and dissociation of LiTFSI in PEO. First example is for selectivity of ion transport. Yuhan Li et al. applied 2D hexagonal boron nitride (h-BN) in PEO. The stronger binding effect between $TFSI^-$ and BN than between Li-ion and BN is simulated by the DFT calculation, which indicates that the Li-ion conductivity of PEO/LiTFSI/BN is lower than without BN. However, the transport of $TFSI^-$ is reduced significantly. As a result, with the application of h-BN, the selectivity of Li-ion transport is higher. The Li/Li symmetric battery with PEO/LiTFSI/h-BN lasts 430 h at 0.2 mA cm^{-2}. For the full battery with Li metal anode and $LiFeO_4$ cathode, the PEO/LiTFSI/h-BN composite electrolyte shows great cycle life for 140 cycles, compared to 39 cycles for SSEs without the addition of h-BN. [169] Second example is for enhancing the dissociation of LiTFSI. g-C_3N_4 nanosheets have some defects on the surface which is different with other defects in the other 2DMs, as it can provide extra lithium transport channels. In order to improve the performance of PEO, Zongjie Sun et al. added g-C_3N_4 nanosheets into the PEO to improve the ionic conductivity, working temperature and mechanical strength. The ionic conductivity reaches 1.7×10^{-5} S cm^{-1} at 30 °C. Moreover, lithium salt can interact with the N atoms on the surface of g-C_3N_4 nanosheets to improve the dissociation of the lithium salt. After 100 cycles, at 60 °C, the ASSLBs with PEO/g-C_3N_4 nanosheets show 155 mA h g^{-1}.[170]

Naturally derived 2DMs have also been explored as a PEO additive. Chengliang Wang et al. reported one kind of 2D natural layered silicate material, lepidolite. They designed a composite electrolyte with lepidolite, PEO and $LiClO_4$. The pure lepidolite is tested first,

it has an ionic conductivity at 100 °C of 1.5×10^{-5} S cm^{-1}. The composition with PEO and lepidolite without Li salt was tested next, it shows an increased Li-ion transference number with larger content of lepidolite in the composites. In order to increase the interface contact and ionic conductivity, PEO and $LiClO_4$ were added into the lepidolite to form the composite electrolytes, and the ionic conductivity at 60 °C can be increased to 1.6×10^{-4} S cm^{-1}. The obtained CPEs show improved ionic conductivity, greater Li^+ transfer, higher thermal stability and better mechanical characteristics than traditional polymer electrolytes.[158] Compared to other 2DMs, the combination between PEO and MnO_2 can provide long-range migration for lithium ions. Yuhan Li et al. applied MnO_2 into PEO to produce PEO/MnO_2 electrolyte, which exhibits better ionic conductivity, lithium transference number and mechanical strength (Figure. 7d). By density functional theory calculations, the PEO/Li complex and MnO_2 binding energy is small, which is beneficial for lithium ion to transfer in the interface between PEO and MnO_2. After 300 cycles, the ASSLB with PEO/MnO_2 electrolyte exhibits 143.5 mA h g^{-1}.[159]

Finally, the application of 2DMs is used to improve the thermal uniformity of PEO-based polymer electrolytes to stabilize the ASSLBs at high temperature. Xuesong Yin et al. applied 2D BN nanoflakes to deal with high operating temperature, poor thermal conductors, and lithium deposition problems in ASSLBs. After the addition of 2D BN, BN-PEO-PVDF's ionic conductivity, mechanical strength, and heat transport ability was improved significantly. Specially, 2D BN enables fast conduction and uniform distribution of heat in PEO. Finally, The deposition and extraction of lithium become more uniform, and thus the ASSLBs shows long cycle life, and high electrochemical performance.[163]

Table 1. The contribution of 2DMs to ionic conductivity of PEO based electrolyte.

Materials*	Ionic conductivity (S/cm)	Temperature (°C)
Polyethylene oxide	10^{-6}-10^{-8}	25
MXene	2.2×10^{-5}	28
polyethylene glycol-grafted graphene	2.53×10^{-5}	30
Vermiculite sheets	2.9×10^{-5}	25
	1.2×10^{-5}	60
	3.1×10^{-5}	100
Vertically aligned vermiculite sheets	1.89×10^{-4}	25
Lepidolite	1.6×10^{-4}	60
Nickel-based ultrathin MOF nanosheets	1.66×10^{-5}	25
Boron nitride	1.82×10^{-3}	25
g-C_3N_4 nanosheets	1.7×10^{-5}	30
Vermiculite nanosheets	1.22×10^{-5}	25

3.2.2 Other solid polymer electrolytes

Besides PEO, other polymers such as PAN, PVDF etc. have also been used as the solid electrolyte. 2D single-layer GO is one of the potential materials for application in ASSLBs. It has a large specific surface area and many oxygen-containing functional groups. It has been reported that the application of GO can enhance the transport of Li-ions and the chemical stability of the electrolyte, which is due to the oxygen-containing functional groups and the 2D structure of GO. Weishang Jia et al. reported a new design of $LiClO_4$-polyacrylonitrile (PAN) SPEs with the application of GO. This GO is modified by -OH, -COOH, -COC and other oxygen-containing functional groups. At 30 °C, the

ionic conductivity of composite PAN electrolyte with 1 wt% GO reached 4.0×10^{-4} S cm^{-1}, which is higher than pure PAN (2.2×10^{-5} S cm^{-1}). In addition, the application of GO reduces the activation energy from 2.31 to 1.03 eV and increase the tensile modulus from 37 to 80 MPa. Moreover, GO makes the polymer less crystalline to have better contact with the electrode. In terms of electrochemical performance, the $LiFePO_4$ (LFP) battery with 1.0 wt% GO-SPE as the electrolyte has an average discharge capacity of 166 mA h g^{-1} when maintained at 0.2C for 50 cycles, and the electrochemical polarization is relatively small at 38 mV.[171]

3.2.3 Sulfide electrolytes

Compared with SPEs, solid sulfide electrolytes (SSEs) can potentially combine the advantages of polymer electrolytes and oxygen-containing electrolytes. They have medium mechanical strength, which is favorable for both the interface contact and structural stability. However, SSEs are not chemically stable, as side reactions low coulombic efficiency. In this section, some improvement strategies will be introduced by the application of 2DMs. It can be divided into two parts.

One is mitigating the side reactions. Xiaoyan Xu et al. designed a strong $Li_7P_3S_{11}$ electrolyte with BN doping for an all-solid-state lithium sulfur battery (Figure. 8a). The BN nanosheets is able to partially separate the $Li_7P_3S_{11}$ solid electrolyte and lithium metal, thereby enhancing the electrode and electrolyte interfacial performance and prevent $Li_7P_3S_{11}$ from reacting with Li metal. By the application of boron nitride doped $Li_7P_3S_{11}$ solid electrolyte, this ASSLB shows improved electrochemical performance with better cycling stability and higher coulombic efficiency.[172,173]

Another one is providing extra lithium-ion transport channels. TiS_2 is one kind of TMDs. To deal with the poor ionic contacts between the active material and sulfide solid electrolyte, Dae Yang Oh et al. applied TiS_2 nanosheets which is prepared by the scalable mechanochemical lithiation to prepare TiS_2, followed by exfoliation by ultrasonication to prepare the nanosheets (Figure. 8b). With the addition of TiS_2, ASSLBs shows excellent reversible capacity due to the favorable contact with TiS_2 nanosheets and short lithium-ion transport channel. Compared with bulk TiS_2, TiS_2 nanosheets show shorter Li-ion transport channels and high electronic conductivity.[174]

3.2.4 Other type of solid-state electrolytes

Besides the solid polymer electrolyte, sulfide solid electrolyte, and solid oxide electrolyte, there are also many novel materials used as solid electrolytes. In this section, the application of 2DMs can be divided into two parts.

As usual, 2DMs provide extra lithium ionic transport channel to enhance the ionic conductivity of the electrolyte. Due to its porous structure and functionalization, perovskite and COF can be used as the electrolyte to promote the lithium-ion transport. Jiafeng Wu et al. use two kinds of perovskites: 3D-PVSK (CH_3NH_3PbI) and 2D-PVSK ($BA_2MA_3Pb_4I_{13}$) to modify the surface of the $Li_{6.75}La_3Zr_{1.75}Ta_{0.25}O_{12}$ (LLZTO) (Figure. 8c). With the modification of 3D-PVSK and 2D-PVSK, 2D PVSK provides extra transport channels for Li-ions compared with other modification methods. ASSLBs use lithium as the anode and $LiFeO_4$ as the cathode to test the application of 2D PVSK. The results show that ASSLBs have higher specific capacities of 153 mA h g^{-1} and 149 mA h g^{-1} with 3D-PVSK and 2D-PVSK respectively compared with no-PVSK ASSLBs, after

50 cycles at 0.2 C. To sum up, with the modification of 3D-PVSK and 2D-PVSK, it will provide more lithium storage of ASSLBs.[175] Zhen Li et al. designed a new COF with TFSI functional group (dCOF-ImTFSI-60). By the post-functionalization of $TFSI^-$, the ionic conductivity of dCOF-ImTFSI-60 is 7.05×10^{-3} S cm^{-1} at 423 K with the extra 1D pores for lithium ionic transport by the extra $TFSI^-$. Li/dCOF-ImTFSI-60@Li/$LiFePO_4$ ASSLB shows an initial capacity is 143.7 mA h g^{-1} under 353 K and retains 98.3% capacity after 40 cycles with 97.5% coulombic efficiency.[176]

In addition, dCOF will have a wide range working temperature range from 303 to 423K. [176] In the other work, Zhen Li et al. designed another type of 2D COF (Im-COF-Br) which was synthesized by Schiff base reaction, and the building block is imidazolium-based monomers. This new COF has some characteristics, such as positive charge in the COF skeletons, tunable counter-anions, and 5.57 nm pore sizes. In order to increase the transport of Li-ion, the Br^- is replaced with TFSI. The Im-COF-TFSI was tested at 353 and 423 K, which shows ionic conductivities of 4.64×10^{-4} and 4.04×10^{-3} S cm^{-1}, respectively.[177] Gen Zheng et al. designed a new combination between COF and PEO to fabricate a new type of electrolyte, which flexible and ethylene oxide PEO in the rigid two-dimensional COF architectures is used as lithium ionic transport channel to enhance the Li-ion conductivity. It is verified by powder X-ray diffraction and thermogravimetric analysis that the periodic structure is stable even over 300 °C, and the dynamic glassy structure of PEO is verified by differential scanning calorimetry and NMR. The Li-ion conductivity reaches 1.33×10^{-3} S cm^{-1} at 200 °C with LiTFSI doping.[178]

On the other hand, 2DMs are also applied as the electrolyte to transport lithium ions individually. Xing Li et al. applied 2D lithiated hydrazone-based COF with phenol group (2D LiCON) nanosheets into ASSLBs (Figure. 8d). First, at 40 °C, the ionic conductivity

of COF without Li salt reaches 10^{-5} S cm^{-1}. Second, it prevents the dissolution of organic redox species in the cathode. When the 2D LiCON is applied in the ASSLB, it is stable for 500 cycles at 500 mA g^{-1} at 20 °C.[179] In addition, with the unique properties of 2D COF, Wenlu Sun et al. fabricated ultra-thin SSEs with a thickness of 7.1 μm, which contributes to the high energy density of the battery.[180]

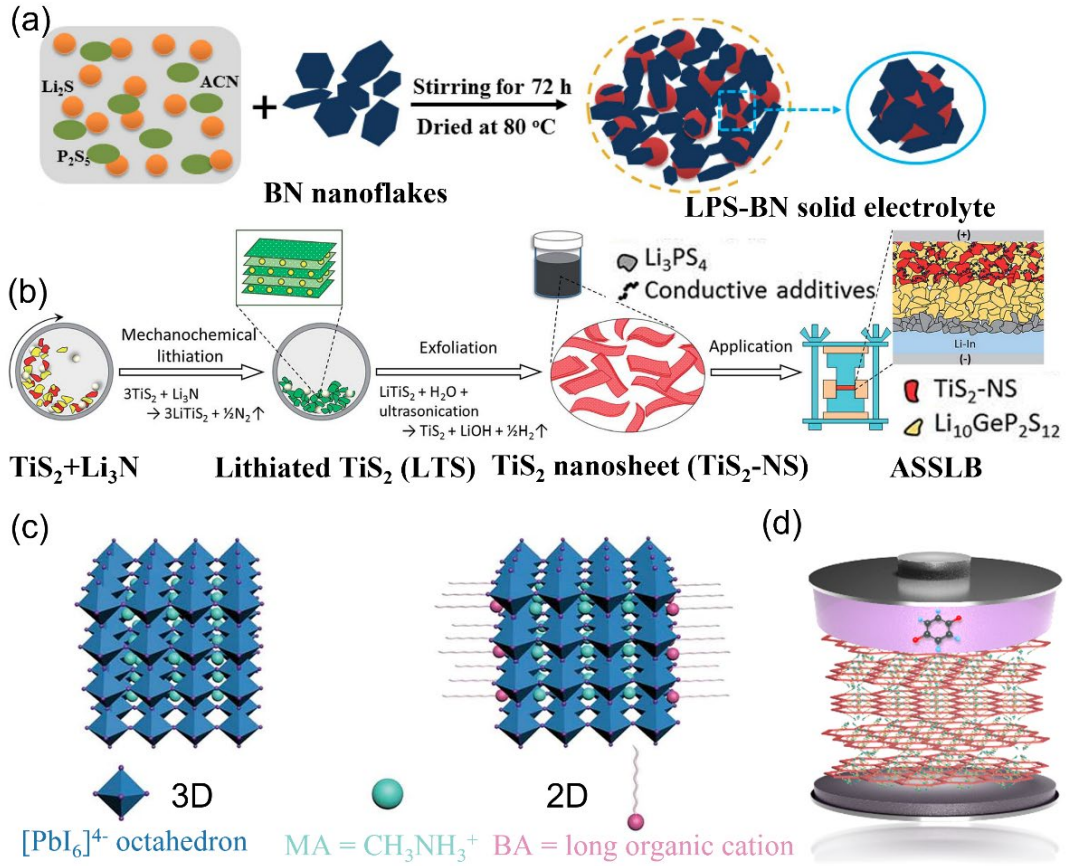

Figure 8. (a) fabrication process of LPS-BN solid electrolyte. Reproduced by permission.[172] Copyright 2019, Springer Nature. (b) preparation of TiS_2 nanosheets (TiS_2-NSs) and their application in bulk-type ASSLBs using sulphide SEs. Reproduced by permission.[174] Copyright 2016, Royal Society of Chemistry. (c) crystal structure of the 3D-PVSK and 2D-PVSK. Reproduced by permission.[176] Copyright 2020, Wiley-VCH. (d) 2D COF solid state electrolyte. Reproduced by permission.[179] Copyright 2020,

American Chemical Society.

Chapter 4

4. Emerging advanced characterizations for 2DMs used in ASSLBs

Considering the specific two-dimensional structure and physicochemical properties of 2DMs, only a few emerging advanced characterization technologies will be focused on this section to deeper the understanding of the structure-function relationship in 2DMs for ASSLBs. The advanced characterizations including synchrotron X-ray techniques and in-situ/operando characterization are summarized below.

Synchrotron radiation is one of most powerful technologies to study the structure and mechanism of battery materials. Compared with traditional characterization technologies, with the assistant of the high flux and brilliant X-ray beam, there are some advantages. First, it can get high structural resolution and 2D/3D morphology of 2DMs in ASSLBs due to the low presence of 2DMs in ASSLBs. Second, it has high temporal resolution, it can significantly shorten the time required for signal acquisition to get the dynamic information of 2DMs with combination with in-situ/operando technology. Third, direct visualization and 3D reconstruction of 2DMs can be acquired at the same time. In conclusion, in order to gain an in-depth understanding of the effect of 2DMs in the electrolyte, electrode and interface of ASSLBs, the synchrotron X-ray technique plays a critical role, which can be divided into four parts: X-ray diffraction (XRD), X-ray absorption fine structure (XAFS), X-ray photoelectron, and X-ray microscopy. In order to investigate the state of ASSLBs in the dimensions of time and space during operation, in-situ/operando technologies are applied as one of the most necessary technology to monitor energy-storge mechanisms with ASSLBs.[181,182]

In-situ characterization is applied to obtain the structure and composition information

of the sample most truthfully. With the application of the in-situ characterizations, the influence on the sample during the sample preparation process is avoided. After by optimizing the in-situ cell, operando technology is applied to achieve real-time observation of changes in ASSLBs. As a results, in-situ/operando technology is one of the most important characterization technologies for study of 2DMs in the ASSLBs.

In this section, spectroscopy material composition analysis and morphology and structure characterization will be introduced.

4.1 Spectroscopy material composition analysis

With the assistant of X-ray technology, in the structural investigations of SSEs, synchrotron XRD is one of the most attractive methods to obtain the structure and chemical information of SSEs. In contrast to laboratory X-ray sources, the measurement of scattering from dilute phases or the analysis of residual stress can be obtained by the assistance of the high resolution and intensity of the synchrotron.[183,184] In addition, synchrotron radiation has the unique advantages of enhancing the signal strength and reducing test time, which enables the development of time-resolved XRD and in-situ/operando XRD in synchrotron beamlines. Thus the crystallographic information of 2DMs, including lattice parameters of different phases, site occupancy, strain/stress, and microstructural information, can be further detected by the diffraction techniques.[185–187]

As mentioned above, the interface stability of interface between the electrolyte and electrode is one of the essential problems that should be resolved, especially for high-voltage cathode materials such as $LiCoO_2$. To detect the side reactions during operation, in-situ XRD is applied in here. For instance, Vardar et al. applied $LiCoO_2$ electrode and

LLZO electrolyte as a model system. The side reaction products are easily detected by the application of synchrotron source, new peaks were detected which is attributed to the composition of Li_2CO_3, $La_2Zr_2O_7$, and $LaCoO_3$ (Figure. 9a). The side production layer will suppress the lithium-ion transport in the interface.[188] With the assistance of 2DMs at the cathode electrolyte, the side reactions between electrolyte and high-voltage cathode has been significantly suppressed. Through synchrotron radiation in-situ XRD monitoring, any side-products produced by the electrode and electrolyte in the operation process can be immediately observed to analyze the failure mechanism of ASSLBs.

XAFS is one of the most powerful technical tools for analyzing 2DMs. It describes X-ray absorption near or above the absorption edge. Due to the different energy ranges, XAFS can be divided into two parts. X-ray near-edge absorption structure (XANES) refers to the spectral region from the absorption edge to the energy range of 30-50 eV beyond the absorption edge. Extended X-ray absorption fine structure (EXAFS) is a type of extended X-ray absorption fine structure. XANES can distinguish between electronic states and three-dimensional coordination geometry. Differently, EXAFS is sensitive to the distance, coordination number, and type of atoms around the adsorbed atoms.[189]

To distinguish the difference of the local atomic geometry and the chemical state of the atoms for 2DMs with their 3D bulk counterparts, XAFS is applied to analyze the specific element. For example, for the atom of a specific element, the coordination number is significantly reduced, and bond lengths are elongated in 2DMs compared with the bulk materials.[190] For the ASSLBs, the presence of 2DMs in electrode and electrolyte are minimal. To detect the 2DMs, with the application of synchrotron radiation, the X-ray absorption energy near or above the absorption edge can be detected. In addition, compared with the EXAFS, the signal of XANES is clearer, the time required to collect

the signal is shorter, and it is more sensitive to the element valence and charge transfer.

Therefore, the in-situ XANES based on the synchronous light source has a time resolution that can be used to study the electronic states and three-dimensional coordination geometry of specific elements for 2DMs in ASSLBs. [191] To analyze the failure mechanism of the SSEs, Weihan Li et al. applied in-situ XANES to observe the nanoscale molecular level and local chemical environment in real time during the operation state of SSE-Li_3InCl_6 (Figure. 9b). As a result, the degradation reaction can be observed between H_2O and Li_3InCl_6, which will produce In_2O_3 and LiCl to reduce the ionic conductivity of SSE.[192]

In summary, by the application of in-situ characteristics technology and synchrotron radiation technology of XAFS, changes in the coordination environment of any element can be observed under operating conditions of ASSLBs, which is of great significance for the more detailed interpretation of the application of characteristic elements in 2DMs in ASSLBs.[193]

Lithium metal is prone to irreversible side reactions with solid electrolytes due to its high reactivity, leading to battery failure. Therefore, it is of great significance to construct an interface layer with high ionic conductivity. In-situ XPS is one technique to delineate the composition change of the SEI during the charge and discharge process. Jürgen Janek et al. used in-situ XPS to characterize the electrochemical deposition process of lithium metal on the surface of a typical sulfide solid electrolyte $Li_{10}GeP_2S_{12}$ (LGPS) to study the interface stability of the LGPS and lithium metal. According to the known position and intensity of the peaks of the relevant components, by fitting the in-situ XPS peaks, it is possible to compare and observe the changes of each component during the charging and discharging process.[194] Wenjia Yan et al. applied the BN nanosheet as SEI to suppress the

side-reaction between electrolyte and lithium metal. In-situ XPS can be used in here to detect the SEI composition in the operation process, the content change of Li_3N during lithium deposition can be detected.[126]

4.2 Morphology and structure characterization

The mechanism of in-situ TEM is that the electron beam with a very short wavelength penetrates the sample and uses an electromagnetic mirror to control the focus of the electron beam to measure it. In-situ TEM improves the time-based resolution to detect the microscopic morphology, crystal structure and phase, which is one of the powerful analytical methods for systematically studying the electrochemical reaction mechanism and failure mechanism of the solid-state battery charge and discharge process. Nomura et al. used the EELS of the TEM to use sparse coding and structure technology to dynamic change of the lithium ions concentration distribution in SSE. Dynamic observation found that during the electrochemical reaction, lithium ions not only move in the vertical direction to the SEI, but also move in parallel directions, resulting in spatial changes in the concentration of lithium ions on the nanometer scale. With the addition of 2DMs in the SSE, the lithium ions concentration distribution in the interface between SSE and 2DMs will represent the unique lithium ions transport way by the observation of in-situ TEM.[195]

In-situ SEM technology is based on the secondary electrons and scattered electrons when electron beam scans the surface of the sample to obtain the real-time imaging. In addition, with the assistant of EDS, the element changes during the charge and discharge process. In ASSLBs, the growth of lithium dendrites in the lithium metal anode is one of

the most serious problems. The application of 2DMs such as MXene, BN, VS, etc. in the interface between the anode and electrolyte is used to suppress the growth of lithium dendrites, as it changes the mechanism of the growth of lithium metal. [196] As a result, the application of in-situ SEM is important to observe the whole process of growth of lithium dendrites. Sagane et al. applied LiPON ($Li_{3.3}PO_{3.8}N_{0.22}$) as the SSE and performed in-situ SEM to observe the process of extraction and deposition of lithium metal on the surface of the negative electrode (Figure. 9c). With the application of 2DMs such as MXene, BN, VS, in the interface between anode and electrolyte to suppress the growth of lithium dendrites, the mechanism of the growth of lithium metal is different.[197]

In-situ X-ray tomography can track the dynamic changes of the morphology, crystal structure and chemical components of the components in the battery in real time during battery operation, which is of great significance for the study of solid-state battery interface properties, interface changes and battery failure mechanism. Gewirth et al. constructed Li|LGPS|Li symmetrical battery and used in-situ X-ray tomography to monitor the real-time three-dimensional morphology of the LGPS solid electrolyte, especially the interface between the LGPS and lithium metal during the battery cycle (Figure. 9d). Compared with polymer-based solid electrolyte, in-situ X-ray tomography is more important for oxygen-based and sulfur-based electrolytes, the arrangement mode of the particles will have a huge impact on the conduction of lithium ions.[198]

Aside from summarized technologies, some other advanced characterizations are also applied in the 2DMs used in ASSLBs, such as cryo-electron microscopy, spherical aberration electron microscopy, et al.

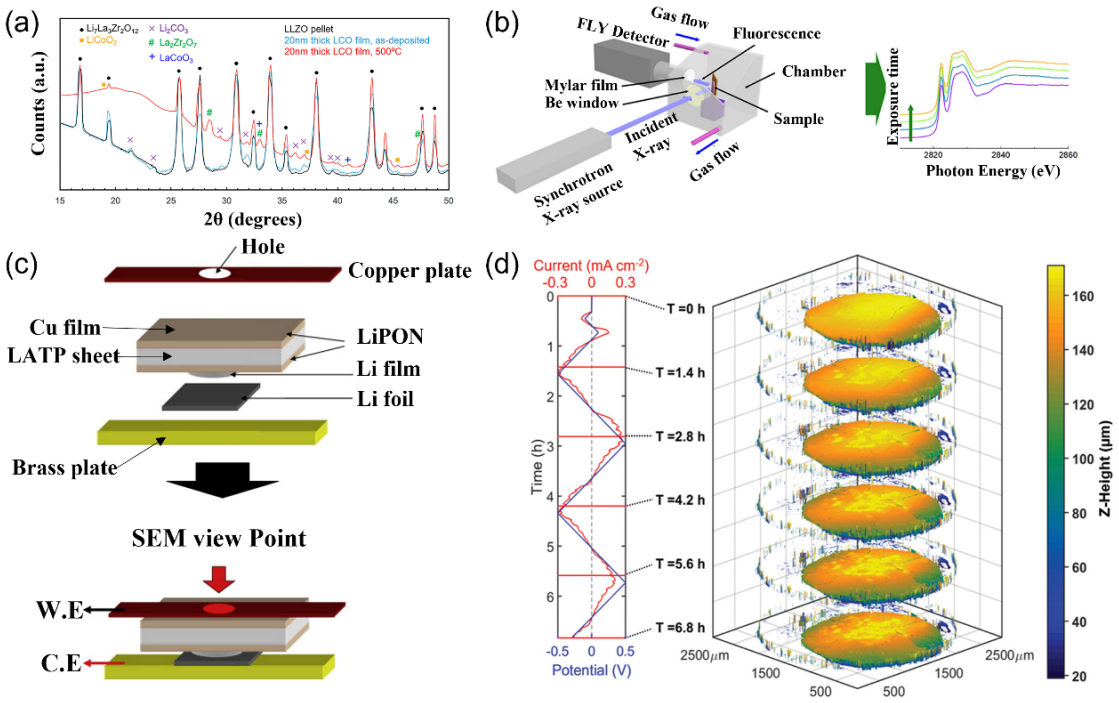

Figure 9. Advanced synchrotron/in-situ characterization (a) in-situ XRD to detect side-production in the interface between $LiCoO_2$ electrode and LLZO electrolyte. Reproduced by permission.[188] Copyright 2018, American Chemical Society. (b) in-situ XANES to detect degradation reaction of Li_3InCl_6. Reproduced by permission.[192] Copyright 2020, American Chemical Society. (c) in-situ SEM to characterize growth of lithium metal dendrites. Reproduced by permission.[197] Copyright 2013, Elsevier. (d) in-situ X-ray tomography to monitor the real-time three-dimensional morphology of the LGPS solid electrolyte. Reproduced by permission.[198] Copyright 2020, Wiley-VCH.

Chapter 5

5. Summary, challenges, and perspectives

5.1 Summary

Although one of the most mature battery technologies, lithium batteries still have many aspects that have not reached the desired requirements, such as energy density, current density, safety, environmental compatibility, and price. Through the combination of characterization technology, 2DMs, and advanced fabrication method, ASSLBs have gradually approached liquid lithium batteries in terms of electrochemical performance. Overall, advanced characterization technology has continuously deepened the understanding of 2DMs, and the application of 2DMs in ASSBLBs has also become diversified, playing different roles in different components.

5.2 Challenges and perspectives

Despite the advanced and increasing research work of 2DMs in ASSLBs summarized in this review, the application of 2DMs in ASSLBs is still in the initial state. There are still many serious problems in the practical application of ASSLBs, such as lithium-ion transport, high interface resistance, and side production. In order to maximize the role of 2DMs in ASSLBs, some proposed directions are discussed below.

(1) Modification of 2DMs

2DMs can be modified by multiple methods such etching and surface functionalization to further improve the electrochemical performance. In the research mentioned in the review, most 2DMs are applied directly in the ASSLBs. As a result, in order to maximize the role of 2DMs in ASSLBs, it is necessary to investigate the relationship between modification and electrochemical performance. For ASSLBs, it is mostly considered for improvement for the lithium metal battery which has highest energy density in lithium battery. For the anode side, it is necessary to enhance the chemical stability, mechanical strength of 2DMs to suppress the side-reaction between lithium metal anode and growth of the lithium dendrites. For the cathode side, it is little study on the high-voltage cathode material such like: $LiNi_{0.8}Co_{0.1}Mn_{0.1}O_2$, $LiCoO_2$, et al. on the ASSLBs. It is important to modify the 2DMs to deal with side-reaction between high-voltage cathode material and electrolyte. After solving this problem, it can further improve the energy density of ASSLBs. For electrolyte, modified 2DMs can provide a comprehensive solution to the low ion conductivity of ASSLBs at room temperature, especially polymer-based solid electrolytes.

(2) In-situ/operando characterization of the lithium-ion transport of 2DMs in SSEs

In situ/operando characterization technology can enhance scientists' understanding of the nature of some phenomena in ASSLBs. For electrolyte, since the introduction of solid lithium-ion conductors, the current mechanism of lithium-ion transport based on pure SSEs has been interpreted by various models. However, with addition of 2DMs, the mechanism of lithium-ion transport in the SSEs has been adjusted, which is necessary to understand the difference of the mechanism of lithium-ion transport in the SSEs with/without the addition of 2DMs. To achieve this goal, advanced methods such as in-situ/operando NDP, XTM, and simulation methods such as DFT and AIMD could analyze

the composite material systems, which should be applied here to analyze the mechanism of lithium-ion transport. For the interface problem between electrolyte and anode, in-situ/operando characterization can be applied to reveal the change of the interface component morphology during the battery operation, to take corresponding measures to improve the interface dynamics of the ASSLBs.

(3) Development of novel 2DMs

Although current 2DMs play an important role in ASSLBs, the novel 2DMs with excellent electrochemical activity should be continually developed. For instance, in the anode side, 2DMs with higher ionic conductivity and higher mechanical strength should be discovered. In the cathode side, novel 2DMs should have higher electronic conductivity and theoretical capacity. In the electrolyte, 2DMs require higher ionic conductivity, higher mechanical strength, etc. Based on the different requirements for different components of ASSLBs, machine learning and artificial intelligence can be very effective means to predict the application of new 2DMs for ASSLBs. These two technologies can greatly reduce the time required for people to screen materials in the early stage, which continues to promote the application of new 2DMs.

In conclusion, the application of 2DMs in ASSLBs is still preliminary. To promote the practical development of ASSLBs, more kinds of 2DMs and characterization methods for different aspects need to be further developed. With the assistance of new 2DMs and novel material fabrication method for ASSLBs, the application of 2DMs for the practical application of ASSLBs will be extended. The development of advanced characterization further reveals the failure mechanism of ASSLBs, which provides targeted guidance and ideas for 2DMs to solve the current problems encountered by ASSLBs. In short, the combination of 2DMs and ASSLBs is a hotspot for research and practical applications.

This work will promote the rapid development of next-generation lithium batteries-ASSLBs to replace the current technology dominated by liquid batteries.

Chapter 6

6. COF-F based all-solid-state lithium metal battery

Although the research on traditional PEO electrolytes has been developed for many years, there are still unsolved problems. The design of composite electrolytes has always been a research hotspot due to its high practical significance and wide application range. However, the traditional design of composite electrolytes mainly focuses on increasing the mechanical strength of the electrolyte to suppress the growth of lithium dendrites and has rarely considered the interface problem. With the continuous development of new materials, scientists have more ideas for the direction of electrolyte modification and are no longer limited to some initial views.

As the one of the new 2DMs which is mentioned in the above section, COF is suitable to stabilize the lithium anode to promote the electrochemical performance of the ASSLBs. Compared with other 2DMs, COF has the core structure which allows the transport of the lithium-ion and et al. Therefore, I conducted a series of designs and experiments on COF composite electrolytes.

6.1 Introduction

Although LIBs are the promising energy storge device for the electric vehicles, portable electronics, there are still serval problems should be solved including the safety and energy density problems. For the safety problem, due to the flammable organic liquid electrolyte, the short-circuit of the battery can easily lead to the electrolyte burning and even explosion. For the energy density, the unnecessary mass provided by the separator

and excess electrolyte composition limits the rise in the overall energy density of the battery. However, solid-state electrolytes can deal with those issues perfectly. Thus, by pairing with Li metal as anodes, the obtained ASSLBs are considered as the most ideal candidates for next-generation high-energy-density energy storage systems. First, inflammable solid-state electrolytes can guarantee safety issues with lees flammable composition. Second, solid-state electrolytes have wide electrochemical window compared with organic liquid electrolyte, which can be compatible with high voltage cathode material.

However, there are several challenges is faced by PEO-based solid-state electrolyte. First, the low ionic conductivity (10^{-6}–10^{-8} S cm^{-1} at room temperature) limits the fast charge and discharge capability of the battery. Second, the growth of lithium dendrites will cause the short circuit of the battery due to the low mechanical strength of PEO, Third, the incompatibility between solid-solid interfaces leads to huge interface impedance. Although many studies are currently addressing these issues, they are still not well resolved. Therefore, it is urgent to find ways to solve these problems.

Covalent organic framework (COF) as one of the rapidly developing porous materials and organic materials with high specific surface area, tunable chemical structure etc. Their rigid structures and periodic channels make them attractive as ion transport channel for dissociation of lithium ions. Due to the controllability of the pore structure of COF, it can be easily realized by adjusting the pore size, and the sieving effect of anions and lithium ions can be easily realized. There are also many reports showing that COF alone can act as a Li-ion conducting medium as a solid-state electrolyte. However, the number of studies based on this point is very small at present, and it has no practical significance due to the extremely poor contact between the COF electrolyte and the electrode interface.

Therefore, the composite solid electrolyte constructed with PEO and COF is one of the directions for the application of COF materials in all solid electrolytes in the future.

In order to deal with these challenges, our group applied covalent fluorinated organic framework (F-COF) as the skeleton in the PEO electrolyte to construct PEO/F-COF composite electrolyte. First, by the addition of COF, the mechanical strength of PEO/F-COF composite electrolyte is greatly enhanced. Second, The C-F bond with extremely low coordination ability with lithium ions can maximize the ability to sieve anions/cations without affecting the transport ability of lithium ions. Third, due to the high activity of Li metal, the cleavage of C-F bonds facilitates the construction of LiF-rich SEI layers, promotes the stability of Li metal anodes, and improves the most serious interfacial problems of solid-state batteries.

6.2 Discussion and results

Synthesis. The COF-F was initially synthesized through a solvothermal synthesis method. In detail, 1,3,5-triformylphloroglucinol (0.5 m mol, 105 mg) and 2,2'-bis(trifluoromethyl)-[1,1'-biphenyl]-4,4'-diamine(TFDB) (0.5 m mol, 163 mg), 5 ml of 1,4-doxane, 5 ml of mesitylene, and 2.5 ml acetic acid (3 M) were added into a Pyrex tube followed by 30 min. Wherein, acetic acid is used as a catalyst to catalyze the reaction. Since the reactants are easily oxidized in a high temperature environment, liquid nitrogen is used to quickly freeze the products after the ultrasonication is completed. Then use a vacuum pump for 5 min to ensure the vacuum environment in the Pyrex tube. Repeat this process three times. The tube was degassed and then heated at 120 ℃ for 72 h. The light-yellow precipitates were obtained and washed by acetone.

It was added to PEO at a mass ratio of 1%, and acetonitrile was added as a solvent to

dissolve into a uniformly distributed liquid. After the solid mass was calculated, the liquid was poured into a Teflon watch glass, and a film was formed after solvent evaporation using the casting method.

Characterization. Successful condensation and formation of β-ketoenamine bonds were confirmed by fourier transform infrared spectroscopy (FTIR). The FTIR spectrum of the obtained powder sample shows a new C-N stretch at 1298 cm^{-1}, corresponding to the β-ketoenamine C=C moiety, and the disappearance of the aldehyde peak around 1602 cm^{-1}, supporting the successful condensation of TP and TFDB (Fig. 10 c).[199] As shown in the Fig. 10, the prepared solid electrolyte membrane has excellent flexibility and ductility. Constant tumbling won't have much of an effect on the battery. The pouch cell made of COF-F composite electrolyte will also have good bending resistance.

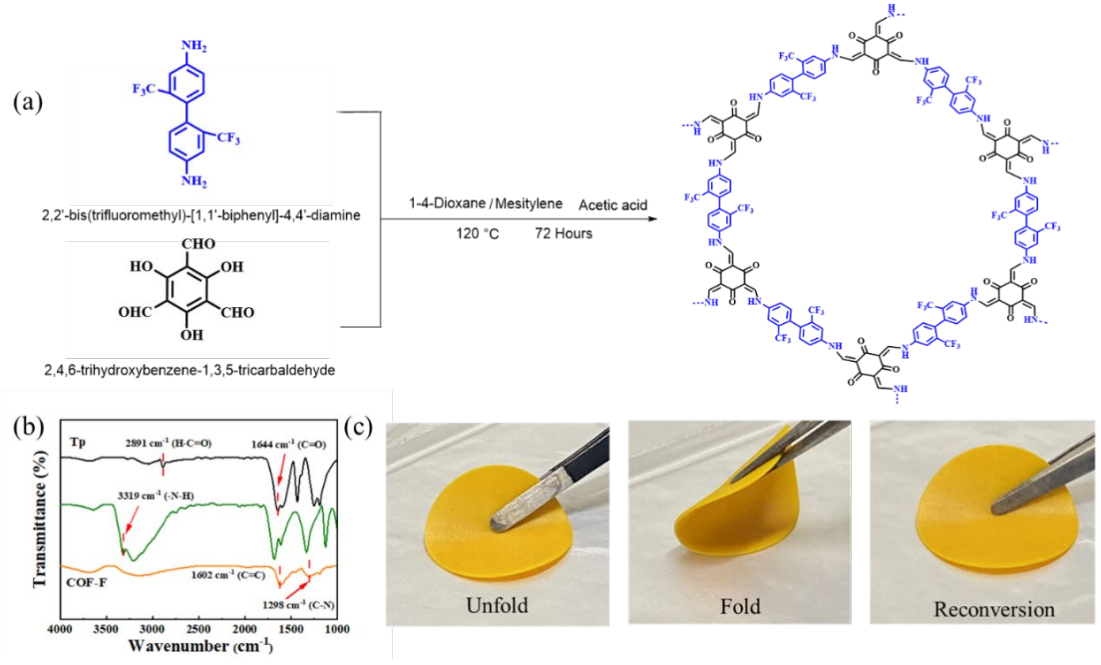

Figure 10. (a) synthesis process of the F-COF; (b) FTIR of the reactor and production; (c) flexibility ability test of the electrolyte.

Uniform deposition of Li^+. Compared with the lithium-ion transport in the conventional

PEO electrolyte, due to the addition of COF-F materials, the coordination environment during the lithium-ion transport process has changed. The solid-state ^{7}Li nuclear magnetic resonance (NMR) spectroscopy was recorded to probe into the effect of COF-F on Li^{+} environments (Fig. 11 b). Results show that a slightly broad single at -0.86 ppm is observed in the spectrum of PEO and then shifts to -0.79 ppm due to the existence of COF-F in PEO composite electrolyte, demonstrating that F in the core environment affects the Li^{+} coordination environment. The special lithium-ion coordination environment leads to more uniform deposition of lithium ions on the anode, which can be contributed to the great dissociation of anions and cations.

The improvement of the electrolyte-electrode interface by COF-F is the most fundamental reason to promote the uniform deposition of lithium metal. Compared with the PEO electrolyte, with the application of the COF-F, the uniform distribution of the COF-F can make the uniform distribution of the Li-flux in the lithium anode surface, which can significantly suppress the growth of the Lithium dendrites.

In order to observed the deposition of Li metal on the anode, SEM is applied to investigate the morphology of lithium anode after cycled 50th at 0.1 mA cm^{-2}. It is clear that the cycled Li with COF-F/PEO composite electrolyte shows a relatively smooth surface while the cycled Li with PEO electrolyte exhibits a rough surface along with dendritic-like Li metal formation, confirming that COF-F/PEO composite electrolyte can effectively induce uniform lithium deposition.

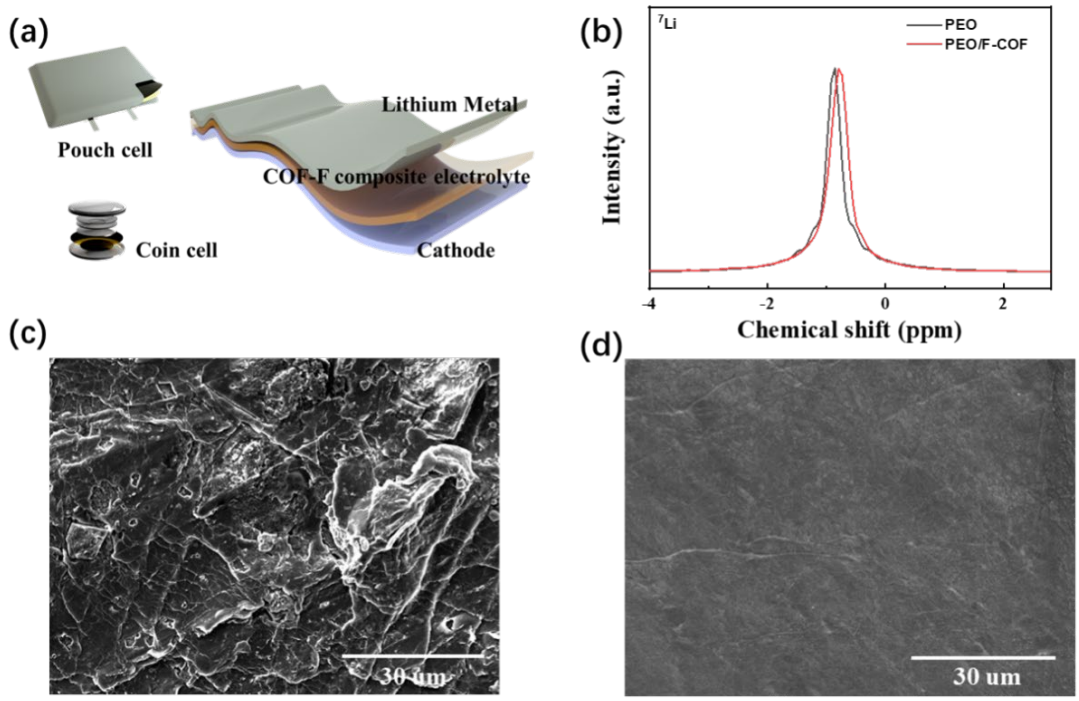

Figure 11. (a) the fabrication of the Li|LFP coin/pouch cell; (b) ^{7}Li solid-state NMR; SEM images of the cycled Lithium anode with (c) PEO electrolyte; (d) PEO/F-COF composite electrolyte.

The SEI composition. SEI is also one of the important components to contribute to the uniform lithium deposition. Owing to the high activity of lithium metal, in the process of charging and discharging, the solid electrolyte will spontaneously react with lithium metal to form a passivation layer, which is called SEI. A good SEI composition can enhance the uniform deposition of lithium metal. At present, most of the exploration of SEI components uses the ex-situ XPS technology. In order to explore the components as much as possible, here we use the in-situ technology to detect the components.

Since the base of the XPS has a thermocouple to control the temperature, the all-solid-state lithium metal battery can be operated in the cavity. However, due to the high vacuum environment of the conventional XPS, the melted PEO will be extracted, which

will affect the operation of the battery. As a result, near-atmosphere XPS (NAP-XPS) is applied to operate the in-situ device. NAP-XPS represents a revolution in the field, allowing for XPS characterization of a sample in a gaseous environment. This is achieved by containing the sample in a high-pressure cell that is only open to the analyses via a small aperture. A series of pumping stages after this aperture quickly reduce the pressure back down to high vacuum and limits the distance the electrons have to travel through a high pressure of gas. By placing the surface of the sample very close to this aperture, the area under analysis can be in a high pressure of gas while also allowing a usable fraction of the emitted photoelectrons to escape and reach the detector (Fig. 12a).

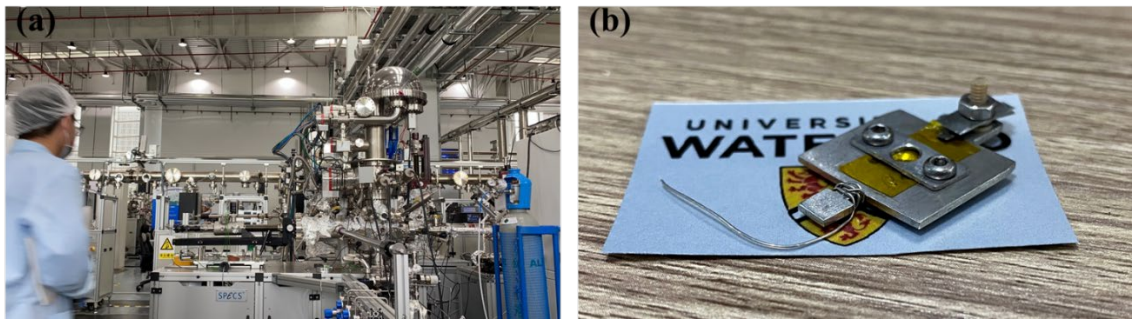

Fig. 12 (a) NAP-XPS equipment diagram; (b) in-situ cell design.

With addition of COF-F, the SEI which contains LiF, Li_3N-rich SEI has been constructed, promoting highly stable lithium metal anode. With the analysis of the XPS results, from C 1s data, the ratio of Li_2CO_3 is significantly higher in the PEO electrolyte, which can be attributed to the decompose of the PEO (Fig. 13a, b). Li_2CO_3 is one of the high machinal strength components in the SEI, which withstands huge volume changes to inhibit dendrite growth. However, it can be clearly seen that with the addition of the COF, the side-reaction of the PEO with lithium anode is significantly suppressed.[200] LiF is regarded as one of the great components of the SEI. LiF has extremely high ionic conductivity and electrochemical inertness and is very suitable as one of the stable SEI

components to ensure the transport of lithium ions while stabilizing the lithium metal anode. By the data from F 1s, it can be clearly seen that in the surface of the lithium anode after cycles, TFSI- and COF-F react on the highly reactive Li metal surface to form LiF with Li metal (Fig. 13c, d). The COF-F as an additional F element donor promotes the cycled lithium metal surface of the COF-F composite electrolyte to have a higher LiF composition. LiN_3 acts as a medium for conducting lithium in the SEI composition, which can guarantee the fast transport of lithium ions in the SEI, so it is also one of the important components in the composition of the SEI. In the Fig.13e, f, g, h, with the addition of COF-F, the content of LiN_3 is higher, combined with the phenomenon that the content of LiF in the SEI becomes higher, which indicate that the presence of COF-F promotes the decomposition of anions ($TFSI^-$).

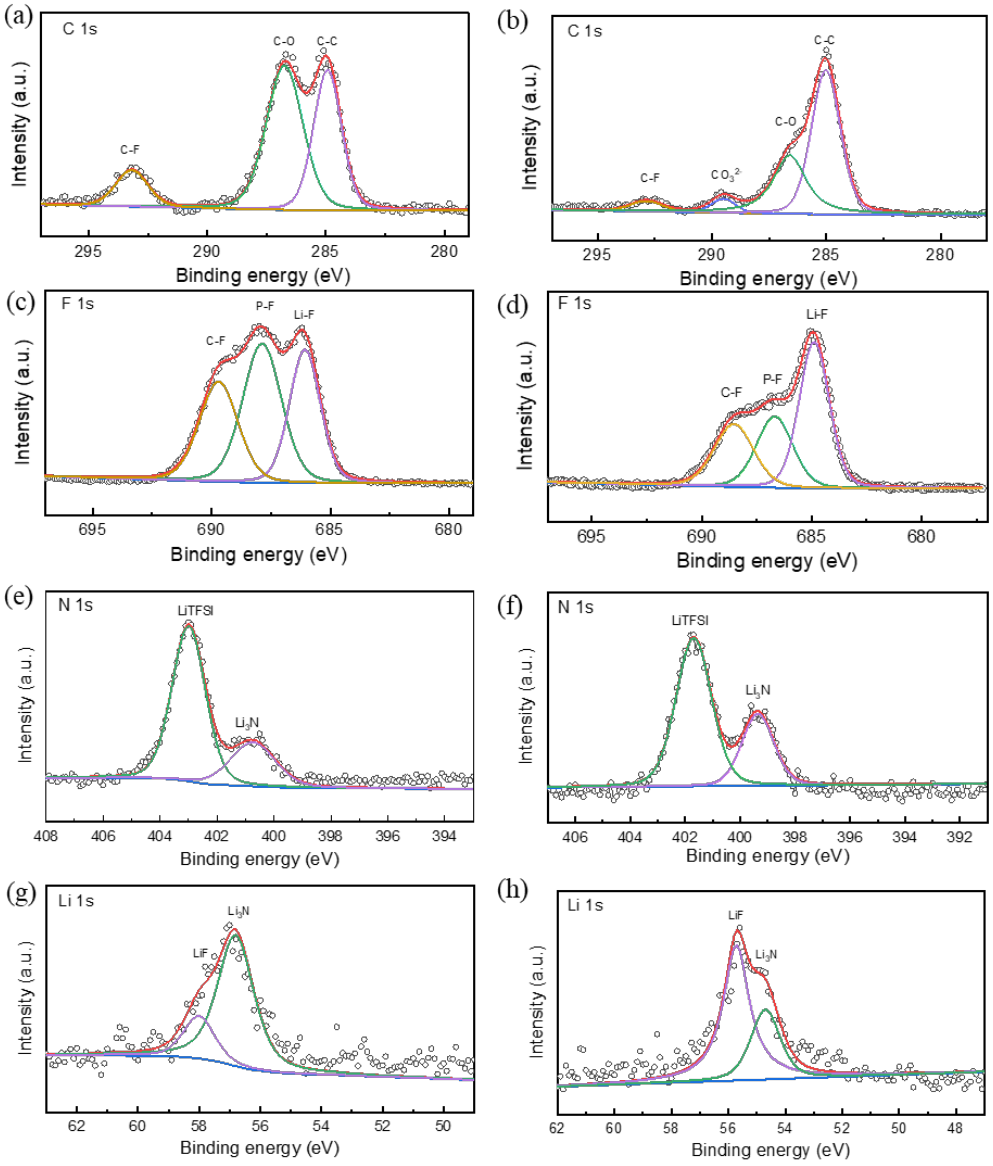

Figure 13. XPS for conventional PEO electrolyte for (a) C 1s; (c) F 1s; (e) N 1s; (g) Li 1s; of COF-F composite electrolyte for (b) C 1s; (d) F 1s; (f) N 1s; (h) Li 1s

In order to more intuitively observe the situation of SEI on the surface of Li metal anode, ToF-SMIS is applied to detect the SEI of two samples. From the Fig. 14a and Fig. 14b, it can be clearly seen that with the addition of COF-F, the density of SEI is higher, especially the content of LiF has obvious higher in the COF-F composite electrolyte, which is consistent with the results from XPS.

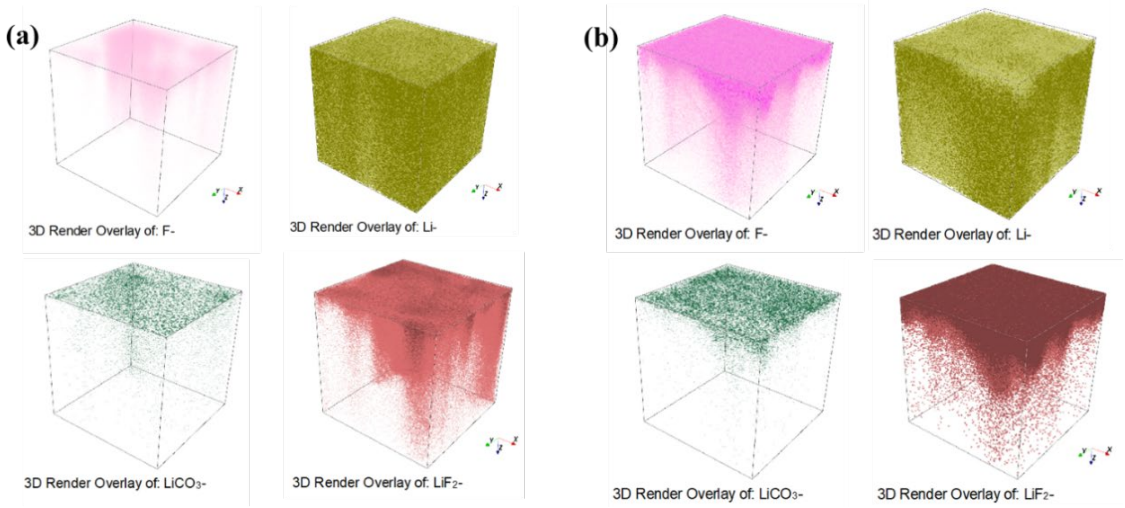

Fig. 14. ToF-SMIS for the distribution of lithium anode cycled in (a) conventional electrolyte and (b) COF-F composite electrolyte.

In order to test the stability of the lithium metal anode, the Li|Li symmetry cell is cycled at current density of 0.2 mA cm^{-2} (with areal capacity of 0.2 mAh cm^{-2}) for 1000 hours, which indicates the high reversibility for the lithium anode with COF-F composite electrolyte under 60 ℃. For Li|LFP battery, it exhibits stable charge/discharge over 400 cycles with 80% capacity retention. The pouch cell is also fabricated to test the practical meaning, which can power electronic clocks at room temperature (25 ℃). In addition, through the puncture test of the steel nail, the battery can still supply power normally. Compared with the liquid-electrolyte lithium metal battery, solid-state lithium metal demonstrates greater stability and security.

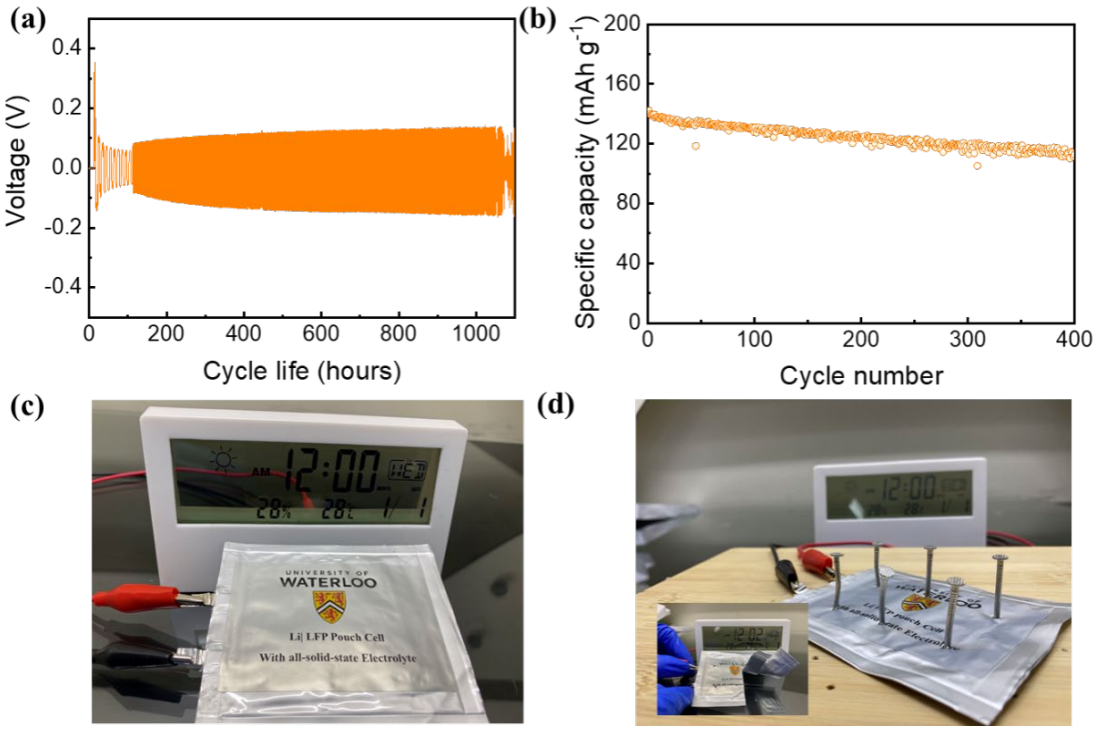

Fig. 15. (a) Li|Li symmetry cell battery; (b) Li|LFP coin cell; (c) practical demonstration of pouch cell; (d) the abuse experiment of Li|COF-F/PEO|LFP pouch cell.

6.3 Conclusion.

In summary, this project of the new design of the all-solid-state composite electrolyte provides new strategy to stabilize the lithium metal anode. On the one hand, as the donor of F element, COF is decomposed electrochemically on the surface of the lithium metal anode, and a LiF-rich SEI layer is constructed. On the other hand, the uniformity and pore distribution of the COF material itself can promote the uneven distribution of lithium ions to form uniform distribution on the surface of the lithium metal anode and promote the uniform deposition of lithium metal. As a result, the symmetric cell with COF-F composite electrolyte exhibits stable stripping/plating behaviour and the as-developed ASSLBs presents superior cycling stability with a capacity retention of 80% after 400 cycles at 0.5 C.

Chapter 7

7. Heterogeneous nanodomains electrolytes for ultra-long-life all-solid-state lithium-metal batteries

In the chapter 6, the novelty is the application of COF in the traditional PEO-based electrolyte. This physical mixing has very good practical significance for the design of electrolytes. However, from a chemical point of view, it is also very meaningful to redesign PEO-based electrolytes, which can more intuitively observe the effects of different functional groups on the stability of lithium metal anodes. At the chemical level, it is of great significance for lithium metal anodes to redesign and modify the segments of PEO.

7.1 Introduction

The inherent flammability, volatility, and thermal instability of liquid electrolytes are considered major causes of battery safety concerns, especially in the pursuit of high-energy-density lithium-ion (Li-ion) batteries.[29,201–203] Solid-state electrolytes (SSEs), benefiting from their high thermal stability, low manufacturing cost, and high safety, have attracted extensive attention. Thus, by pairing with Li metal as anodes, the obtained all-solid-state lithium-metal batteries (ASSLBs) are considered as the most ideal candidates for next-generation high-energy-density energy storage systems.[204–208] Among the various SSEs, solid polymer electrolytes (SPEs), especially poly(ethylene oxide) (PEO)-based SSEs, show a promising prospect in terms of their facile processability and good electrode/electrolyte interfacial compatibility.[209–211] However, the PEO-based SSEs

suffer insufficient Li^+ conductivity (10^{-6} S cm^{-1} at room temperature) and mechanical strength.[212,213] To well-address this defect, multiple design strategies have been applied, including heterogeneous SPE strategies to construct multiblock copolymers by coupling rigid polymer chains with flexible PEO chains, to enhance the Li^+ conductivity and maintain the mechanical strength.[214,215]

The multiblock copolymers possess the characteristic of phase separation, during which the flexible polyether chains can form nano-scale domain structures with a feature of ultra-low crystallinity and fast thermal movement.[216,217] Specifically, the Li^+ transport in traditional PEO-based SSEs is based on the hopping of Li^+ between ether oxygens (EO) sites, where the rate of hopping closely associates with the thermal movement of PEO chains.[218–220] For heterogeneous SPEs, the modified PEO nanodomains with fast chain kinetics can release more EO sites for ionic conduction segregated at the interface of conductive and non-conductive nanodomains, leading to a faster diffusion rate.[221] Recently, heterogeneous SPE strategy based on polystyrene (PS)-PEO has been reported to exhibit acceptable toughness and high ionic conductivity, but they still suffer from uncontrollable dendrite growth, weak mechanical strength, and discontinuous Li^+ diffusion channels due to the use of plasticizers.[214,222,223] It is critical to create plasticizers-free heterogeneous SPEs for regulating the size and order of nanodomains to achieve both decent channel consecutiveness and ion conduction. As brand-new commercial multiblock copolymers, poly(ether-block-amide) (Pebax) materials are made up of rigid polyamide blocks and flexible polyether blocks, without the need for plasticizers. The toughness of polyamides and the flexibility of polyethers are well maintained, and they also can be compounded with polymer salt to lower the surface resistivity.

Herein, we report a straightforward process to prepare the heterogeneous nanodomains electrolytes (HNEs) for ASSLBs *via* Pebax based multiblock copolymers made of rigid polyamide (PA) chains and flexible PEO chains, which possess a high ionic conductivity (4×10^{-4} S cm^{-1}) and suitable mechanical strength. After the solvent evaporation-induced phase separation and dynamic optimization by the LiTFSI salts, the formed PEO nanodomains contribute to ordered transport channels and PA chains facilely immobilize the anions of LiTFSI, which eventually facilitate fast Li-ion conduction and regulate the uniform deposition behavior. Furthermore, the obtained thin and dense organic-inorganic hybrid solid electrolyte interface (SEI) layer, as well as potent mechanical strength of Pebax HNEs, can synergistically suppress the dendrite growth, triggering dendrite-free Li metal anode. Attributed to these structural features, the all-solid-state Li/$LiFePO_4$ (LFP) and Li/$LiNi_{0.8}Mn_{0.1}Co_{0.1}O_2$ (NMC 811) batteries present excellent cycling stability. Our intriguing findings may stimulate the design of SSEs with novel conduction structures for next-generation ASSLBs.

7.2 Physicochemical properties of Pebax HNEs

The chemical structure and Li^+ conduction mechanism of Pebax HNEs are shown in Fig. 16a. The electrolyte membranes were obtained by incorporating LiTFSI into Pebax through a facile solution casting method, which is donated as Pebax HNE (x) (x = 18, 16, 14, 12, 10, and 8, representing the ratio of EO: Li). The as-prepared electrolytes present a flexible and dense structure with a thickness as thin as about 48 μm (Fig. 16b and Supplementary Figs. 2-3). EDS mapping results reveal that LiTFSI is homogeneously distributed in Pebax HNEs. To probe into the phase-separated structure of the electrolyte membranes, a small-angle X-ray scattering (SAXS) measurement was performed (Fig.

16c). The Pebax without LiTFSI (noted as Pebax (no Li)) exhibits an obvious scattering peak, confirming the formation of PEO nanodomains *via* solvent evaporation-induced phase separation, while the homopolymer PEO without LiTFSI (noted as PEO (no Li)) presents no such structure. Then, the crystallinity of electrolytes is observed with XRD measurement (Supplementary Fig. 4). In contrast to PEO (no Li), Pebax (no Li) displays extremely lower crystallinity, which further decreases with the addition of LiTFSI. It's worth noting that the crystallization peak of PEO nanodomains in Pebax HNE (12) is almost unobservable. Besides, the crystallinity of Pebax with varying LiTFSI content was also explored. As the LiTFSI content increases, the crystalline region of the PA chain (15°-28°) is destroyed[224], and when EO: Li reaches 8:1, the crystallization peak of LiTFSI appears, indicating the over-saturation and precipitation of LiTFSI in Pebax HNEs. The relevant phase transition behavior and chain motion of electrolytes were detected by DSC in the temperature range of -80 to 250 ℃. While in the low-temperature zone (-80-0 ℃), the Pebax (no Li) displays a glass transition temperature (T_g) of -52.4 ℃ (Supplementary Fig. 5), which is slightly higher in comparison to that of PEO (no Li) (-54.1 ℃). Upon the addition of LiTFSI, the T_g of electrolytes is remarkably elevated to -29.4 ℃ (Pebax HNE (12)) and -39.5 ℃ (PEO) respectively, manifesting that the involvement of LiTFSI facilitates the mobility of chains. Notably, the Pebax chains experience higher mobility than that of PEO. In the high-temperature zone (0-250 ℃) (Fig. 16d), the Pebax (no Li) exhibits two melting temperatures (T_m), which belong to PEO chains (16.6 ℃) and PA chains (206.5 ℃), respectively. In addition, the T_m of PEO chains in Pebax HNE (12) disappears, indicating that the crystalline PEO is completely transformed into an amorphous phase (Supplementary Table 2). More specifically, the participation of LiTFSI inhibits the crystallization of polymer chains, which is precisely consistent with the result

of XRD patterns. Compared with PEO (52.3 ℃), the PA chains in Pebax HNE (12) are demonstrated with a higher T_m of 123.8 ℃, indicating its excellent thermal stability and is capable of maintaining its solid-state in a wider temperature range. Furthermore, the tensile test of as-prepared electrolytes was performed to explore the mechanical properties of Pebax HNEs. As shown in Supplementary Fig. 6, with continuous addition of LiTFSI, the mechanical performance of Pebax HNEs slightly degrades, but still displays an overwhelming advantage over PEO. Pebax HNE (12) shows the stress of 6 Mpa, about 3 times higher than that of PEO. The involvement of LiTFSI interferes with the crystallization of the PA chains in Pebax HNEs , directly leading to a decline of mechanical strength. Hence, the varying trend of the mechanical properties of Pebax HNEs is consistent with its crystallinity.

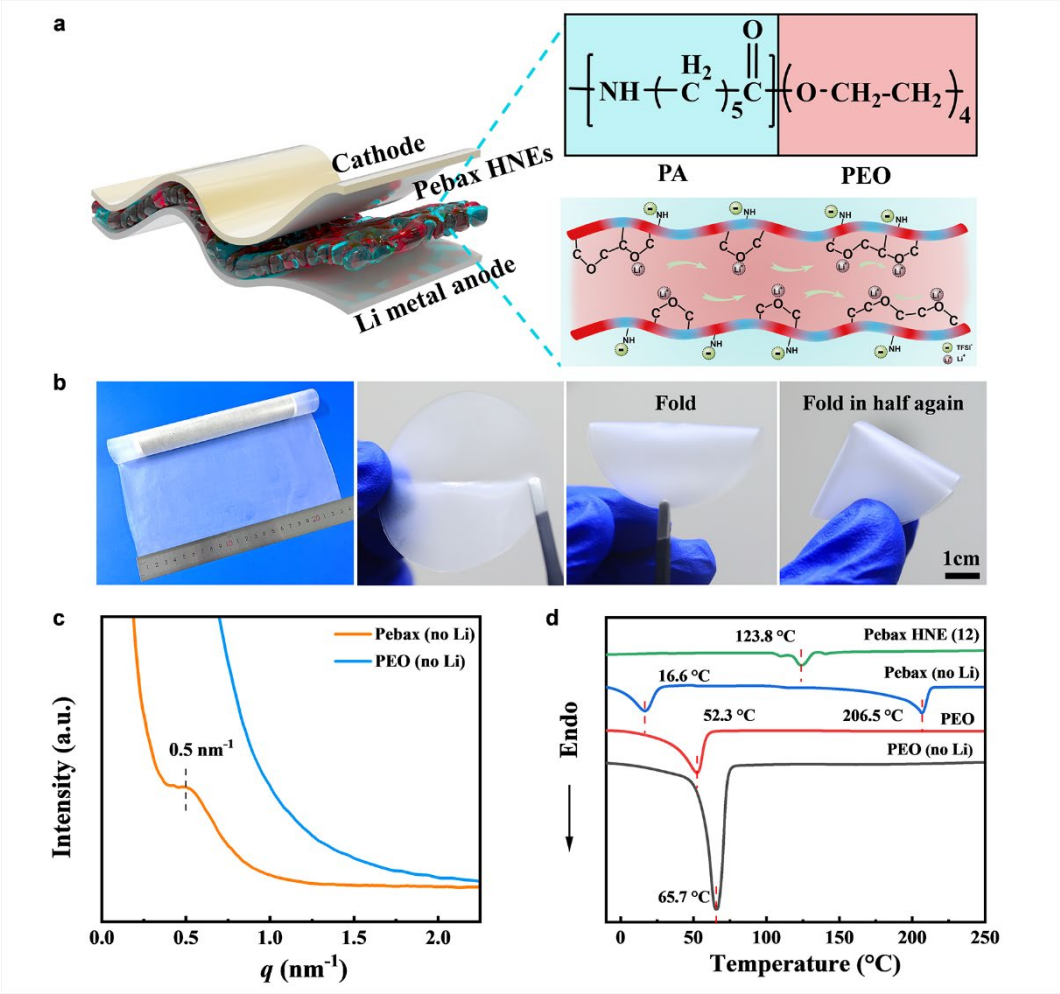

Fig. 16 Physicochemical properties of Pebax HNEs. (a) Chemical structure and Li^+ conduction mechanism, (b) photographs of Pebax HNEs, (c) SAXS and (d) DSC curves of Pebax and PEO membranes (with and without LiTFSI).

7.3 Electrochemical/kinetic behavior of Pebax HNEs

The segregated PA and PEO chains in Pebax HNEs play a crucial part in altering the size and order of nanodomains, thereby regulating the Li^+ conductivity and improving the electrochemical performance of SSEs.[225,226] To explore the tunability of conductive nanodomains, Pebax HNEs with different LiTFSI contents were prepared and characterized by SAXS (Fig. 17a, Supplementary Fig. 7, and Supplementary Table 3).

When the ratio of EO:Li increases to 12, the intensity of Pebax HNEs gradually increases, corresponding to the formation of more ordered nanodomains[227], whereas Pebax HNE (10) is not observed due to its weak mechanical strength. The regulation of nanodomains for conductivity enhancement is further revealed by EIS analysis. Fig. 17b shows the EIS spectra of Pebax HNEs with different LiTFSI contents at a temperature range between 30 and 90 ℃. All electrolytes display enhanced ionic conductivities when the temperature is elevated. Among them, Pebax HNE (12) shows the highest Li^+ conductivity of 4×10^{-4} S cm^{-1} at 60 ℃, which is higher than that of PEO. The decent ion conductivity can be ascribed to the Li^+ rapid conduction channel formed by the amorphous conductive nanodomains of PEO. Thus, the Pebax HNE (12) is set as the invariant in the subsequent investigation. However, the Li^+ conductivity undergoes an obvious decline when the ratio of EO:Li exceeds 12, attributing to the over-saturation of LiTFSI that hinders the Li^+ conduction. In addition, the Li^+ migration ability in Pebax HNEs was also estimated by activation energy (E_a) *via* Vogel–Tamman–Fulcher (VTF) model (Supplementary Fig. 8). With the increase of LiTFSI contents, the E_a gradually decreases to as low as 0.126 eV (Supplementary Table 4), which indicates the lowest energy barrier for Li^+ transfer in Pebax HNE (12). Interestingly, the E_a of Pebax HNEs turns out lower than that of PEO, demonstrating that the Li^+ migration ability in PEO nanodomains is superior to that in PEO. Besides, the ion-conductive channel in Pebax HNE (12) is benefit to Li^+ rapid conduction, which is consistent with the EIS results. The electrochemical stability window of the electrolyte is a critical parameter for implementing high-energy-density batteries, thus, the linear sweep voltammetry (LSV) measurements at 60 ℃ were provided to evaluate the electrochemical stability of SSEs. As reported in Fig. 17c, the oxidative stability of Pebax HNE (12) is over 4.38 V, obviously higher than PEO (around 3.8 V).

The increased voltage is attributed to the reduced contents of terminal hydroxyl groups in PEO chains blocked by PA chains, which contributes to the satisfactory electrode/electrolyte interfacial compatibility of Pebax HNEs.

To analyze the chemical interactions between Pebax and LiTFSI, the coordination environment of Li^+ was measured by Fourier-transform infrared spectroscopy (FT-IR). As illustrated in Fig. 17d, the characteristic bands of N-H and C=O present red-shifts, which are probably initiated by the interactions between LiTFSI and PA chains in Pebax HNEs and are further verified by the control experiments. Considering the chemical structure of PA and LiTFSI, it can be reasonably deduced that these interactions are contributed by the hydrogen bonding between -NH and $TFSI^-$, as well as the coordination between Li^+ and -C=O.[228,229] In addition, the C-O-C band at 1106 cm^{-1} weakens and shifts to lower wavenumbers with the addition of LiTFSI, which is attributed to the coordination between Li^+ and C-O-C (Supplementary Fig. 10).[230,231] Therefore, conclusions could be drawn that PA chains in Pebax HNEs can facilely coordinate with $TFSI^-$, regulating Li^+ coordination environments and facilitating the dissociation of Li^+−$TFSI^-$ ion pairs. The solid-state ^7Li nuclear magnetic resonance (NMR) spectroscopy was recorded to probe into the effect of PA chains on Li^+ environments (Fig. 17e). Results show that a slightly broad single at ~3.39 ppm is observed in the spectrum of PEO and then shifts to ~3.16 ppm due to the existence of PA chains in Pebax HNE (12), demonstrating that PA chains affect the Li^+ coordination environment. Moreover, the saturation recovery study reveals a faster Li^+ dynamics in Pebax HNEs with a T_1 relaxation time[179,232] of 0.3406 s for Pebax HNE (12) and 0.4156 s for PEO (Fig. 17f), further indicating that PA chains coordinate with $TFSI^-$ and consequently increase the concentration of mobile Li^+ in Pebax HNEs.

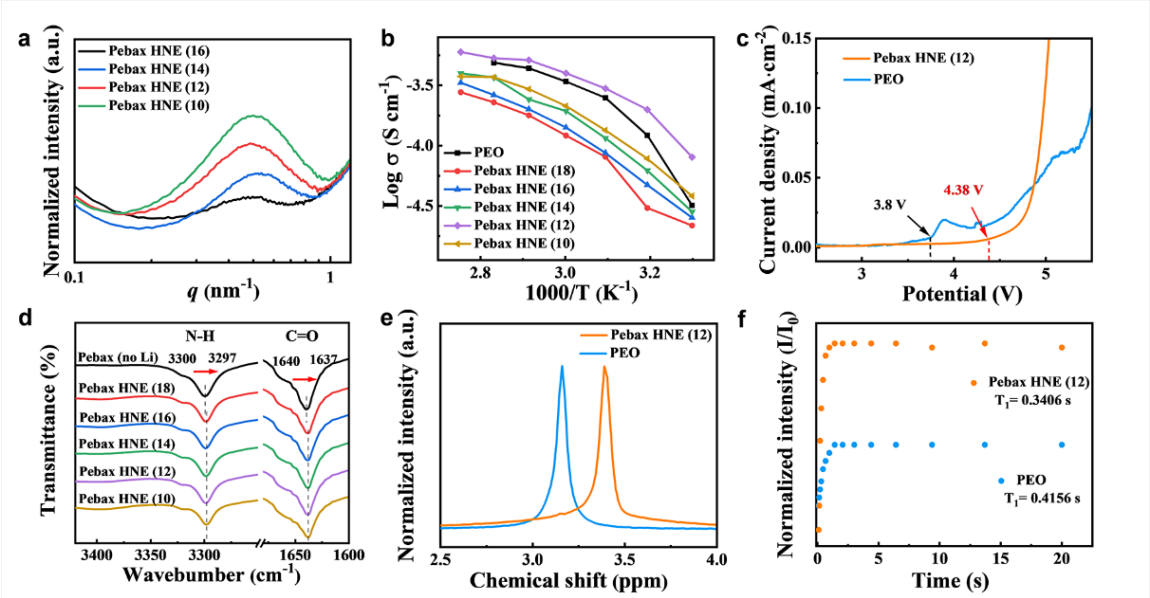

Fig. 17 Electrochemical features of Pebax HNEs. (a) SAXS of Pebax HNEs. Arrhenius plots (b) and LSV curves (c) of PEO and Pebax electrolytes. (d) FT-IR spectra of Pebax HNEs. ^{7}Li NMR spectrum (e) and corresponding saturation recovery plots (f) of PEO and Pebax electrolytes.

To further explore the structure of nanodomains, the interactions between polymer and LiTFSI, and the kinetic properties of Li^+ transfer in electrolytes, the molecular dynamics (MD) simulation were conducted. Results show that the agglomeration morphology of PEO nanodomains (represented by green cycle in Fig. 3b) is formed in Pebax HNE (12) and shows an interconnected structure (Fig. 18a, b), which is contributed to the formation of rapid and coherent Li^+ transport pathways. However, no such structure is seen in PEO SSEs (Fig. 18c), which is in agreement with the SAXS results. Furthermore, the Li^+ coordination environment in electrolytes is simulated and shown in the type of radial distribution functions (RDF) and total interactions energy. As shown in Fig. 18d, the RDF of Li-(C=O) exhibits a sharp peak and close to Li-(C-O-C) with the position (about 2.3 Å) lower than that of Li-TFSI (about 3.5 Å), suggesting that Li^+ in

Pebax HNE (12) are solvated and wrapped by the PEO nanodomains and the C=O in PA chains. In addition, the g(r) value of Li-(C-O-C) and Li-(C=O) in Pebax HNE (12) is slightly higher than that Li-(C-O-C) in PEO (Fig. 18e), indicating that the existence of PA chains contributes to the dissociation of LiTFSI. The total interaction energy (Supplementary Fig. 13 and Supplementary Table 5) also verifies that the interaction between -NH and $TFSI^-$ endows PA chains with potent immobilization of $TFSI^-$, contributing to the dissociation of LiTFSI and providing more free Li^+ in Pebax HNE (12). Furthermore, the interaction between Li^+ and C-O-C/C=O in Pebax HNE (12) is stronger than that of Li^+ with C-O-C in PEO, suggesting the unstable coordination structure of Li^+ with C-O-C/C=O, which is conducive to the faster diffusion of Li^+. Meanwhile, a quantitative characterization of Li^+ mobility in the transport process *via* the mean square displacement (MSD) is simulated (Fig. 18f and Supplementary Fig. 14). The MSD results report that Li^+ in Pebax HNE (12) significantly exceeds that in PEO, strongly indicating a higher diffusivity of Li^+ in Pebax HNE (12), which should be related to the fast thermal movement of amorphous nanodomains of PEO in Pebax HNE (12). This is consistent with above EIS and NMR results and further verifies the fast Li^+ conductive dynamics in Pebax HNE (12). The simulations snapshots (Fig. 18g, h) of Li^+ conductivity in electrolytes show that the diffusion of Li^+ in the interconnected PEO nanodomains in Pebax HNE (12) is remarkably faster than that in homopolymer PEO. Both MD simulations and experiments show that the interconnected PEO nanodomains in Pebax HNEs with fast chain thermal movement are conducive to achieving rapid Li^+ conduction.

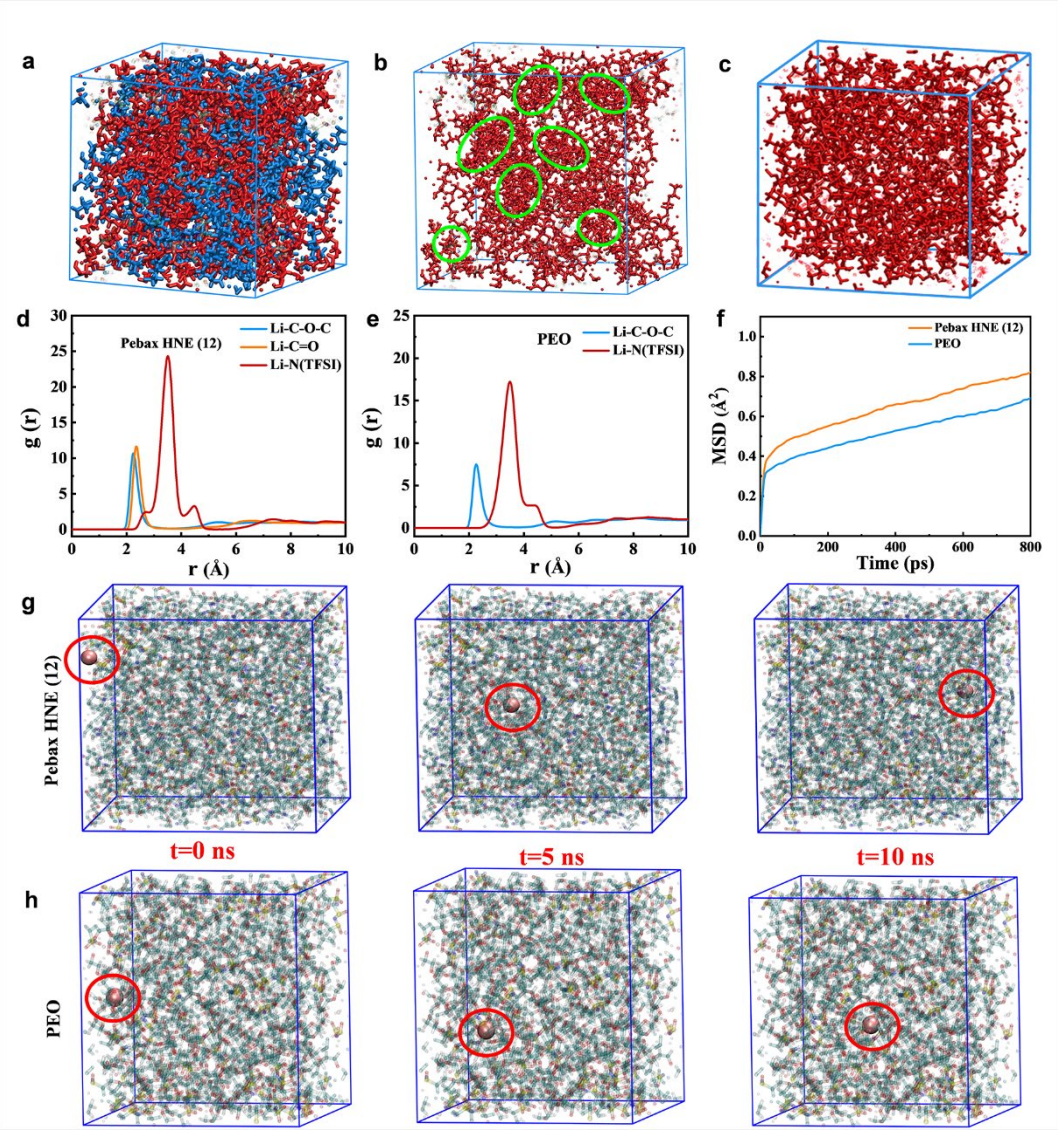

Fig. 18 MD simulations of the Pebax HNE (12) and PEO. (a) The agglomeration structure (a), and the corresponding PEO nanodomains in Pebax HNE (12) (b) and PEO (c), where PEO chains, PA chains are highlighted by red and blue, respectively. RDF of Li to C-O-C/C=O/N(TFSI) in Pebax HNE (12) (d) and Li to C-O-C/N(TFSI) in PEO (e). f, MSD of Li^+ and F atoms in Pebax HNE (12) and PEO. Simulation snapshots at 0, 5, and 10 ns for sets of Pebax HNE (12) (g) and PEO (h) simulation box present the Li^+ transfer process.

7.4 Evaluation of Li stripping/plating behavior

The impact of PEO conductive nanodomains in Pebax HNEs on Li^+ deposition and dissolution process were further identified. As such, symmetric cells were assembled and cycled at 0.1 mA cm^{-2} (with areal capacity of 0.1 mAh cm^{-2}) under 60 ℃ to investigate the ability of as-prepared electrolytes to restrain the nucleation and growth of Li dendrite (Fig. 19a). The PEO symmetrical cell is short-circuited around 170 h cycling while the Pebax HNE (12) symmetrical cell can stably cycle over 3200 h and still maintains the similar polarization voltage, indicating its stable stripping/plating behaviour. The Galvanostatic nucleation overpotential voltage profiles were performed by asymmetric cells composed of Li/Pebax HNE (12)/Cu and Li/PEO/Cu at a current density of 0.1 mA cm^{-2} (Fig. 10b). The cells exhibit similar nucleation overpotentials, proving that the presence of PA chains in Pebax HNE (12) does not significantly increase its nucleation energy barriers. At the initial stage of Li deposition, Li^+ at the interface between Pebax HNE (12) and Cu preferentially nucleates with a consumption of Li below areal capacity of 0.01 mAh cm^{-2}, indicating the decent compatibility of Pebax HNEs. By contrast, the consumption of Li with areal capacity of 0.04 mAh cm^{-2} at the interface between PEO and Cu implies a severe side reaction existing between PEO and Li.[233] The morphology comparison of SSEs membrane obtained from symmetrical cells after 50 cycles was further explored by both optical and SEM observations, as shown in Fig. 19c, d. The Pebax HNE (12) after cycling is still intact and transparent with a smooth surface containing only a small amount of Li residue. However, a large amount of “dead” Li can be observed on the surface of the cycled PEO. What’s worse, poor mechanical strength of PEO makes it easily penetrated by Li dendrite, resulting in an uneven surface.

Furthermore, the ex-situ analysis of the Li metal electrodes in asymmetric cells was utilized to explore the dendrite inhibition capability of electrolyte membranes. The non-destructive synchrotron X-ray tomography were adopted to investigate the morphology of the Li surface after stripping/plating process. Two symmetric cells with Pebax HNE (12) and PEO were cycled 100 h at 0.1 mA cm^{-2} (with areal capacity of 0.1 mAh cm^{-2}). 3D reconstructed tomograms of the Li/Pebax HNE (12)/Li and Li/PEO/Li cells further reveal the interface morphological evolution of the cycled Li metal electrodes (Fig. 4e, f) with the gold volume elements representing the cycled Li electrodes. As shown in Fig. 19e, the 3D tomogram of the Li/Pebax HNE (12)/Li cell displays no dendrite growth on either side, indicating a homogeneous Li stripping/plating process. This should be related to the formation of uniform and fast PEO conductive nanodomains in Pebax HNE (12). Nevertheless, the Li/PEO/Li cell shows an evident dendrite growth and mossy Li formation in Fig. 19f. The heterogeneous stripping/plating of Li metal at the Li/PEO interface initiates a rapid growth of Li dendrites, which gradually penetrates the PEO membrane and eventually leads to a short-circuit. The above results demonstrate that Pebax HNE (12) can effectively suppress the growth of Li dendrite in comparison to PEO.

The uniform and coherent conductive nanodomains in Pebax HNEs are conducive to the uniform Li^+ deposition and interface stability between HNEs and Li metal. The surface morphology and chemical composition of Li metal electrodes were characterized by SEM and X-ray photoelectron spectroscopy (XPS) to probe into the deposition morphology and SEI component. Li metal electrode was evaluated after the 50th stripping/plating process under the current density of 0.1 mA cm^{-2} and areal capacity of 0.1 mAh cm^{-2}, using Pebax HNE (12) and PEO as electrolytes (noted as Li@Pebax HNE (12) and Li@PEO, respectively). As shown in Supplementary Fig. 15, Li@Pebax HNE

(12) shows a smooth surface while Li@PEO exhibits a rough surface along with dendritic-like Li metal formation, confirming that Pebax HNE (12) can effectively inhibit the Li dendrite growth. According to the F 1s, S 2p, N 1s, and Li 1s XPS spectra, the typical LiF, Li_3N, and Li_2S peaks were observed (Supplementary Fig. 16), which have long been recognized as the core components for stable Li^+ deposition and SEI in Li metal anode.[129,234] The N 1s spectra confirms the existence of -N-C=O on Li@ Pebax HNE (12), which is related to the decomposition of PA chains. The depth-dependent XPS analysis was also conducted to explore the composition distribution of SEI. As the depth deepens, the peak intensity of inorganic components (LiF, Li_3N, and Li_2S) increases while the peak of LiTFSI disappears, indicating the formation of SEI layer with the organic-inorganic feature. To further elucidate the structure and composition of SEI, time-of-flight secondary ion mass spectroscopy (TOF-SIMS) analysis was employed. Supplementary Figs. 17-18 and Fig. 19g, h display the depth profiles, overlays, and their corresponding 3D rendering of two chosen species, LiF_2^- and LiS^-, which are representatives of LiF and Li_2S, respectively. The high intensity of LiF fragments in the TOF-SIMS spectra confirms it as the leading component on the Li metal surface of SEI. Besides, Supplementary Fig. 17 reveals a higher LiF_2^- signal intensity in Li@Pebax HNE (12) than that in Li@PEO with the former firstly achieves a balance during the sputtering time, confirming the formation of a thinner SEI layer on Li@Pebax HNE (12). According to the 3D reconstruction of the sputtered volume for two species of interest, the SEI layer of Li@Pebax HNE (12) possesses distinct advantages of thin, dense, and uniform over Li@PEO. In one aspect, it verifies that HNEs with PEO conductive nanodomains benefit for homogenized Li^+ deposition and an eventual ultrathin and dense SEI. In another aspect,

the SEI layer is beneficial to decrease the resistance for Li^+ transfer across the interface and suppress Li dendrite formation during repeated stripping/plating process.[235]

From these findings above, three arresting conclusions can be drawn; firstly, the amorphous PEO nanodomains, formed by solvent evaporation-induced phase separation in Pebax HNEs, exhibit interconnected and highly ionic conductive features. The PA chains can facilitate the mobility of Li^+ by facilely coordinating with the anions of LiTFSI, which eventually permit the fast conduction and uniform deposition of Li^+. Secondly, Pebax HNEs, equipped with favorable mechanical strength, effectively inhibit the Li dendrite growth. Thirdly, the thin and dense organic-inorganic hybrid SEI and Pebax HNEs with suitable mechanical strength synergistically suppress the nucleation and growth of Li dendrite.

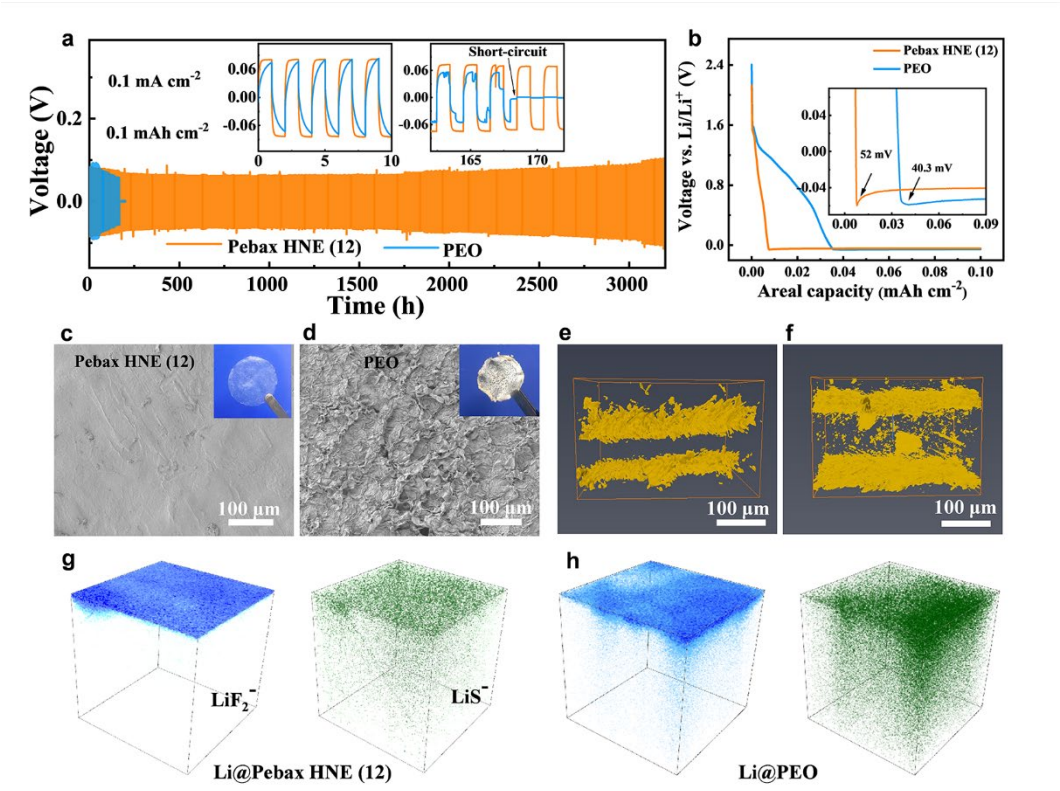

Fig. 19 Pebax HNE (12) and PEO in symmetric Li and asymmetric Li||Cu cells. (a)

The long-term cycling performance of symmetric cells. (b) Voltage profiles of the Li/Cu deposition process. The morphologies of electrolytes after cycled for Li/Pebax HNE (12)/Li (c) and Li/PEO/Li (d) cells, respectively. Cross-sectional synchrotron X-ray tomography 3D reconstructive tomograms of Li/Pebax HNE (12)/Li (e) and Li/PEO/Li (f) cells after cycling. TOF-SIMS 3D reconstruction of the representative species of SEI formed at the Li@Pebax HNE (12) (g) and Li@PEO (h). All the electrodes were prepared after 50th stripping/plating process.

7.5 ASSLBs performances

To evaluate the electrochemical performance of Pebax HNEs in practical application, ASSLBs with a commercial cathode of $LiFePO_4$ (LFP) were assembled and cycled at 60 °C. The Li/Pebax HNE (12)/LFP cell exhibits a discharge capacity of 153.6, 146.7, 133.9, 119.5, and 82.2 mAh g^{-1} under the current density of 0.1, 0.2, 0.5, 1 and 2 C, respectively (Fig. 19a). After switching back to 0.1 C, a high discharge capacity of 154.3 mAh g^{-1} can be recovered, implying the excellent capacity reversibility of Pebax HNE (12) (Supplementary Fig. 19). Remarkably, the ASSLBs exhibits excellent long-term cycle stability at 0.5 C and 60 °C. The Li/Pebax HNE (12)/LFP cell presents a discharge capacity retention of 80% after 1560 cycles with high Coulombic efficiency (CE) close to 100%, which is superior to previously reported PEO-based ASSLBs (Fig. 19b). Moreover, the stable charge-discharge curves reveal no obvious increase of overpotential, indicating the hyperstatic cycling property of Pebax HNE (12) (Fig. 19c). Conversely, the capacity of Li/PEO/LFP cell decays rapidly to 100 mAh g^{-1} after 300 cycles with a low CE, especially in the first 50 cycles, indicating the instability and incompatibility of PEO SSE. In addition, the rate and long-term performance of control cells of LFP/Pebax HNE

(14/10)/Li were shown in Supplementary Fig. 20 proving that ordered nanodomains enable fast Li^+ conduction and stable cycling of ASSLBs. Furthermore, the Li/Pebax HNE (12)/LFP cell cycled over 1000 cycles at 1 C and 60 °C with a discharge capacity retention close to 92%, which indicates the fascinating electrochemical stability and dendrite inhibition of Pebax HNE (12) (Supplementary Figs. 21-22).

In order to broaden the temperature range of Pebax HNEs in applications, the galvanostatic cycling performance of Li/Pebax HNE (12)/LFP cell at elevated temperature (70-90 °C) was also investigated. The cell reveals a higher discharge capacity of 151.3, 157, and 161 mAh g^{-1} at temperatures of 70, 80, and 90 °C, respectively (Supplementary Fig. 23). Even after long-term cycling at 1 C and 90 °C (Fig. 19d, e) an excellent discharge capacity retention of 74.2% after 800 cycles can still be achieved, which confirms the remarkable mechanical properties and electrochemical stability of Pebax HNE (12) at high temperature. Furthermore, the rate performance of Li/Pebax HNE (12)/LFP cell at 90 °C was also explored and eventually exhibit striking discharge capacities of 160.2, 154.6, 145.6, and 85.5 mAh g^{-1} at the rates of 0.2, 0.5, 1, and 2 C, respectively (Supplementary Fig. 24). In order to demonstrate the feasibility of Pebax HNEs to operate at higher voltage, the commercially cathode of $LiNi_{0.8}Mn_{0.1}Co_{0.1}O_2$ (NCM 811) was assembled and cycled at 60 °C. The Li/Pebax HNE (12)/NCM811 cell delivers a high discharge capacity of 155.4 mAh g^{-1} at 0.1 C and obtains a specific capacity of 124.3 mAh g^{-1} after 70 cycles with a high CE above 99.36% (Fig. 19f), verifying the decent compatibility of Pebax HNEs with NCM 811 and Li metal electrodes. In addition, the charge-discharge curve (Fig. 19g) witnesses a limited capacity decay during cycling, indicating that Pebax HNEs are well-compatible with high-voltage cathode materials. A comparison with the reported typical PEO-based SSEs in terms of

their cycling performance is illustrated in Supplementary Fig. 25 and Supplementary Table 6. The significant electrochemical performances, including long-lifespan, high-rate performance, *etc*., verify the enormous potential of Pebax HNEs for the application of ASSLBs.

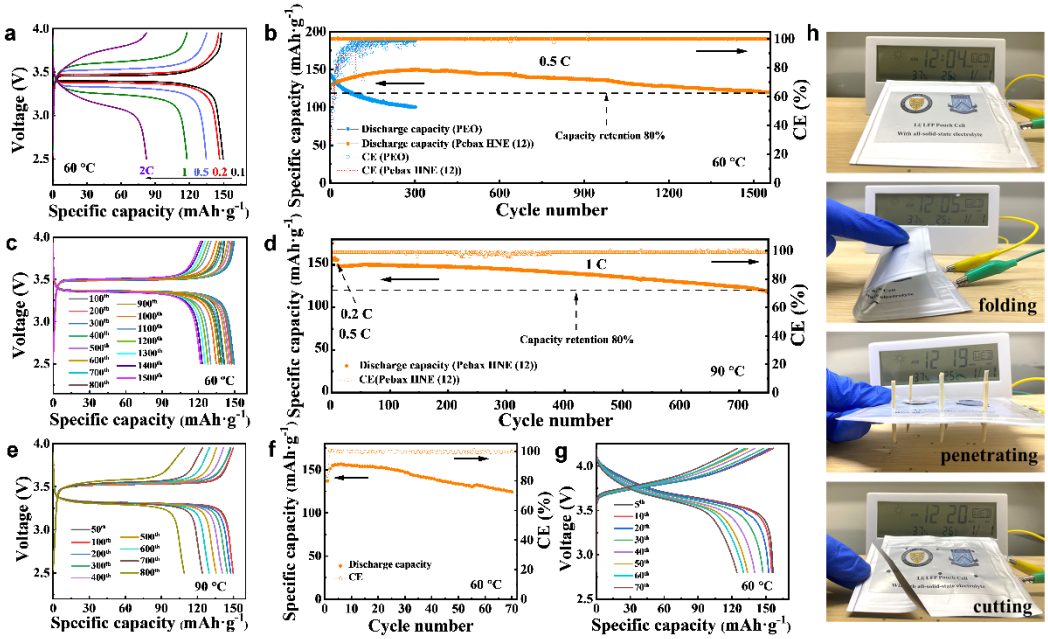

Fig. 20 The performances of ASSLBs. (a) Charge/discharge curves of Li/Pebax HNE (12)/LFP cell at different rates, cycled at 60 °C. Discharge specific capacity and CE (b) as well as Charge/discharge curves (c) of the Li/Pebax HNE (12)/LFP and Li/PEO/LFP cells at 0.5 C and 60 °C. Discharge specific capacity and CE (d) as well as charge/discharge curves (e) of the Li/Pebax HNE (12)/LFP cell at 1 C, under 90 °C. Discharge specific capacity and CE (f) as well as charge/discharge curves (g) of the Li/Pebax HNE (12)/NCM 811 cells at 0.1 C and 60 °C. (h) The abuse experiment of Li/Pebax/LFP pouch cell.

The practical application of ASSLBs cannot ignore the safety concern evaluation under pouch cell level. To evaluate the safety of ASSLBs, a pouch cell was assembled

and subjected to abuse testing. As shown in Fig. 19h, the all-solid-state pouch cell was connected to an electronic watch. After folding and unfolding, the electronic watch remains available, demonstrating the good flexibility of the pouch cell. Moreover, abuse tests including nail tests and cutting tests were also conducted. Notably, the treated pouch cell still supports the electronic watch to work even after being nailed 6 times and cut, which well indicates the reliability and safety of the pouch cell.

7.6 Conclusion

In summary, we introduce poly(ether-block-amide) (Pebax) strategies to construct heterogeneous nanodomains electrolytes (HNEs) for ultra-long-life ASSLBs. The PEO conductive nanodomains in Pebax HNEs, formed by the solvent evaporation-induced phase separation, exhibit interconnected as well as highly ionic conductive features. Then, PEO nanodomains construct ordered transport channels and PA chains facilely coordinate with the anions of Li salts, facilitating the fast Li^+ conduction and uniform Li^+ deposition. Additionally, a thin and dense organic–inorganic hybrid SEI is obtained *via* the reaction initiated between Pebax HNEs and Li metal, which decreases the Li^+ transfer resistance across the interface. The suitable mechanical strength of Pebax HNEs and hybrid SEI synergistically suppress the Li dendrite formation during repeated cycling. As a result, the symmetric cell with Pebax HNEs exhibites stable stripping/plating behaviour and the as-developed ASSLBs presents superior cycling stability with a capacity retention of 80% after 1560 cycles at 0.5 C. Our findings propose a brand-new insight to construct conductive nanodomains in SSEs for high-performance ASSLBs.

7.7 Methods

Materials and Fabrication. The Pebax heterogeneous nanodomains electrolytes (HNEs) were fabricated by first dissolving Pebax (Arkema) and Lithium bis(trifluoromethanesulfonyl)imide (LiTFSI) (Aladdin 99%) in mixed solvents of ethanol and water at 80 ℃. After that, the obtained solution was cast onto a PTFE dish and dried at room temperature for 24 h, followed by vacuum drying at 60 °C (24 h), 90 °C (24 h), and 120 ℃ (24 h) to evaporate the solvent. The Pebax HNEs with different LiTFSI contents (EO: Li=18:1/16:1/14:1/12:1/10:1/8:1) were prepared and donated as Pebax HNE (X), where X represents 18, 16, 14, 12, 10, and 8 respectively.

The polyethylene oxide (PEO, M_w=600000, Aladdin) electrolyte membrane was prepared by dissolving PEO and LiTFSI (EO: Li = 12:1) in anhydrous acetonitrile. The resultant solution was then cast onto a PTFE dish in an argon filled glove box. The PEO electrolyte membrane was dried at 30 °C for 24 h and followed by vacuum drying at 50 °C.

To prepare the $LiFePO_4$ (LFP) and $LiNi_{0.8}Mn_{0.1}Co_{0.1}O_2$ (NCM 811) electrodes: LFP or NCM 811, polyvinylidene fluoride (PVDF), and carbon black with a weight ratio of 80:10:10 were mixed in N-methyl-2-pyrrolidone (NMP) to form a homogeneous slurry. The slurry was mechanically stirred for 1 h and then cast on the carbon–coated aluminum foil. The cathode was further dried at 80 °C for 24 h under vacuum. The loading of electrodes active material is (2–4) mg cm^{-2}.

Structure and morphology characterization. The microphase separation structure of electrolyte membranes were characterized by small-angle X-ray scattering (SAXS) (Xenocs Xeuss 3.0) with a scan range of 0.07–3.8 nm^{-1}. The Pebax HNEs nanodomains spacing, L_0, is calculated by as $2\pi/q$, where q represents the scattering peaks. X-ray diffraction (XRD) was recorded by Brucker AXS D8 at a range of 5°~50° with Cu Kα radiation (λ=1.5406 Å). Differential scanning calorimetry (DSC) was collected by NETZSCH DSC 200F3 at 10 °C /min from -80~250 °C with N_2 atmosphere.

Mechanical testing was carried out on an Instron electroplus 1000 testing stain with a strain rate of 2 mm/min. The morphology and microstructure of electrolyte membranes were characterized by scanning electron microscope (SEM) (JEOL 7001F) equipped with an energy-dispersive microscopy

EDX spectrometer. Flourier transform infrared spectra (FT-IR) were recorded from 500-4000 cm^{-1} via a Thermo Scientific Nicolet iS50 instrument. Solid-state nuclear magnetic resonance (NMR) experiments were conducted using an JNM-ECZ 600 MHz NMR spectrometer at room temperature. Spin–lattice relaxation time (T_1) was measured employing a saturation recovery pulse sequence with 15 saturation pulses at recovery times varying from 0 to 20.0 s.

The cells were imaged using the non–destructive synchrotron X–ray tomography technique conducted at the tomography station at BMIT-BM line end station at BESSY II, Helmholtz–Zentrum Berlin, Canadian Light Sources, which makes it possible to directly visualize the three-dimensional electrode. Monochromatic hard X–rays with an energy of 20 keV ($\Delta E/E = 1.5\%$) were directed onto the sample. The transmitted X–rays were converted into the visible light by a scintillator (CdWO 4, 60 μm in thickness), which were then magnified by a set of microscope optics before projected on a CCD sensor (PCO4000 camera, 4008 × 2672 pixel). A (4.4 × 2.9) mm^2 field of view was used with a pixel size of 0.72 μm. During a rotation of 180°, 2200 projections and 230 flatfields with an exposure time of 1.6 s for each projection/flat field were collected. The 3D image reconstruction followed the same procedure as our previous report. Image segmentation was conducted using Image J/Weka followed by the visualization *via* VGSTUDIO MAX 3.1. All the symmetrical Li/polymer/Li cells were galvanostatic discharged (stripping) and charged (plating) using a Neware BTS400 multichannel battery testing system. After cycling, the cells were transferred to the beamline to conduct tomography without cell disassembly.

X–ray photoelectron spectroscopy (XPS, Thermo Scientific ESCALAB Xi+) was acquired by utilizing an Al Kα ($\lambda = 0.83$ nm, $h\nu = 1{,}486.7$ eV) X–ray source operated at 2 kV and 20 mA. The C 1s main peak at 284.6 eV was treated as the reference to calibrate peak shifts caused by the surface–charging effects. Time–of–flight secondary ion mass spectrometry (TOF–SIMS5-100) was employed to study the surface chemical composition of Li anode. For depth profiling, a Cs+ ion beam (1KeV ion energy, ~40 nA measured sample current) was used to sputter 80×80 μm^2 areas centered around the analyzed areas. All depth profiles were acquired in noninterlaced mode, namely sequential sputtering, and then analyzed.

Electrochemical measurements. All electrochemical measurements were carried out using a Bio-Logic electrochemical station. Electrochemical impedance spectroscopy (EIS) measurements were tested in a sandwiched Li ion blocking stainless steel electrodes in the frequency range of 1 MHz to 0.1 Hz with an AC amplitude of 10 mV under the temperature range from 30 °C to 90 °C. The linear sweep voltammetry was determined employing a Li |solid electrolyte| stainless steel model from 2.5 to 6 V at a scan rate of 1 mV/s.

All the cells were sealed in a 2032-coin cell for testing. A symmetric cell of Li |solid electrolyte| Li was employed for both interfacial resistance and interface stability of the composite polymer electrolyte against lithium electrode. The galvanostatic cycling was conducted at a current density of 0.1 mA/ cm^{-2} with charging and discharging for 1 h, respectively. A cell of Li |solid electrolyte| Cu, employed for monitoring the nucleation of Li, was conducted at a current density of 0.1 mA/ cm^{-2} with charging and discharging for 1 h, respectively.

The cycling and rate performance of all-solid–state batteries were determined on a Neware BTS400 instrument with 2.5-3.95 V (LFP) and 2.8-4.2 V (NCM 811).

Details of Molecular Dynamics Simulations

Classic molecular dynamics simulations were carried out to give an atom-level insight of the microstructure of the Pebax HNE (12) and PEO systems. The diffusion behavior of Li^+ in two systems was also studied. The molecular/polymer structures of LiTFSI, Pebax, and PEO are shown in the Supplementary Fig. 1. The simplified Pebax chain features 24 ethylene oxide units followed by 6 polyamide units while the simplified PEO chain contains 24 ethylene oxide units. The component and amount of the simulation system are listed in Supplementary Table 1. Both the initial configurations of mixture systems were constructed through the software of PACKMOL, all the molecules were randomly inserted in a cubic simulation box. The GROMOS54a7 force field was employed to describe the behavior of the molecules. The molecular force field consists of nonbonded and bonded interaction. The nonbonded interaction contains van deer Waals (vdW) and electrostatic interaction, which are described by the Equation 1 and Equation 2, respectively.

$$E_{LJ}\left(r_{ij}\right)=4\varepsilon_{ij}\left(\left(\frac{\varepsilon_{ij}}{r_{ij}}\right)^{12}-\left(\frac{\varepsilon_{ij}}{r_{ij}}\right)^{6}\right) \quad (1)$$

$$E_{c}\left(r_{ij}\right)=\frac{q_i q_j}{4\pi\varepsilon_o\varepsilon_r r_{ij}} \quad (2)$$

For different kinds of atoms, the Lorentz-Berthelot mix rules were adopted for vdW interactions, which follows the Equation 3. The cut-off distance of vdW and electronic interactions was set to 1.2 nm, and the particle mesh Ewald (PME) method was employed to calculate long-range electrostatic interactions.

$$\sigma_{ij}=\frac{1}{2}\left(\sigma_{ii}+\sigma_{jj}\right);\varepsilon_{ij}=\left(\varepsilon_{ii}*\varepsilon_{jj}\right)^{1/2} \quad (3)$$

Letters of Copyright Permission

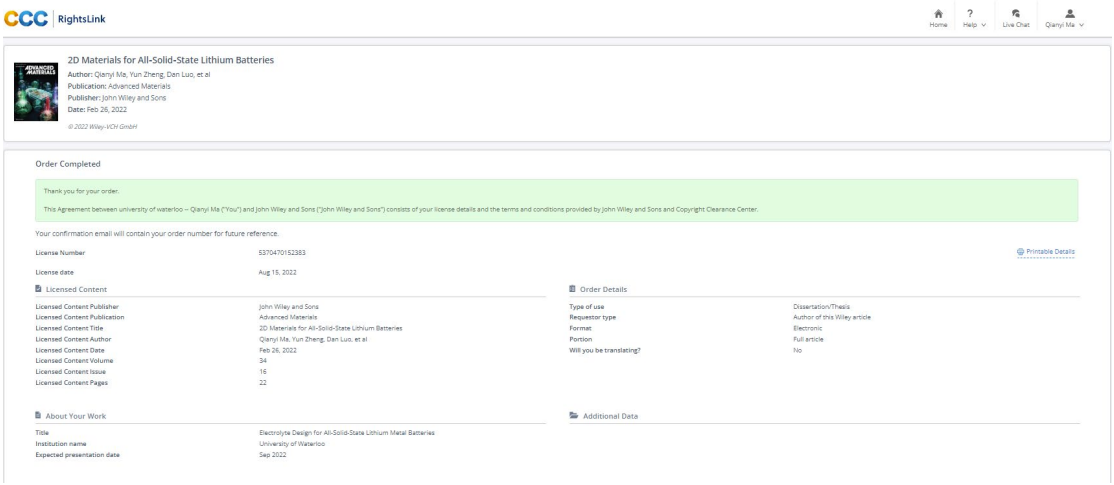

CCC | RightsLink

Home | Help | Live Chat | Qianyi Ma

2D Materials for All-Solid-State Lithium Batteries
Author: Qianyi Ma, Yun Zheng, Dan Luo, et al
Publication: Advanced Materials
Publisher: John Wiley and Sons
Date: Feb 26, 2022
© 2022 Wiley-VCH GmbH

Order Completed

Thank you for your order.

This Agreement between university of waterloo -- Qianyi Ma ("You") and John Wiley and Sons ("John Wiley and Sons") consists of your license details and the terms and conditions provided by John Wiley and Sons and Copyright Clearance Center.

Your confirmation email will contain your order number for future reference.

License Number	5370470152383
License date	Aug 15, 2022

Printable Details

Licensed Content

Licensed Content Publisher	John Wiley and Sons
Licensed Content Publication	Advanced Materials
Licensed Content Title	2D Materials for All-Solid-State Lithium Batteries
Licensed Content Author	Qianyi Ma, Yun Zheng, Dan Luo, et al
Licensed Content Date	Feb 26, 2022
Licensed Content Volume	34
Licensed Content Issue	16
Licensed Content Pages	22

Order Details

Type of use	Dissertation/Thesis
Requestor type	Author of this Wiley article
Format	Electronic
Portion	Full article
Will you be translating?	No

About Your Work

Title	Electrolyte Design for All-Solid-State Lithium Metal Batteries
Institution name	University of Waterloo
Expected presentation date	Sep 2022

Additional Data

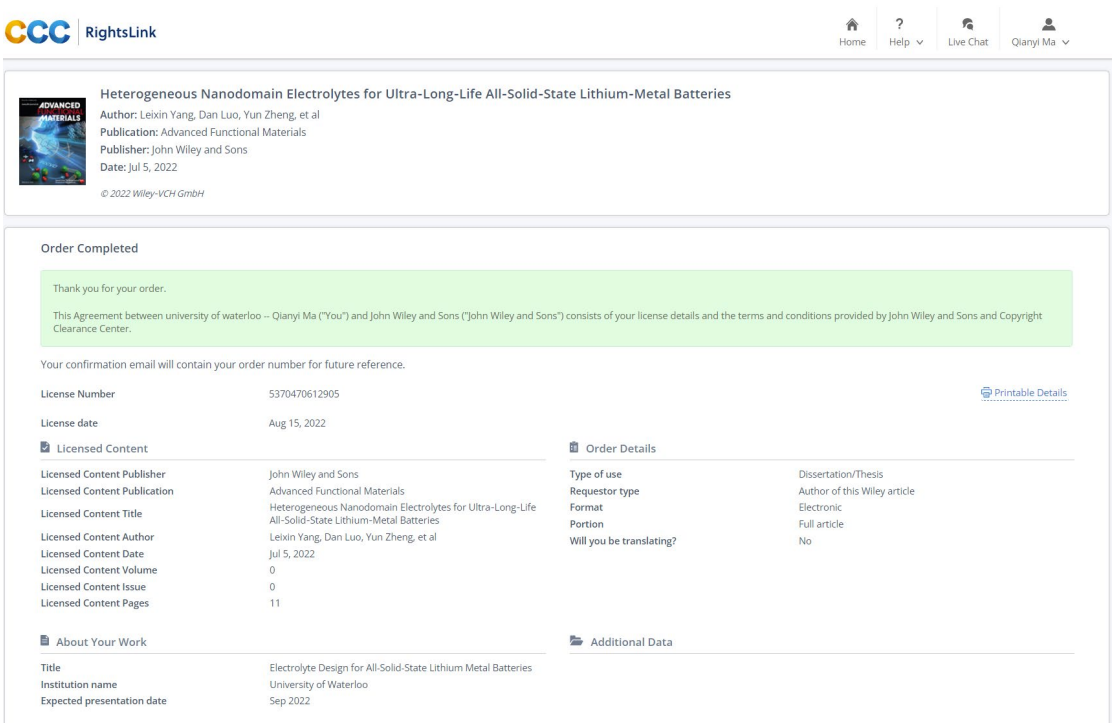

CCC | RightsLink

Home | Help | Live Chat | Qianyi Ma

Heterogeneous Nanodomain Electrolytes for Ultra-Long-Life All-Solid-State Lithium-Metal Batteries
Author: Leixin Yang, Dan Luo, Yun Zheng, et al
Publication: Advanced Functional Materials
Publisher: John Wiley and Sons
Date: Jul 5, 2022
© 2022 Wiley-VCH GmbH

Order Completed

Thank you for your order.

This Agreement between university of waterloo -- Qianyi Ma ("You") and John Wiley and Sons ("John Wiley and Sons") consists of your license details and the terms and conditions provided by John Wiley and Sons and Copyright Clearance Center.

Your confirmation email will contain your order number for future reference.

License Number	5370470612905
License date	Aug 15, 2022

Printable Details

Licensed Content

Licensed Content Publisher	John Wiley and Sons
Licensed Content Publication	Advanced Functional Materials
Licensed Content Title	Heterogeneous Nanodomain Electrolytes for Ultra-Long-Life All-Solid-State Lithium-Metal Batteries
Licensed Content Author	Leixin Yang, Dan Luo, Yun Zheng, et al
Licensed Content Date	Jul 5, 2022
Licensed Content Volume	0
Licensed Content Issue	0
Licensed Content Pages	11

Order Details

Type of use	Dissertation/Thesis
Requestor type	Author of this Wiley article
Format	Electronic
Portion	Full article
Will you be translating?	No

About Your Work

Title	Electrolyte Design for All-Solid-State Lithium Metal Batteries
Institution name	University of Waterloo
Expected presentation date	Sep 2022

Additional Data

References

1. Parellada, J.A., Dunn, M.M., Wayland, A., Cousins, J., and Shaw de Paredes, E. (1997). Patient tracking and follow-up after percutaneous breast biopsy. Appl. Radiol. *26*, 7–10.
2. Manthiram, A. (2011). Materials challenges and opportunities of lithium ion batteries. J. Phys. Chem. Lett. *2*, 176–184.
3. Manthiram, A., Fu, Y., and Su, Y.S. (2013). Challenges and prospects of lithium-sulfur batteries. Acc. Chem. Res. *46*, 1125–1134.
4. Wang, J., Yamada, Y., Sodeyama, K., Watanabe, E., Takada, K., Tateyama, Y., and Yamada, A. (2018). Fire-extinguishing organic electrolytes for safe batteries. Nat. Energy *3*, 22–29.
5. Sun, C., Liu, J., Gong, Y., Wilkinson, D.P., and Zhang, J. (2017). Recent advances in all-solid-state rechargeable lithium batteries. Nano Energy *33*, 363–386.
6. Li, M., Lu, J., Chen, Z., and Amine, K. (2018). 30 Years of Lithium-Ion Batteries. Adv. Mater. *30*, 1–24.
7. Hannan, M.A., Lipu, M.S.H., Hussain, A., and Mohamed, A. (2017). A review of lithium-ion battery state of charge estimation and management system in electric vehicle applications: Challenges and recommendations. Renew. Sustain. Energy Rev. *78*, 834–854.
8. Xu, R.C., Xia, X.H., Zhang, S.Z., Xie, D., Wang, X.L., and Tu, J.P. (2018). Interfacial challenges and progress for inorganic all-solid-state lithium batteries. Electrochim. Acta *284*, 177–187.

9. Chen, S., Xie, D., Liu, G., Mwizerwa, J.P., Zhang, Q., Zhao, Y., Xu, X., and Yao, X. (2018). Sulfide solid electrolytes for all-solid-state lithium batteries: Structure, conductivity, stability and application. Energy Storage Mater. *14*, 58–74.

10. Zhang, S.S. (2013). Liquid electrolyte lithium/sulfur battery: Fundamental chemistry, problems, and solutions. J. Power Sources *231*, 153–162.

11. Zheng, F., Kotobuki, M., Song, S., Lai, M.O., and Lu, L. (2018). Review on solid electrolytes for all-solid-state lithium-ion batteries. J. Power Sources *389*, 198–213.

12. Albertus, P., Babinec, S., Litzelman, S., and Newman, A. (2018). Status and challenges in enabling the lithium metal electrode for high-energy and low-cost rechargeable batteries. Nat. Energy *3*, 16–21.

13. Li, W., Yao, H., Yan, K., Zheng, G., Liang, Z., Chiang, Y.M., and Cui, Y. (2015). The synergetic effect of lithium polysulfide and lithium nitrate to prevent lithium dendrite growth. Nat. Commun. *6*.

14. Xu, G., Ding, B., Pan, J., Nie, P., Shen, L., and Zhang, X. (2014). High performance lithium-sulfur batteries: Advances and challenges. J. Mater. Chem. A *2*, 12662–12676.

15. Armand, M. (2001). Nature Lithium Battery. Nature *414*, 359–367.

16. Liu, Y., He, P., and Zhou, H. (2018). Rechargeable Solid-State Li–Air and Li–S Batteries: Materials, Construction, and Challenges. Adv. Energy Mater. *8*, 1–22.

17. Judez, X., Zhang, H., Li, C., Eshetu, G.G., González-Marcos, J.A., Armand, M., and Rodriguez-Martinez, L.M. (2018). Review—Solid Electrolytes for Safe and High Energy Density Lithium-Sulfur Batteries: Promises and Challenges. J.

Electrochem. Soc. *165*, A6008–A6016.

18. Xu, L., Tang, S., Cheng, Y., Wang, K., Liang, J., Liu, C., Cao, Y.C., Wei, F., and Mai, L. (2018). Interfaces in Solid-State Lithium Batteries. Joule *2*, 1991–2015.

19. Tao, H., Li, J., Ma, Q., Chen, Z., Zhang, X., Quan, Y., Yang, P., and Qi, C. (2020). Synthesis of W-Nb-O solid acid for catalytic combustion of low-concentration monochlorobenzene. Chem. Eng. J. *382*, 123045.

20. Varzi, A., Raccichini, R., Passerini, S., and Scrosati, B. (2016). Challenges and prospects of the role of solid electrolytes in the revitalization of lithium metal batteries. J. Mater. Chem. A *4*, 17251–17259.

21. Wan, J., Xie, J., Mackanic, D.G., Burke, W., Bao, Z., and Cui, Y. (2018). Status, promises, and challenges of nanocomposite solid-state electrolytes for safe and high performance lithium batteries. Mater. Today Nano *4*, 1–16.

22. Jiang, Z., Han, Q., Wang, S., and Wang, H. (2019). Reducing the Interfacial Resistance in All-Solid-State Lithium Batteries Based on Oxide Ceramic Electrolytes. ChemElectroChem *6*, 2970–2983.

23. Xia, S., Wu, X., Zhang, Z., Cui, Y., and Liu, W. (2019). Practical Challenges and Future Perspectives of All-Solid-State Lithium-Metal Batteries. Chem *5*, 753–785.

24. Gurung, A., Pokharel, J., Baniya, A., Pathak, R., Chen, K., Lamsal, B.S., Ghimire, N., Zhang, W.H., Zhou, Y., and Qiao, Q. (2019). A review on strategies addressing interface incompatibilities in inorganic all-solid-state lithium batteries. Sustain. Energy Fuels *3*, 3279–3309.

25. Ding, Z., Li, J., Li, J., and An, C. (2020). Review—Interfaces: Key Issue to Be Solved for All Solid-State Lithium Battery Technologies. J. Electrochem. Soc.

167, 070541.

26. Cui, G. (2020). Reasonable Design of High-Energy-Density Solid-State Lithium-Metal Batteries. Matter *2*, 805–815.

27. Kerman, K., Luntz, A., Viswanathan, V., Chiang, Y.-M., and Chen, Z. (2017). Review—Practical Challenges Hindering the Development of Solid State Li Ion Batteries. J. Electrochem. Soc. *164*, A1731–A1744.

28. Yu, C., Ganapathy, S., Eck, E.R.H.V., Wang, H., Basak, S., Li, Z., and Wagemaker, M. (2017). Accessing the bottleneck in all-solid state batteries, lithium-ion transport over the solid-electrolyte-electrode interface. Nat. Commun. *8*, 1–9.

29. Cheng, X.B., Zhao, C.Z., Yao, Y.X., Liu, H., and Zhang, Q. (2019). Recent Advances in Energy Chemistry between Solid-State Electrolyte and Safe Lithium-Metal Anodes. Chem *5*, 74–96.

30. Hu, Y., and Sun, X. (2014). Flexible rechargeable lithium ion batteries: Advances and challenges in materials and process technologies. J. Mater. Chem. A *2*, 10712–10738.

31. Jung, Y.S., Oh, D.Y., Nam, Y.J., and Park, K.H. (2015). Issues and challenges for bulk-type all-solid-state rechargeable lithium batteries using sulfide solid electrolytes. Isr. J. Chem. *55*, 472–485.

32. Gao, Z., Sun, H., Fu, L., Ye, F., Zhang, Y., Luo, W., and Huang, Y. (2018). Promises, Challenges, and Recent Progress of Inorganic Solid-State Electrolytes for All-Solid-State Lithium Batteries. Adv. Mater. *30*, 1–27.

33. Zhou, L., Kwok, C.Y., Shyamsunder, A., Zhang, Q., Wu, X., and Nazar, L.F. (2020). A new halospinel superionic conductor for high-voltage all solid state

lithium batteries. Energy Environ. Sci. *13*, 2056–2063.

34. Huo, C., Yan, Z., Song, X., and Zeng, H. (2015). 2D materials via liquid exfoliation: a review on fabrication and applications. Sci. Bull. *60*, 1994–2008.

35. Zhang, X., Hou, L., Ciesielski, A., and Samorì, P. (2016). 2D Materials Beyond Graphene for High-Performance Energy Storage Applications. Adv. Energy Mater. *6*.

36. Wang, X., Weng, Q., Yang, Y., Bando, Y., and Golberg, D. (2016). Hybrid two-dimensional materials in rechargeable battery applications and their microscopic mechanisms. Chem. Soc. Rev. *45*, 4042–4073.

37. Li, B., Xu, H., Ma, Y., and Yang, S. (2019). Harnessing the unique properties of 2D materials for advanced lithium-sulfur batteries. Nanoscale Horizons *4*, 77–98.

38. Mas-Ballesté, R., Gómez-Navarro, C., Gómez-Herrero, J., and Zamora, F. (2011). 2D materials: To graphene and beyond. Nanoscale *3*, 20–30.

39. Zhou, T., Lv, W., Li, J., Zhou, G., Zhao, Y., Fan, S., Liu, B., Li, B., Kang, F., and Yang, Q.H. (2017). Twinborn TiO2-TiN heterostructures enabling smooth trapping-diffusion-conversion of polysulfides towards ultralong life lithium-sulfur batteries. Energy Environ. Sci. *10*, 1694–1703.

40. Lu, P., Liu, L., Wang, S., Xu, J., Peng, J., Yan, W., Wang, Q., Li, H., Chen, L., and Wu, F. (2021). Superior All-Solid-State Batteries Enabled by a Gas-Phase-Synthesized Sulfide Electrolyte with Ultrahigh Moisture Stability and Ionic Conductivity. Adv. Mater. *33*, 1–13.

41. Shi, L., and Zhao, T. (2017). Recent advances in inorganic 2D materials and their applications in lithium and sodium batteries. J. Mater. Chem. A *5*, 3735–3758.

42. Dong, R., Zhang, T., and Feng, X. (2018). Interface-Assisted Synthesis of 2D

Materials: Trend and Challenges. Chem. Rev. *118*, 6189–6325.

43. Liu, D.H., Bai, Z., Li, M., Yu, A., Luo, D., Liu, W., Yang, L., Lu, J., Amine, K., and Chen, Z. (2020). Developing high safety Li-metal anodes for future high-energy Li-metal batteries: Strategies and perspectives. Chem. Soc. Rev. *49*, 5407–5445.

44. Luo, D., Zheng, L., Zhang, Z., Li, M., Chen, Z., Cui, R., Shen, Y., Li, G., Feng, R., Zhang, S., et al. (2021). Constructing multifunctional solid electrolyte interface via in-situ polymerization for dendrite-free and low N/P ratio lithium metal batteries. Nat. Commun. *12*, 1–11.

45. Zhao, F., Alahakoon, S.H., Adair, K., Zhang, S., Xia, W., Li, W., Yu, C., Feng, R., Hu, Y., Liang, J., et al. (2021). An Air-Stable and Li-Metal-Compatible Glass-Ceramic Electrolyte enabling High-Performance All-Solid-State Li Metal Batteries. Adv. Mater. *33*, 1–9.

46. Ren, B., Wen, G., Ricardez–Sandoval, L., and Croiset, E. (2021). New mechanistic insights into CO2 reduction in solid oxide electrolysis cell through a multi-scale modelling approach. J. Power Sources *490*, 229488.

47. Wen, G., Lee, D.U., Ren, B., Hassan, F.M., Jiang, G., Cano, Z.P., Gostick, J., Croiset, E., Bai, Z., Yang, L., et al. (2018). Orbital Interactions in Bi-Sn Bimetallic Electrocatalysts for Highly Selective Electrochemical CO2 Reduction toward Formate Production. Adv. Energy Mater. *8*, 1–9.

48. Wang, C., Hwang, S., Jiang, M., Liang, J., Sun, Y., Adair, K., Zheng, M., Mukherjee, S., Li, X., Li, R., et al. (2021). Deciphering Interfacial Chemical and Electrochemical Reactions of Sulfide-Based All-Solid-State Batteries. Adv. Energy Mater. *11*, 1–9.

49. Yang, P., Fan, S., Chen, Z., Bao, G., Zuo, S., and Qi, C. (2018). Synthesis of Nb2O5 based solid superacid materials for catalytic combustion of chlorinated VOCs. Appl. Catal. B Environ. *239*, 114–124.

50. Weiss, N.O., Zhou, H., Liao, L., Liu, Y., Jiang, S., Huang, Y., and Duan, X. (2012). Graphene: An emerging electronic material. Adv. Mater. *24*, 5782–5825.

51. Lerf, A., He, H., Forster, M., and Klinowski, J. (1998). Structure of graphite oxide revisited. J. Phys. Chem. B *102*, 4477–4482.

52. Dreyer, D.R., Murali, S., Zhu, Y., Ruoff, R.S., and Bielawski, C.W. (2011). Reduction of graphite oxide using alcohols. J. Mater. Chem. *21*, 3443–3447.

53. Kumbhakar, P., Chowde Gowda, C., Mahapatra, P.L., Mukherjee, M., Malviya, K.D., Chaker, M., Chandra, A., Lahiri, B., Ajayan, P.M., Jariwala, D., et al. (2021). Emerging 2D metal oxides and their applications. Mater. Today *45*, 142–168.

54. Li, R., Cheng, Y., and Huang, W. (2018). Recent Progress of Janus 2D Transition Metal Chalcogenides: From Theory to Experiments. Small *14*, 1–11.

55. Jiang, Q., Lei, Y., Liang, H., Xi, K., Xia, C., and Alshareef, H.N. (2020). Review of MXene electrochemical microsupercapacitors. Energy Storage Mater. *27*, 78–95.

56. Pakdel, A., Bando, Y., and Golberg, D. (2014). Nano boron nitride flatland. Chem. Soc. Rev. *43*, 934–959.

57. Yaghi, O.M. (2015). Chemistry of Covalent Organic Frameworks.

58. Thorarinsdottir, A.E., and Harris, T.D. (2020). Metal-Organic Framework Magnets. Chem. Rev. *120*, 8716–8789.

59. Wang, S., Yang, L., He, G., Shi, B., Li, Y., Wu, H., Zhang, R., Nunes, S., and

Jiang, Z. (2020). Two-dimensional nanochannel membranes for molecular and ionic separations. Chem. Soc. Rev. *49*, 1071–1089.

60. Kucinskis, G., Bajars, G., and Kleperis, J. (2013). Graphene in lithium ion battery cathode materials: A review. J. Power Sources *240*, 66–79.

61. Kim, H., Park, K.Y., Hong, J., and Kang, K. (2014). All-graphene-battery: Bridging the gap between supercapacitors and lithium ion batteries. Sci. Rep. *4*, 1–8.

62. Wu, S., Ge, R., Lu, M., Xu, R., and Zhang, Z. (2015). Graphene-based nano-materials for lithium-sulfur battery and sodium-ion battery. Nano Energy *15*, 379–405.

63. Geim, A.K. (2009). Graphene : Status and Prospects. *324*, 1530–1535.

64. Xu, R.C., Wang, X.L., Zhang, S.Z., Xia, Y., Xia, X.H., Wu, J.B., and Tu, J.P. (2018). Rational coating of Li7P3S11 solid electrolyte on MoS2 electrode for all-solid-state lithium ion batteries. J. Power Sources *374*, 107–112.

65. Wee, A.T.S. (2012). Graphene: The game changer? ACS Nano *6*, 5739–5741.

66. Wei, D., Haque, S., Andrew, P., Kivioja, J., Ryhänen, T., Pesquera, A., Centeno, A., Alonso, B., Chuvilin, A., and Zurutuza, A. (2013). Ultrathin rechargeable all-solid-state batteries based on monolayer graphene. J. Mater. Chem. A *1*, 3177–3181.

67. K. S. Novoselov, A. K. Geim, S. V. Morozov, D. Jiang, Y. Zhang, S. V. Dubonos, I.V.G. and A.A.F. (2016). Electric Field Effect in Atomically Thin Carbon Films. *306*, 666–669.

68. Mei, J., Liao, T., and Sun, Z. (2018). Two-dimensional metal oxide nanosheets for rechargeable batteries. J. Energy Chem. *27*, 117–127.

69. Augustyn, V., and Gogotsi, Y. (2017). 2D Materials with Nanoconfined Fluids for Electrochemical Energy Storage. Joule *1*, 443–452.

70. Augustyn, V. (2017). Tuning the interlayer of transition metal oxides for electrochemical energy storage. J. Mater. Res. *32*, 2–15.

71. Akinwande, D., Petrone, N., and Hone, J. (2014). Two-dimensional flexible nanoelectronics. Nat. Commun. *5*.

72. Mannhart, J. and S.D.G. (2010). Oxide Interfaces — An. Scien *327*, 1607–1611.

73. Mahmood, N., De Castro, I.A., Pramoda, K., Khoshmanesh, K., Bhargava, S.K., and Kalantar-Zadeh, K. (2019). Atomically thin two-dimensional metal oxide nanosheets and their heterostructures for energy storage. Energy Storage Mater. *16*, 455–480.

74. Zhang, K., Park, M., Zhou, L., Lee, G.H., Li, W., Kang, Y.M., and Chen, J. (2016). Urchin-Like CoSe2 as a High-Performance Anode Material for Sodium-Ion Batteries. Adv. Funct. Mater. *26*, 6728–6735.

75. Yuan, H., Kong, L., Li, T., and Zhang, Q. (2017). A review of transition metal chalcogenide/graphene nanocomposites for energy storage and conversion. Chinese Chem. Lett. *28*, 2180–2194.

76. Chen, X., Peng, H.J., Zhang, R., Hou, T.Z., Huang, J.Q., Li, B., and Zhang, Q. (2017). An analogous periodic law for strong anchoring of polysulfides on polar hosts in lithium sulfur batteries: S- or Li-binding on first-row transition-metal sulfides? ACS Energy Lett. *2*, 795–801.

77. Murphy, D.W., and Trumbore, F.A. (1977). Metal chalcogenides as reversible electrodes in nonaqueous lithium batteries. J. Cryst. Growth *39*, 185–199.

78. Huang, X., Zeng, Z., and Zhang, H. (2013). Metal dichalcogenide nanosheets:

Preparation, properties and applications. Chem. Soc. Rev. *42*, 1934–1946.

79. Xu, X., Liu, W., Kim, Y., and Cho, J. (2014). Nanostructured transition metal sulfides for lithium ion batteries: Progress and challenges. Nano Today *9*, 604–630.

80. Qiu, W., Yang, N., Luo, D., Wang, J., Zheng, L., Zhu, Y., Akinoglu, E.M., Huang, Q., Shui, L., Wang, R., et al. (2021). Precise synthesis of Fe–N2 with N vacancies coordination for boosting electrochemical artificial N2 fixation. Appl. Catal. B Environ. *293*, 120216.

81. Liu, Z., Gong, Y., Zhou, W., Ma, L., Yu, J., Idrobo, J.C., Jung, J., Macdonald, A.H., Vajtai, R., Lou, J., et al. (2013). Ultrathin higherature oxidation-resistant coatings of hexagonal boron nitride. Nat. Commun. *4*, 1–8.

82. Duan, Z.Q., Liu, Y.T., Xie, X.M., Ye, X.Y., and Zhu, X.D. (2016). H-BN Nanosheets as 2D Substrates to Load 0D Fe3O4 Nanoparticles: A Hybrid Anode Material for Lithium-Ion Batteries. Chem. - An Asian J. *11*, 828–833.

83. Nanosheets, N., Li, L.H., Cervenka, J., Watanabe, K., Taniguchi, T., and Chen, Y. (2014). Strong Oxidation Resistance of Atomically Thin Boron. 1457–1462.

84. Xie, J., Liao, L., Gong, Y., Li, Y., Shi, F., Pei, A., Sun, J., Zhang, R., Kong, B., Subbaraman, R., et al. (2017). Stitching h-BN by atomic layer deposition of LiF as a stable interface for lithium metal anode. Sci. Adv. *3*, 1–10.

85. Guerra, V., Wan, C., and McNally, T. (2019). Thermal conductivity of 2D nano-structured boron nitride (BN) and its composites with polymers. Prog. Mater. Sci. *100*, 170–186.

86. Dean, C.R., Young, A.F., Meric, I., Lee, C., Wang, L., Sorgenfrei, S., Watanabe, K., Taniguchi, T., Kim, P., Shepard, K.L., et al. (2010). Boron nitride substrates

for high-quality graphene electronics. Nat. Nanotechnol. *5*, 722–726.

87. Decker, R., Wang, Y., Brar, V.W., Regan, W., Tsai, H.Z., Wu, Q., Gannett, W., Zettl, A., and Crommie, M.F. (2011). Local electronic properties of graphene on a BN substrate via scanning tunneling microscopy. Nano Lett. *11*, 2291–2295.

88. Xue, J., Sanchez-Yamagishi, J., Bulmash, D., Jacquod, P., Deshpande, A., Watanabe, K., Taniguchi, T., Jarillo-Herrero, P., and Leroy, B.J. (2011). Scanning tunnelling microscopy and spectroscopy of ultra-flat graphene on hexagonal boron nitride. Nat. Mater. *10*, 282–285.

89. Dou, H., Jiang, B., Xu, M., Zhang, Z., Wen, G., Peng, F., Yu, A., Bai, Z., Sun, Y., Zhang, L., et al. (2019). Boron Nitride Membranes with a Distinct Nanoconfinement Effect for Efficient Ethylene/Ethane Separation. Angew. Chemie *131*, 14107–14113.

90. Zhao, C., Diercks, C.S., Zhu, C., Hanikel, N., Pei, X., and Yaghi, O.M. (2018). Urea-Linked Covalent Organic Frameworks. J. Am. Chem. Soc. *140*, 16438–16441.

91. Martínez-Abadiá, M., Stoppiello, C.T., Strutynski, K., Lerma-Berlanga, B., Martí-Gastaldo, C., Saeki, A., Melle-Franco, M., Khlobystov, A.N., and Mateo-Alonso, A. (2019). A Wavy Two-Dimensional Covalent Organic Framework from Core-Twisted Polycyclic Aromatic Hydrocarbons. J. Am. Chem. Soc. *141*, 14403–14410.

92. Alahakoon, S.B., Diwakara, S.D., Thompson, C.M., and Smaldone, R.A. (2020). Supramolecular design in 2D covalent organic frameworks. Chem. Soc. Rev. *49*, 1344–1356.

93. Liu, J., Lyu, P., Zhang, Y., Nachtigall, P., and Xu, Y. (2018). New Layered

Triazine Framework/Exfoliated 2D Polymer with Superior Sodium-Storage Properties. Adv. Mater. *30*, 1–8.

94. Yang, L., Yang, H., Wu, H., Zhang, L., Ma, H., Liu, Y., Wu, Y., Ren, Y., Wu, X., and Jiang, Z. (2021). COF membranes with uniform and exchangeable facilitated transport carriers for efficient carbon capture. J. Mater. Chem. A *9*, 12636–12643.

95. Zheng, W., Tsang, C.S., Lee, L.Y.S., and Wong, K.Y. (2019). Two-dimensional metal-organic framework and covalent-organic framework: synthesis and their energy-related applications. Mater. Today Chem. *12*, 34–60.

96. Park, J., Lee, M., Feng, D., Huang, Z., Hinckley, A.C., Yakovenko, A., Zou, X., Cui, Y., and Bao, Z. (2018). Stabilization of Hexaaminobenzene in a 2D Conductive Metal-Organic Framework for High Power Sodium Storage. J. Am. Chem. Soc. *140*, 10315–10323.

97. Aubrey, M.L., and Long, J.R. (2015). A Dual-Ion Battery Cathode via Oxidative Insertion of Anions in a Metal-Organic Framework. J. Am. Chem. Soc. *137*, 13594–13602.

98. Sheberla, D., Bachman, J.C., Elias, J.S., Sun, C.J., Shao-Horn, Y., and Dincă, M. (2017). Conductive MOF electrodes for stable supercapacitors with high areal capacitance. Nat. Mater. *16*, 220–224.

99. Qiu, W., Xie, X.Y., Qiu, J., Fang, W.H., Liang, R., Ren, X., Ji, X., Cui, G., Asiri, A.M., Cui, G., et al. (2018). High-performance artificial nitrogen fixation at ambient conditions using a metal-free electrocatalyst. Nat. Commun. *9*, 1–8.

100. Lin, Z., McCreary, A., Briggs, N., Subramanian, S., Zhang, K., Sun, Y., Li, X., Borys, N.J., Yuan, H., Fullerton-Shirey, S.K., et al. (2016). 2D materials

advances: From large scale synthesis and controlled heterostructures to improved characterization techniques, defects and applications. 2D Mater. *3*.

101. Briggs, N., Bersch, B., Wang, Y., Jiang, J., Koch, R.J., Nayir, N., Wang, K., Kolmer, M., Ko, W., La, A. De, et al. (2020). By Confinement Heteroepitaxy. Nat. Mater.

102. Huo, C., Yan, Z., Song, X., and Zeng, H. (2015). 2D materials via liquid exfoliation: a review on fabrication and applications. Sci. Bull. *60*, 1994–2008.

103. Gao, E., Lin, S.Z., Qin, Z., Buehler, M.J., Feng, X.Q., and Xu, Z. (2018). Mechanical exfoliation of two-dimensional materials. J. Mech. Phys. Solids *115*, 248–262.

104. Nicolosi, V., Chhowalla, M., Kanatzidis, M.G., Strano, M.S., and Coleman, J.N. (2013). Liquid exfoliation of layered materials. Science (80-.). *340*, 72–75.

105. Lu, J., Chen, Z., Pan, F., Curtiss, L.A., and Amine, K. (2010). Charge matters in fish. Nat. Nanotechnol. *11*.

106. Gao, E., and Xu, Z. (2015). Thin-Shell Thickness of Two-Dimensional Materials. J. Appl. Mech. Trans. ASME *82*, 1–4.

107. Cai, X., Luo, Y., Liu, B., and Cheng, H.M. (2018). Preparation of 2D material dispersions and their applications. Chem. Soc. Rev. *47*, 6224–6266.

108. Moon, J.Y., Kim, M., Kim, S. Il, Xu, S., Choi, J.H., Whang, D., Watanabe, K., Taniguchi, T., Park, D.S., Seo, J., et al. (2020). Layer-engineered large-area exfoliation of graphene. Sci. Adv. *6*, 1–8.

109. Coleman, J.N., Lotya, M., O'Neill, A., Bergin, S.D., King, P.J., Khan, U., Young, K., Gaucher, A., De, S., Smith, R.J., et al. (2011). Two-dimensional nanosheets produced by liquid exfoliation of layered materials. Science (80-.).

331, 568–571.

110. Chen, H., Feng, X., Huang, Y., Huang, Y., and Rogers, J.A. (2013). Experiments and viscoelastic analysis of peel test with patterned strips for applications to transfer printing. J. Mech. Phys. Solids *61*, 1737–1752.

111. Chen, H., and Chen, S. (2013). The peeling behaviour of a graphene sheet on a nano-scale corrugated surface. J. Phys. D. Appl. Phys. *46*.

112. Yu, J., Li, J., Zhang, W., and Chang, H. (2015). Synthesis of high quality two-dimensional materials via chemical vapor deposition. Chem. Sci. *6*, 6705–6716.

113. Gao, T., Xie, S., Gao, Y., Liu, M., Chen, Y., Zhang, Y., and Liu, Z. (2011). Growth and atomic-scale characterizations of graphene on multifaceted textured Pt foils prepared by chemical vapor deposition. ACS Nano *5*, 9194–9201.

114. Yan, K., Peng, H., Zhou, Y., Li, H., and Liu, Z. (2011). Formation of bilayer bernal graphene: Layer-by-layer epitaxy via chemical vapor deposition. Nano Lett. *11*, 1106–1110.

115. Wang, M., Jang, S.K., Jang, W.J., Kim, M., Park, S.Y., Kim, S.W., Kahng, S.J., Choi, J.Y., Ruoff, R.S., Song, Y.J., et al. (2013). A platform for large-scale graphene electronics - CVD growth of single-layer graphene on CVD-grown hexagonal boron nitride. Adv. Mater. *25*, 2746–2752.

116. Seah, C.M., Chai, S.P., and Mohamed, A.R. (2014). Mechanisms of graphene growth by chemical vapour deposition on transition metals. Carbon N. Y. *70*, 1–21.

117. Li, L., Yu, Y., Ye, G.J., Ge, Q., Ou, X., Wu, H., Feng, D., Chen, X.H., and Zhang, Y. (2014). Black phosphorus field-effect transistors. Nat. Nanotechnol. *9*, 372–377.

118. Bourlinos, A.B., Georgakilas, V., Zboril, R., Sterioti, T.A., and Stubos, A.K. (2009). Liquid-Phase Exfoliation of Graphite Towards Solubilized Graphenes. Small *5*, 1841–1845.

119. Yu, Y., Li, C., Liu, Y., Su, L., Zhang, Y., and Cao, L. (2013). Controlled scalable synthesis of uniform, high-quality monolayer and few-layer MoS2 films. Sci. Rep. *3*, 1–6.

120. Witomska, S., Leydecker, T., Ciesielski, A., and Samorì, P. (2019). Production and Patterning of Liquid Phase–Exfoliated 2D Sheets for Applications in Optoelectronics. Adv. Funct. Mater. *29*.

121. Park, G.H., Nielsch, K., and Thomas, A. (2019). 2D Transition Metal Dichalcogenide Thin Films Obtained by Chemical Gas Phase Deposition Techniques. Adv. Mater. Interfaces *6*, 1–31.

122. Zhang, Y., Zuo, T., Popovic, J., Lim, K., and Yin, Y. (2020). Towards better Li metal anodes : Challenges and strategies. Mater. Today *33*, 56–74.

123. Wang, Y., Liu, B., Li, Q., Cartmell, S., Ferrara, S., Deng, Z.D., and Xiao, J. (2015). Lithium and lithium ion batteries for applications in microelectronic devices: A review. J. Power Sources *286*, 330–345.

124. Lin, J., Wu, Y., Bi, R., and Guo, H. (2017). All-solid-state microscale lithium-ion battery fabricated by a simple process with graphene as anode. Sensors Actuators, A Phys. *253*, 218–222.

125. Huang, S., Yang, H., Hu, J., Liu, Y., Wang, K., Peng, H., Zhang, H., and Fan, L.Z. (2019). Early Lithium Plating Behavior in Confined Nanospace of 3D Lithiophilic Carbon Matrix for Stable Solid-State Lithium Metal Batteries. Small *15*, 32–34.

126. Wen, J., Huang, Y., Duan, J., Wu, Y., Luo, W., Zhou, L., Hu, C., Huang, L., Zheng, X., Yang, W., et al. (2019). Highly Adhesive Li-BN Nanosheet Composite Anode with Excellent Interfacial Compatibility for Solid-State Li Metal Batteries. ACS Nano *13*, 14549–14556.

127. Cheng, Q., Li, A., Li, N., Li, S., Zangiabadi, A., Li, T. De, Huang, W., Li, A.C., Jin, T., Song, Q., et al. (2019). Stabilizing Solid Electrolyte-Anode Interface in Li-Metal Batteries by Boron Nitride-Based Nanocomposite Coating. Joule *3*, 1510–1522.

128. Kızılaslan, A., Çetinkaya, T., and Akbulut, H. (2020). 2H-MoS2 as an Artificial Solid Electrolyte Interface in All-Solid-State Lithium–Sulfur Batteries. Adv. Mater. Interfaces *7*, 1–7.

129. Xue, Y., Ma, G., Wang, X., Jin, M., Akinoglu, E.M., Luo, D., and Shui, L. (2021). Constructing multifunctional solid electrolyte interface via in-situ polymerization for dendrite-free and low N/P ratio lithium metal batteries. ACS Appl. Mater. Interfaces *13*, 7334–7342.

130. Lou, S., Zhang, F., Fu, C., Chen, M., Ma, Y., Yin, G., and Wang, J. (2020). Interface Issues and Challenges in All-Solid-State Batteries: Lithium, Sodium, and Beyond. Adv. Mater. *2000721*, 1–29.

131. Li, Y., Li, Y., Yang, Y., Cui, Z., Wang, J., and Zhang, T. (2020). Conversion inorganic interlayer of a LiF/graphene composite in all-solid-state lithium batteries. Chem. Commun. *56*, 1725–1728.

132. Cai, L., Wan, H., Zhang, Q., Mwizerwa, J.P., Xu, X., and Yao, X. (2020). In Situ Coating of Li7P3S11Electrolyte on CuCo2S4/Graphene Nanocomposite as a High-Performance Cathode for All-Solid-State Lithium Batteries. ACS Appl.

Mater. Interfaces *12*, 33810–33816.

133. Wan, H., Cai, L., Han, F., Mwizerwa, J.P., Wang, C., and Yao, X. (2019). Construction of 3D Electronic/Ionic Conduction Networks for All-Solid-State Lithium Batteries. Small *15*, 1–7.

134. Wan, H., Peng, G., Yao, X., Yang, J., Cui, P., and Xu, X. (2016). Cu2ZnSnS4/graphene nanocomposites for ultrafast, long life all-solid-state lithium batteries using lithium metal anode. Energy Storage Mater. *4*, 59–65.

135. Zhang, C., Lin, Y., Zhu, Y., Zhang, Z., and Liu, J. (2017). Improved lithium-ion and electrically conductive sulfur cathode for all-solid-state lithium-sulfur batteries. RSC Adv. *7*, 19231–19236.

136. Zhuang, Z., Yang, L., Ju, B., Yin, A., Lei, G., Zhou, Q., Tang, Y., Deng, Z., Tu, F., and Qin, S. (2020). Engineering LiNi 0.5 Co 0.2 Mn 0.3 O 2 /poly(propylene carbonate) interface by graphene oxide modification for all-solid-state lithium batteries . Energy Storage *2*, 1–12.

137. Cao, R., Xu, W., Lv, D., Xiao, J., and Zhang, J.G. (2015). Anodes for Rechargeable Lithium-Sulfur Batteries. Adv. Energy Mater. *5*.

138. Yao, X., Huang, N., Han, F., Zhang, Q., Wan, H., Mwizerwa, J.P., Wang, C., and Xu, X. (2017). High-Performance All-Solid-State Lithium–Sulfur Batteries Enabled by Amorphous Sulfur-Coated Reduced Graphene Oxide Cathodes. Adv. Energy Mater. *7*, 1–9.

139. Zhang, Y., Lai, J., Gong, Y., Hu, Y., Liu, J., Sun, C., and Wang, Z.L. (2016). A Safe High-Performance All-Solid-State Lithium-Vanadium Battery with a Freestanding V2O5 Nanowire Composite Paper Cathode. ACS Appl. Mater. Interfaces *8*, 34309–34316.

140. Zhang, Q., Wan, H., Liu, G., Ding, Z., Mwizerwa, J.P., and Yao, X. (2019). Rational design of multi-channel continuous electronic/ionic conductive networks for room temperature vanadium tetrasulfide-based all-solid-state lithium-sulfur batteries. Nano Energy *57*, 771–782.

141. Zhang, Q., Ding, Z., Liu, G., Wan, H., Mwizerwa, J.P., Wu, J., and Yao, X. (2019). Molybdenum trisulfide based anionic redox driven chemistry enabling high-performance all-solid-state lithium metal batteries. Energy Storage Mater. *23*, 168–180.

142. Xu, R.C., Xia, X.H., Wang, X.L., Xia, Y., and Tu, J.P. (2017). Tailored Li2S-P2S5 glass-ceramic electrolyte by MoS2 doping, possessing high ionic conductivity for all-solid-state lithium-sulfur batteries. J. Mater. Chem. A *5*, 2829–2834.

143. Santhosha, A.L., Nayak, P.K., Pollok, K., Langenhorst, F., and Adelhelm, P. (2019). Exfoliated MoS2 as Electrode for All-Solid-State Rechargeable Lithium-Ion Batteries. J. Phys. Chem. C *123*, 12126–12134.

144. Zhang, Q., Yao, X., Mwizerwa, J.P., Huang, N., Wan, H., Huang, Z., and Xu, X. (2018). FeS nanosheets as positive electrodes for all-solid-state lithium batteries. Solid State Ionics *318*, 60–64.

145. Xing, C., Zhang, D., Cao, K., Zhao, S., Wang, X., Qin, H., Liu, J., Jiang, Y., and Meng, L. (2015). In situ growth of FeS microsheet networks with enhanced electrochemical performance for lithium-ion batteries. J. Mater. Chem. A *3*, 8742–8749.

146. Kamaya, N., Homma, K., Yamakawa, Y., Hirayama, M., Kanno, R., Yonemura, M., Kamiyama, T., Kato, Y., Hama, S., Kawamoto, K., et al. (2011). A lithium

superionic conductor. Nat. Mater. *10*, 682–686.

147. Cai, L., Zhang, Q., Mwizerwa, J.P., Wan, H., Yang, X., Xu, X., and Yao, X. (2018). Highly Crystalline Layered VS2 Nanosheets for All-Solid-State Lithium Batteries with Enhanced Electrochemical Performances. ACS Appl. Mater. Interfaces *10*, 10053–10063.

148. Fang, W., Zhao, H., Xie, Y., Fang, J., Xu, J., and Chen, Z. (2015). Facile Hydrothermal Synthesis of VS2/Graphene Nanocomposites with Superior High-Rate Capability as Lithium-Ion Battery Cathodes. ACS Appl. Mater. Interfaces *7*, 13044–13052.

149. Xu, S., Kwok, C.Y., Zhou, L., Zhang, Z., Kochetkov, I., and Nazar, L.F. (2020). A High Capacity All Solid-State Li-Sulfur Battery Enabled by Conversion-Intercalation Hybrid Cathode Architecture. Adv. Funct. Mater. *2004239*, 1–8.

150. Fujii, Y., Ramirez, D., Rosero-Navarro, N.C., Jullian, D., Miura, A., Jaramillo, F., and Tadanaga, K. (2019). Two-Dimensional Hybrid Halide Perovskite as Electrode Materials for All-Solid-State Lithium Secondary Batteries Based on Sulfide Solid Electrolytes. ACS Appl. Energy Mater. *2*, 6569–6576.

151. Shi, J., Liu, G., Weng, W., Cai, L., Zhang, Q., Wu, J., Xu, X., and Yao, X. (2020). Co3S4@Li7P3S11 Hexagonal Platelets as Cathodes with Superior Interfacial Contact for All-Solid-State Lithium Batteries. ACS Appl. Mater. Interfaces *12*, 14079–14086.

152. Xia, Q., Zhang, Q., Sun, S., Hussain, F., Zhang, C., Zhu, X., Meng, F., Liu, K., Geng, H., Xu, J., et al. (2020). Tunnel Intergrowth LixMnO2 Nanosheet Arrays as 3D Cathode for High-Performance All-Solid-State Thin Film Lithium Microbatteries. Adv. Mater. *2003524*, 1–11.

153. Su, L., Liu, L., Hei, J., Chen, H., Wang, L., Wang, Y., and Ren, M. (2020). Sub-10 nm V2O5 Crystals on Carbon Nanosheets for Advanced All-Solid-State Lithium Metal Batteries. Part. Part. Syst. Charact. *37*, 1–8.

154. Zhang, Q., Mwizerwa, J.P., Wan, H., Cai, L., Xu, X., and Yao, X. (2017). Fe3S4@Li7P3S11 nanocomposites as cathode materials for all-solid-state lithium batteries with improved energy density and low cost. J. Mater. Chem. A *5*, 23919–23925.

155. Dou, H., Xu, M., Wang, B., Zhang, Z., Wen, G., Zheng, Y., Luo, D., Zhao, L., Yu, A., Zhang, L., et al. (2021). Microporous framework membranes for precise molecule/ion separations. Chem. Soc. Rev. *50*, 986–1029.

156. Han, Q., Wang, S., Jiang, Z., Hu, X., and Wang, H. (2020). Composite Polymer Electrolyte Incorporating Metal-Organic Framework Nanosheets with Improved Electrochemical Stability for All-Solid-State Li Metal Batteries. ACS Appl. Mater. Interfaces *12*, 20514–20521.

157. Zhai, P., Peng, N., Sun, Z., Wu, W., Kou, W., Cui, G., Zhao, K., and Wang, J. (2020). Thin laminar composite solid electrolyte with high ionic conductivity and mechanical strength towards advanced all-solid-state lithium-sulfur battery. J. Mater. Chem. A *8*, 23344–23353.

158. Wang, B., Tang, M., Wu, Y., Chen, Y., Jiang, C., Zhuo, S., Zhu, S., and Wang, C. (2019). A 2D Layered Natural Ore as a Novel Solid-State Electrolyte. ACS Appl. Energy Mater. *2*, 5909–5916.

159. Li, Y., Sun, Z., Liu, D., Gao, Y., Wang, Y., Bu, H., Li, M., Zhang, Y., Gao, G., and Ding, S. (2020). A composite solid polymer electrolyte incorporating MnO2 nanosheets with reinforced mechanical properties and electrochemical stability

for lithium metal batteries. J. Mater. Chem. A *8*, 2021–2032.

160. Gomari, S., Esfandeh, M., and Ghasemi, I. (2017). All-solid-state flexible nanocomposite polymer electrolytes based on poly(ethylene oxide): Lithium perchlorate using functionalized graphene. Solid State Ionics *303*, 37–46.

161. Dey, A., Karan, S., and De, S.K. (2010). Molecular interaction and ionic conductivity of polyethylene oxide-LiClO4 nanocomposites. J. Phys. Chem. Solids *71*, 329–335.

162. Zhang, Z., Antonio, R.G., and Choy, K.L. (2019). Boron nitride enhanced polymer/salt hybrid electrolytes for all-solid-state lithium ion batteries. J. Power Sources *435*, 226736.

163. Yin, X., Wang, L., Kim, Y., Ding, N., Kong, J., Safanama, D., Zheng, Y., Xu, J., Repaka, D.V.M., Hippalgaonkar, K., et al. (2020). Thermal Conductive 2D Boron Nitride for High-Performance All-Solid-State Lithium–Sulfur Batteries. Adv. Sci. *7*, 1–7.

164. Tang, W., Tang, S., Zhang, C., Ma, Q., Xiang, Q., Yang, Y.W., and Luo, J. (2018). Simultaneously Enhancing the Thermal Stability, Mechanical Modulus, and Electrochemical Performance of Solid Polymer Electrolytes by Incorporating 2D Sheets. Adv. Energy Mater. *8*, 1–7.

165. Tang, W., Tang, S., Guan, X., Zhang, X., Xiang, Q., and Luo, J. (2019). High-Performance Solid Polymer Electrolytes Filled with Vertically Aligned 2D Materials. Adv. Funct. Mater. *29*, 1–7.

166. Zheng, G., Lee, S.W., Liang, Z., Lee, H.W., Yan, K., Yao, H., Wang, H., Li, W., Chu, S., and Cui, Y. (2014). Interconnected hollow carbon nanospheres for stable lithium metal anodes. Nat. Nanotechnol. *9*, 618–623.

167. Yang, L.-Y., Wei, D.-X., Xu, M., Yao, Y.-F., and Chen, Q. (2014). Transferring Lithium Ions in Nanochannels: A PEO/Li + Solid Polymer Electrolyte Design . Angew. Chemie *126*, 3705–3709.

168. Chen, X., Chen, X.R., Hou, T.Z., Li, B.Q., Cheng, X.B., Zhang, R., and Zhang, Q. (2019). Lithiophilicity chemistry of heteroatom-doped carbon to guide uniform lithium nucleation in lithium metal anodes. Sci. Adv. *5*.

169. Li, Y., Zhang, L., Sun, Z., Gao, G., Lu, S., Zhu, M., Zhang, Y., Jia, Z., Xiao, C., Bu, H., et al. (2020). Hexagonal boron nitride induces anion trapping in a polyethylene oxide based solid polymer electrolyte for lithium dendrite inhibition. J. Mater. Chem. A *8*, 9579–9589.

170. Sun, Z., Li, Y., Zhang, S., Shi, L., Wu, H., Bu, H., and Ding, S. (2019). G-C3N4 nanosheets enhanced solid polymer electrolytes with excellent electrochemical performance, mechanical properties, and thermal stability. J. Mater. Chem. A *7*, 11069–11076.

171. Jia, W., Li, Z., Wu, Z., Wang, L., Wu, B., Wang, Y., Cao, Y., and Li, J. (2018). Graphene oxide as a filler to improve the performance of PAN-LiClO4 flexible solid polymer electrolyte. Solid State Ionics *315*, 7–13.

172. Xu, X., Wang, L., Fei, H., and Ci, L. (2019). Boron nitride doped Li7P3S11 solid electrolyte with improved interfacial compatibility and application in all-solid-state Li/S battery. J. Mater. Sci. Mater. Electron. *30*, 19119–19125.

173. Geng, P., Zheng, S., Tang, H., Zhu, R., Zhang, L., Cao, S., Xue, H., and Pang, H. (2018). Transition Metal Sulfides Based on Graphene for Electrochemical Energy Storage. Adv. Energy Mater. *8*, 1–26.

174. Oh, D.Y., Choi, Y.E., Kim, D.H., Lee, Y.G., Kim, B.S., Park, J., Sohn, H., and

Jung, Y.S. (2016). All-solid-state lithium-ion batteries with TiS2 nanosheets and sulphide solid electrolytes. J. Mater. Chem. A *4*, 10329–10335.

175. Wu, J., Li, X., Zhao, Y., Liu, L., Qu, W., Luo, R., Chen, R., Li, Y., and Chen, Q. (2018). Interface engineering in solid state Li metal batteries by quasi-2D hybrid perovskites. J. Mater. Chem. A *6*, 20896–20903.

176. Li, Z., Liu, Z.W., Li, Z., Wang, T.X., Zhao, F., Ding, X., Feng, W., and Han, B.H. (2020). Defective 2D Covalent Organic Frameworks for Postfunctionalization. Adv. Funct. Mater. *30*, 1–9.

177. Li, Z., Liu, Z.W., Mu, Z.J., Cao, C., Li, Z., Wang, T.X., Li, Y., Ding, X., Han, B.H., and Feng, W. (2020). Cationic covalent organic framework based all-solid-state electrolytes. Mater. Chem. Front. *4*, 1164–1173.

178. Zhang, G., Hong, Y.L., Nishiyama, Y., Bai, S., Kitagawa, S., and Horike, S. (2019). Accumulation of Glassy Poly(ethylene oxide) Anchored in a Covalent Organic Framework as a Solid-State Li + Electrolyte. J. Am. Chem. Soc. *141*, 1227–1234.

179. Li, X., Hou, Q., Huang, W., Xu, H. Sen, Wang, X., Yu, W., Li, R., Zhang, K., Wang, L., Chen, Z., et al. (2020). Solution-Processable Covalent Organic Framework Electrolytes for All-Solid-State Li-Organic Batteries. ACS Energy Lett., 3498–3506.

180. Sun, W., Zhang, J., Xie, M., Lu, D., Zhao, Z., Li, Y., Cheng, Z., Zhang, S., and Chen, H. (2020). Ultrathin Aramid/COF Heterolayered Membrane for Solid-State Li-Metal Batteries. Nano Lett.

181. Cheng, Y., Zhang, L., Zhang, Q., Li, J., Tang, Y., Delmas, C., Zhu, T., Winter, M., Wang, M.S., and Huang, J. (2021). Understanding all solid-state lithium

batteries through in situ transmission electron microscopy. Mater. Today *42*, 137–161.

182. Xiang, Y., Zheng, G., Liang, Z., Jin, Y., Liu, X., Chen, S., Zhou, K., Zhu, J., Lin, M., He, H., et al. (2020). Visualizing the growth process of sodium microstructures in sodium batteries by in-situ 23Na MRI and NMR spectroscopy. Nat. Nanotechnol. *15*, 883–890.

183. Minafra, N., Culver, S.P., Li, C., Senyshyn, A., and Zeier, W.G. (2019). Influence of the Lithium Substructure on the Diffusion Pathways and Transport Properties of the Thio-LISICON Li4Ge1- xSnxS4. Chem. Mater. *31*, 3794–3802.

184. Seidlhofer, B.K., Jerliu, B., Trapp, M., Hüger, E., Risse, S., Cubitt, R., Schmidt, H., Steitz, R., and Ballauff, M. (2016). Lithiation of Crystalline Silicon As Analyzed by Operando Neutron Reflectivity. ACS Nano *10*, 7458–7466.

185. Robinson, I., and Harder, R. (2009). Coherent X-ray diffraction imaging of strain at the nanoscale. Nat. Mater. *8*, 291–298.

186. Deng, Y., Eames, C., Chotard, J.N., Laleìre, F., Seznec, V., Emge, S., Pecher, O., Grey, C.P., Masquelier, C., and Islam, M.S. (2015). Structural and Mechanistic Insights into Fast Lithium-Ion Conduction in Li4SiO4-Li3PO4 Solid Electrolytes. J. Am. Chem. Soc. *137*, 9136–9145.

187. Kun, R., Langer, F., Delle Piane, M., Ohno, S., Zeier, W.G., Gockeln, M., Colombi Ciacchi, L., Busse, M., and Fekete, I. (2018). Structural and Computational Assessment of the Influence of Wet-Chemical Post-Processing of the Al-Substituted Cubic Li7La3Zr2O12. ACS Appl. Mater. Interfaces *10*, 37188–37197.

188. Vardar, G., Bowman, W.J., Lu, Q., Wang, J., Chater, R.J., Aguadero, A., Seibert,

R., Terry, J., Hunt, A., Waluyo, I., et al. (2018). Structure, Chemistry, and Charge Transfer Resistance of the Interface between Li7La3Zr2O12 Electrolyte and LiCoO2 Cathode.

189. Dixit, M.B., Park, J.-S., Kenesei, P., Almer, J., and Hatzell, K.B. (2021). Status and prospect of in situ and operando characterization of solid-state batteries . Energy Environ. Sci.

190. Wu, C., Feng, F., and Xie, Y. (2013). Design of vanadium oxide structures with controllable electrical properties for energy applications. Chem. Soc. Rev. *42*, 5157–5183.

191. Wang, J., Chen-Wiegart, Y.C.K., Eng, C., Shen, Q., and Wang, J. (2016). Visualization of anisotropic-isotropic phase transformation dynamics in battery electrode particles. Nat. Commun. *7*, 1–7.

192. Li, W., Liang, J., Li, M., Adair, K.R., Li, X., Hu, Y., Xiao, Q., Feng, R., Li, R., Zhang, L., et al. (2020). Unraveling the origin of moisture stability of halide solid-state electrolytes by in situ and operando synchrotron X-ray analytical techniques. Chem. Mater. *32*, 7019–7027.

193. Shen, F., Dixit, M.B., Xiao, X., and Hatzell, K.B. (2018). Effect of Pore Connectivity on Li Dendrite Propagation within LLZO Electrolytes Observed with Synchrotron X-ray Tomography. ACS Energy Lett. *3*, 1056–1061.

194. Dietrich, C., Koerver, R., Gaultois, M.W., Kieslich, G., Cibin, G., Janek, J., and Zeier, W.G. (2018). Spectroscopic characterization of lithium thiophosphates by XPS and XAS-a model to help monitor interfacial reactions in all-solid-state batteries. Phys. Chem. Chem. Phys. *20*, 20088–20095.

195. Nomura, Y., Yamamoto, K., Hirayama, T., Ohkawa, M., Igaki, E., Hojo, N., and

Saitoh, K. (2018). Quantitative Operando Visualization of Electrochemical Reactions and Li Ions in All-Solid-State Batteries by STEM-EELS with Hyperspectral Image Analyses. Nano Lett. *18*, 5892–5898.

196. Liu, T., Lin, L., Bi, X., Tian, L., Yang, K., Liu, J., Li, M., Chen, Z., Lu, J., Amine, K., et al. (2019). In situ quantification of interphasial chemistry in Li-ion battery. Nat. Nanotechnol. *14*, 50–56.

197. Sagane, F., Shimokawa, R., Sano, H., Sakaebe, H., and Iriyama, Y. (2013). In-situ scanning electron microscopy observations of Li plating and stripping reactions at the lithium phosphorus oxynitride glass electrolyte/Cu interface. J. Power Sources *225*, 245–250.

198. Madsen, K.E., Bassett, K.L., Ta, K., Sforzo, B.A., Matusik, K.E., Kastengren, A.L., and Gewirth, A.A. (2020). Direct Observation of Interfacial Mechanical Failure in Thiophosphate Solid Electrolytes with Operando X-Ray Tomography. Adv. Mater. Interfaces *7*, 1–12.

199. Yang, X., Hu, Y., Dunlap, N., Wang, X., Huang, S., Su, Z., Sharma, S., Jin, Y., Huang, F., Wang, X., et al. (2020). A Truxenone-based Covalent Organic Framework as an All-Solid-State Lithium-Ion Battery Cathode with High Capacity. Angew. Chemie - Int. Ed. *59*, 20385–20389.

200. Han, B., Zhang, Z., Zou, Y., Xu, K., Xu, G., Wang, H., Meng, H., Deng, Y., Li, J., and Gu, M. (2021). Poor Stability of Li2CO3 in the Solid Electrolyte Interphase of a Lithium-Metal Anode Revealed by Cryo-Electron Microscopy. Adv. Mater. *33*, 1–10.

201. Sun, Y., Liu, N., and Cui, Y. (2016). Promises and challenges of nanomaterials for lithium-based rechargeable batteries. Nat. Energy *1*.

202. Liang, J., Zhang, X., Zeng, X., Yan, M., Yin, Y., Xin, S., Wang, W., Wu, X., Shi, J., Wan, L., et al. (2020). Enabling a Durable Electrochemical Interface via an Artificial Amorphous Cathode Electrolyte Interphase for Hybrid Solid/Liquid Lithium-Metal Batteries. Angew. Chemie *132*, 6647–6651.

203. Zhang, H., Chen, F., Lakuntza, O., Oteo, U., Qiao, L., Martinez-Ibañez, M., Zhu, H., Carrasco, J., Forsyth, M., and Armand, M. (2019). Suppressed Mobility of Negative Charges in Polymer Electrolytes with an Ether-Functionalized Anion. Angew. Chemie *131*, 12198–12203.

204. Lin, D., Liu, Y., and Cui, Y. (2017). Reviving the lithium metal anode for high-energy batteries. Nat. Nanotechnol. *12*, 194–206.

205. Gao, Y., Wang, D., Li, Y.C., Yu, Z., Mallouk, T.E., and Wang, D. (2018). Salt-Based Organic–Inorganic Nanocomposites: Towards A Stable Lithium Metal/Li10GeP2S12 Solid Electrolyte Interface. Angew. Chemie - Int. Ed. *57*, 13608–13612.

206. Huo, H., Chen, Y., Luo, J., Yang, X., Guo, X., and Sun, X. (2019). Rational Design of Hierarchical "Ceramic-in-Polymer" and "Polymer-in-Ceramic" Electrolytes for Dendrite-Free Solid-State Batteries. Adv. Energy Mater. *9*, 1–8.

207. Lu, Z., Li, W., Long, Y., Liang, J., Liang, Q., Wu, S., Tao, Y., Weng, Z., Lv, W., and Yang, Q.H. (2020). Constructing a High-Strength Solid Electrolyte Layer by In Vivo Alloying with Aluminum for an Ultrahigh-Rate Lithium Metal Anode. Adv. Funct. Mater. *30*, 1–9.

208. Shi, Y., Wan, J., Liu, G.X., Zuo, T.T., Song, Y.X., Liu, B., Guo, Y.G., Wen, R., and Wan, L.J. (2020). Interfacial Evolution of Lithium Dendrites and Their Solid Electrolyte Interphase Shells of Quasi-Solid-State Lithium-Metal Batteries.

Angew. Chemie - Int. Ed. *59*, 18120–18125.

209. Lopez, J., Mackanic, D.G., Cui, Y., and Bao, Z. (2019). Designing polymers for advanced battery chemistries. Nat. Rev. Mater. *4*, 312–330.

210. Manthiram, A., Yu, X., and Wang, S. (2017). Lithium battery chemistries enabled by solid-state electrolytes. Nat. Rev. Mater. *2*, 1–16.

211. Zheng, Y., Yao, Y., Ou, J., Li, M., Luo, D., Dou, H., Li, Z., Amine, K., Yu, A., and Chen, Z. (2020). A review of composite solid-state electrolytes for lithium batteries: Fundamentals, key materials and advanced structures. Chem. Soc. Rev. *49*, 8790–8839.

212. Zhou, D., Tkacheva, A., Tang, X., Sun, B., Shanmukaraj, D., Li, P., Zhang, F., Armand, M., and Wang, G. (2019). Stable Conversion Chemistry-Based Lithium Metal Batteries Enabled by Hierarchical Multifunctional Polymer Electrolytes with Near-Single Ion Conduction. Angew. Chemie - Int. Ed. *58*, 6001–6006.

213. Yan, Y., Ju, J., Dong, S., Wang, Y., Huang, L., Cui, L., Jiang, F., Wang, Q., Zhang, Y., and Cui, G. (2021). In Situ Polymerization Permeated Three-Dimensional Li+-Percolated Porous Oxide Ceramic Framework Boosting All Solid-State Lithium Metal Battery. Adv. Sci. *8*, 1–9.

214. Mackanic, D.G., Yan, X., Zhang, Q., Matsuhisa, N., Yu, Z., Jiang, Y., Manika, T., Lopez, J., Yan, H., Liu, K., et al. (2019). Decoupling of mechanical properties and ionic conductivity in supramolecular lithium ion conductors. Nat. Commun. *10*, 1–11.

215. Zhao, Q., Liu, X., Stalin, S., Khan, K., and Archer, L.A. (2019). Solid-state polymer electrolytes with in-built fast interfacial transport for secondary lithium batteries. Nat. Energy *4*, 365–373.

216. Chintapalli, M., Chen, X.C., Thelen, J.L., Teran, A.A., Wang, X., Garetz, B.A., and Balsara, N.P. (2014). Effect of grain size on the ionic conductivity of a block copolymer electrolyte. Macromolecules *47*, 5424–5431.

217. Thelen, J.L., Wang, A.A., Chen, X.C., Jiang, X., Schaible, E., and Balsara, N.P. (2018). Correlations between Salt-Induced Crystallization, Morphology, Segmental Dynamics, and Conductivity in Amorphous Block Copolymer Electrolytes. Macromolecules *51*, 1733–1740.

218. Cheng, S., Smith, D.M., and Li, C.Y. (2015). Anisotropic Ion Transport in a Poly(ethylene oxide)-LiClO4 Solid State Electrolyte Templated by Graphene Oxide. Macromolecules *48*, 4503–4510.

219. Yang, C., Wu, Q., Xie, W., Zhang, X., Brozena, A., Zheng, J., Garaga, M.N., Ko, B.H., Mao, Y., He, S., et al. (2021). Copper-coordinated cellulose ion conductors for solid-state batteries. Nature *598*, 590–596.

220. Maitra, A., and Heuer, A. (2007). Cation transport in polymer electrolytes: A microscopic approach. Phys. Rev. Lett. *98*, 1–4.

221. Sharon, D., Bennington, P., Webb, M.A., Deng, C., De Pablo, J.J., Patel, S.N., and Nealey, P.F. (2021). Molecular Level Differences in Ionic Solvation and Transport Behavior in Ethylene Oxide-Based Homopolymer and Block Copolymer Electrolytes. J. Am. Chem. Soc. *143*, 3180–3190.

222. Lopez, J., Sun, Y., Mackanic, D.G., Lee, M., Foudeh, A.M., Song, M.S., Cui, Y., and Bao, Z. (2018). A Dual-Crosslinking Design for Resilient Lithium-Ion Conductors. Adv. Mater. *30*, 1–9.

223. Zeng, Z., Chen, X., Sun, M., Jiang, Z., Hu, W., Yu, C., Cheng, S., and Xie, J. (2021). Nanophase-Separated, Elastic Epoxy Composite Thin Film as an

Electrolyte for Stable Lithium Metal Batteries. Nano Lett. *21*, 3611–3618.

224. Li, Y., Xin, Q., Wu, H., Guo, R., Tian, Z., Liu, Y., Wang, S., He, G., Pan, F., and Jiang, Z. (2014). Efficient CO2 capture by humidified polymer electrolyte membranes with tunable water state. Energy Environ. Sci. *7*, 1489–1499.

225. Chintapalli, M., Le, T.N.P., Venkatesan, N.R., Mackay, N.G., Rojas, A.A., Thelen, J.L., Chen, X.C., Devaux, D., and Balsara, N.P. (2016). Structure and Ionic Conductivity of Polystyrene-block-poly(ethylene oxide) Electrolytes in the High Salt Concentration Limit. Macromolecules *49*, 1770–1780.

226. Young, W.S., and Epps, T.H. (2012). Ionic conductivities of block copolymer electrolytes with various conducting pathways: Sample preparation and processing considerations. Macromolecules *45*, 4689–4697.

227. He, G., Li, Z., Zhao, J., Wang, S., Wu, H., Guiver, M.D., and Jiang, Z. (2015). Nanostructured ion-exchange membranes for fuel cells: Recent advances and perspectives. Adv. Mater. *27*, 5280–5295.

228. Xu, Y.Z., Sun, W.X., Li, W.H., Hu, X.B., Zhou, H.B., Weng, S.F., Zhang, F., Zhang, X.X., Wu, J.G., Xu, D.F., et al. (2000). Investigation on the interaction between polyamide and lithium salts. J. Appl. Polym. Sci. *77*, 2685–2690.

229. Zhao, Z., Li, F., Zhao, J., Ding, G., Wang, J., Du, X., Zhou, Q., Hou, G., and Cui, G. (2020). Ionic-Association-Assisted Viscoelastic Nylon Electrolytes Enable Synchronously Coupled Interface for Solid Batteries. Adv. Funct. Mater. *30*, 1–10.

230. Bar, N., Basak, P., and Tsur, Y. (2017). Vibrational and impedance spectroscopic analyses of semi-interpenetrating polymer networks as solid polymer electrolytes. Phys. Chem. Chem. Phys. *19*, 14615–14624.

231. Wieczorek, W., Raducha, D., Zalewska, A., and Stevens, J.R. (1998). Effect of salt concentration on the conductivity of PEO-based composite polymeric electrolytes. J. Phys. Chem. B *102*, 8725–8731.

232. Chen, H., Tu, H., Hu, C., Liu, Y., Dong, D., Sun, Y., Dai, Y., Wang, S., Qian, H., Lin, Z., et al. (2018). Cationic Covalent Organic Framework Nanosheets for Fast Li-Ion Conduction. J. Am. Chem. Soc. *140*, 896–899.

233. Zhang, K., Liu, W., Gao, Y., Wang, X., Chen, Z., Ning, R., Yu, W., Li, R., Li, L., Li, X., et al. (2021). A High-Performance Lithium Metal Battery with Ion-Selective Nanofluidic Transport in a Conjugated Microporous Polymer Protective Layer. Adv. Mater. *33*, 1–9.

234. Xu, B., Li, X., Yang, C., Li, Y., Grundish, N.S., Chien, P.H., Dong, K., Manke, I., Fang, R., Wu, N., et al. (2021). Interfacial Chemistry Enables Stable Cycling of All-Solid-State Li Metal Batteries at High Current Densities. J. Am. Chem. Soc. *143*, 6542–6550.

235. Fang, R., Xu, B., Grundish, N.S., Xia, Y., Li, Y., Lu, C., Liu, Y., Wu, N., and Goodenough, J.B. (2021). Li2S6-Integrated PEO-Based Polymer Electrolytes for All-Solid-State Lithium-Metal Batteries. Angew. Chemie - Int. Ed. *60*, 17701–17706.

Appendix

Supporting Information

Experimental Section

Materials and Fabrication

The Pebax heterogeneous nanodomain electrolytes (HNEs) were fabricated by first dissolving Pebax (Arkema) and Lithium bis(trifluoromethanesulfonyl)imide (LiTFSI) (Aladdin 99%) in mixed solvents of ethanol and water at 80 ℃. After that, the obtained solution was cast onto a PTFE dish and dried at room temperature for 24 h, followed by vacuum drying at 60 °C (24 h), 90 °C (24 h), and 120 °C (24 h) to evaporate the solvent. The Pebax HNEs with different LiTFSI contents (EO: Li=18:1/16:1/14:1/12:1/10:1/8:1) were prepared and donated as Pebax HNE (X), where X represents 18, 16, 14, 12, 10, and 8 respectively.

The polyethylene oxide (PEO, M_w=600000, Aladdin) electrolyte membrane was prepared by dissolving PEO and LiTFSI (EO: Li = 12:1) in anhydrous acetonitrile. The resultant solution was then cast onto a PTFE dish in an argon filled glove box. The PEO electrolyte membrane was dried at 30 °C for 24 h and followed by vacuum drying at 50 °C.

Lithium metal was purchased from China Energy Lithium Co., Ltd. with a diameter of 16 mm and thickness of 500 um, which was used without further pretreatment.

To prepare the $LiFePO_4$ (LFP) and $LiNi_{0.8}Mn_{0.1}Co_{0.1}O_2$ (NCM 811) electrodes: LFP or NCM 811, polyvinylidene fluoride (PVDF), and carbon black with a weight ratio of 80:10:10 were mixed in N-methyl-2-pyrrolidone (NMP) to form a homogeneous slurry. The slurry was mechanically stirred for 1 h and then cast on the carbon–coated aluminum foil. The cathode was further dried at 80 °C for 24 h under vacuum. The loading of electrodes active material is (3-7.1) mg cm^{-2}, where the low loading is (3-4) mg cm^{-2} and the high loading is 7.1 mg cm^{-2}.

The as-prepared electrolyte membranes and electrodes were further stored in an argon filled glove box (H_2O < 1 ppm and O_2 < 1 ppm) to eliminate the adverse influence of water or solvent completely before use.

Structure and morphology characterization

The microphase separation structure of electrolyte membranes were characterized by small-angle X-ray scattering (SAXS) (Xenocs Xeuss 3.0) with a scan range of 0.07–3.8 nm^{-1}. The Pebax HNEs nanodomains spacing, L_0, is calculated by as $2\pi/q$, where q represents the scattering peaks. X-ray diffraction (XRD) was recorded by Brucker AXS D8 at a range of 5°~50° with Cu Kα radiation (λ=1.5406 Å). Differential scanning calorimetry (DSC) was collected by NETZSCH DSC 200F3 at 10 °C/min from -80~250 °C with N_2 atmosphere.

Mechanical testing was carried out on an Instron electroplus 1000 testing stain with a strain rate of 2 mm/min. The morphology and microstructure of electrolyte membranes were characterized by scanning electron microscope (SEM) (JEOL 7001F) equipped with an energy-dispersive microscopy EDX spectrometer. Flourier transform infrared spectra (FT-IR) were recorded from 500-4000 cm^{-1} *via* a Thermo Scientific Nicolet iS50 instrument. Solid-state nuclear magnetic resonance (NMR) experiments were conducted using an JNM-ECZ 600 MHz NMR spectrometer at room temperature. Spin–lattice relaxation time (T_1) was measured employing a saturation recovery pulse sequence with 15 saturation pulses at recovery times varying from 0 to 20.0 s.

The cells were imaged using the non–destructive synchrotron X–ray tomography technique conducted at the tomography station at BMIT-BM line end station at BESSY II, Helmholtz–Zentrum Berlin, Canadian Light Sources, which makes it possible to directly visualize the three-dimensional electrode. Monochromatic hard X–rays with an energy of 20 keV ($\Delta E/E = 1.5\%$) were directed onto the sample. The transmitted X–rays were converted into the visible light by a scintillator (CdWO 4, 60 μm in thickness), which were then magnified by a set of microscope optics before projected on a CCD sensor (PCO4000 camera, 4008 × 2672 pixel). A (4.4 × 2.9) mm^2 field of view was used with a pixel size of 0.72 μm. During a rotation of 180°, 2200 projections and 230 flatfields with an exposure time of 1.6 s for each projection/flat field were collected. The 3D image reconstruction followed the same procedure as our previous report. Image segmentation

was conducted using Image J/Weka followed by the visualization *via* VGSTUDIO MAX 3.1. All the symmetrical Li/polymer/Li cells were galvanostatic discharged (stripping) and charged (plating) using a Neware BTS400 multichannel battery testing system. After cycling, the cells were transferred to the beamline to conduct tomography without cell disassembly.

X–ray photoelectron spectroscopy (XPS, Thermo Scientific ESCALAB Xi^+) was acquired by utilizing an Al K α (λ = 0.83 nm, hν = 1,486.7 eV) X–ray source operated at 2 kV and 20 mA (**Note:** The cycled Li metal was first washed by Propylene carbonate and then measured to obtain the surface information). The C 1s main peak at 284.6 eV was treated as the reference to calibrate peak shifts caused by the surface–charging effects. Time–of–flight secondary ion mass spectrometry (TOF–SIMS5-100) was employed to study the surface chemical composition of Li anode. For depth profiling, a Cs^+ ion beam (1KeV ion energy, ~40 nA measured sample current) was used to sputter 50×80 μm^2 areas centered around the analyzed areas. All depth profiles were acquired in noninterlaced mode, namely sequential sputtering, and analyzed.

Electrochemical measurements

All electrochemical measurements were carried out using a Bio-Logic electrochemical station. Electrochemical impedance spectroscopy (EIS) measurements were tested in a sandwiched Li ion blocking stainless steel electrodes in the frequency range of 1 MHz to 0.1 Hz with an AC amplitude of 10 mV under the temperature range from 30 °C to 90 °C. The linear sweep voltammetry was determined employing a Li |solid electrolyte| stainless steel model from 2.5 to 6 V at a scan rate of 1 mV/s.

All the cells were sealed in a 2032-coin cell for testing. A symmetric cell of Li |solid electrolyte| Li was employed for both interfacial resistance and interface stability of the composite polymer electrolyte against lithium electrode. The galvanostatic cycling was conducted at a current density of 0.1 mA cm^{-2} with charging and discharging for 1 h, respectively. A cell of Li|solid electrolyte|Cu, employed for monitoring the nucleation of Li, was conducted at a current density of 0.1 mA cm^{-2} with charging and discharging for 1 h, respectively.

The cycling and rate performance of all-solid–state batteries were determined on a Neware BTS400 instrument with 2.5-3.95 V (LFP) and 2.8-4.2 V (NCM 811).

Details of Molecular Dynamics Simulations

Classic molecular dynamics simulations were carried out to give an atom-level insight of the microstructure of the Pebax HNE (12) and PEO systems. The diffusion behavior of Li^+ in two systems was also studied. The molecular/polymer structures of LiTFSI, Pebax, and PEO are shown in the Supplementary Fig. 1. The simplified Pebax chain features 24 ethylene oxide units followed by 6 polyamide units while the simplified PEO chain contains 24 ethylene oxide units. The component and amount of the simulation system are listed in Supplementary Table 1. Both the initial configurations of mixture systems were constructed through the software of PACKMOL,[1] all the molecules were randomly inserted in a cubic simulation box. The GROMOS54a7 force field[2] was employed to describe the behavior of the molecules. The molecular force field consists of nonbonded and bonded interaction. The nonbonded interaction contains van deer Waals (vdW) and electrostatic interaction, which are described by the Equation 1 and Equation 2, respectively.

$$E_{LJ}\left(r_{ij}\right)=4\varepsilon_{ij}\left(\left(\frac{\varepsilon_{ij}}{r_{ij}}\right)^{12}-\left(\frac{\varepsilon_{ij}}{r_{ij}}\right)^{6}\right) \tag{1}$$

$$E_{c}\left(r_{ij}\right)=\frac{q_i q_j}{4\pi\varepsilon_o\varepsilon_r r_{ij}} \tag{2}$$

For different kinds of atoms, the Lorentz-Berthelot mix rules were adopted for vdW interactions, which follows the Equation 3. The cut-off distance of vdW and electronic interactions was set to 1.2 nm, and the particle mesh Ewald (PME) method was employed to calculate long-range electrostatic interactions.

$$\sigma_{ij}=\frac{1}{2}\left(\sigma_{ii}+\sigma_{jj}\right);\varepsilon_{ij}=\left(\varepsilon_{ii}*\varepsilon_{jj}\right)^{1/2} \tag{3}$$

Results and Discussion

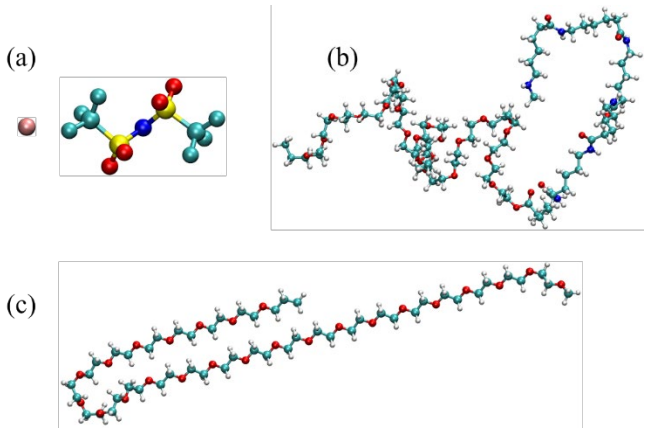

Figure S1. The molecular structure of a) LiTFSI, b) Pebax, and c) PEO.

Table S1. The initial configuration setup for the simulation system.

System	Type	Number
PEO	Li^+	50
	$TFSI^-$	50
	PEO	25
Pebax HNE (12)	Li^+	50
	$TFSI^-$	50
	Pebax	25

An energy minimization was firstly employed to relax the simulation box. Then, an isothermal-isobaric (NPT) ensemble with a 1.0 fs time step was employed to optimize the simulation box. The pressure of both systems was set to 1.0 atm, which was kept via the Parrinello-Rahman barostat. The temperature was set to 298.15 K, which was kept via the Nose-Hoover thermostat barostat. The NPT optimization time was set to 20.0 ns, which is long enough to obtain a stable box size. Following the NPT simulation, a canonical (NVT) ensemble with 20.0 ns was performed to further optimize the simulation box, the time step was set to 2.0 fs. At last, another 10.0 ns NVT simulation was performed to collect the trajectory coordinates of molecules with a storage frequency of 100 steps. The time step of NVT simulation was set to 1.0 fs. For all the MD simulations, the motion of atoms was described by classical Newton's equation, which was solved using the Velocity-Verlet algorithm. Diffusion coefficients of Li^+ and $TFSI^-$ ions were calculated based on the mean–squared displacement (MSD). All simulations were performed using the GROMACS 2019.5 package.[3]

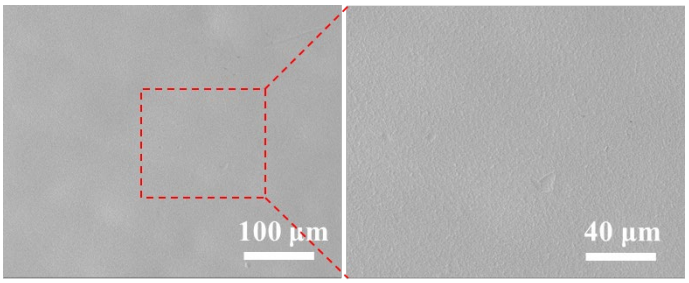

Figure S2. Surface SEM images of Pebax HNEs.

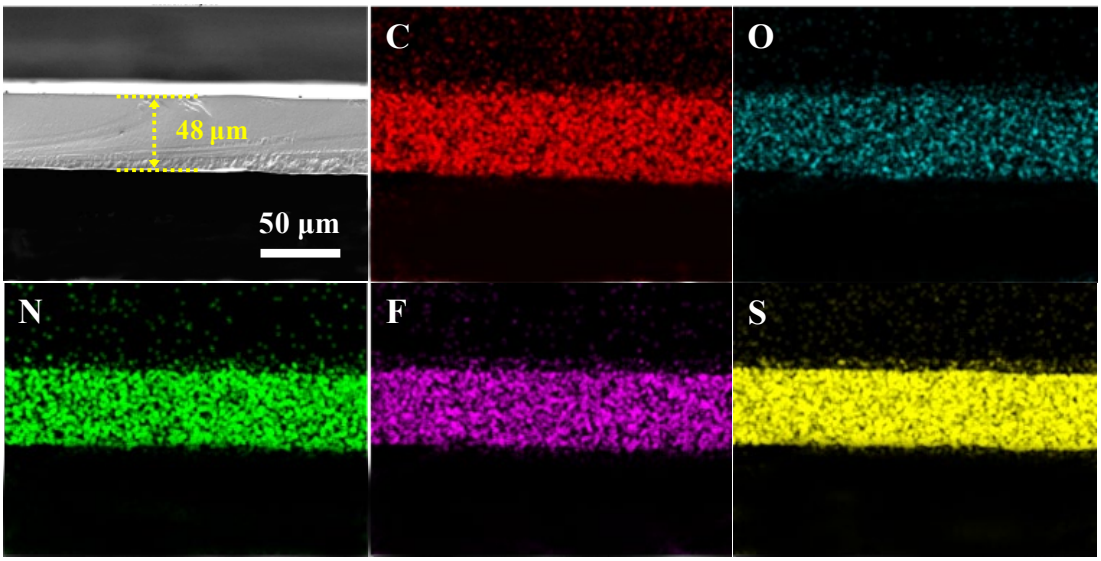

Figure S3. Cross-section image and corresponding EDX mapping of Pebax HNEs.

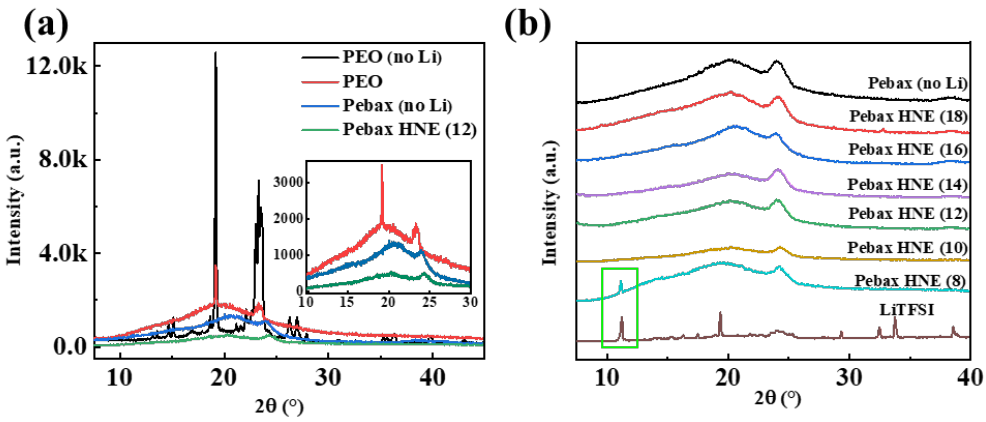

Figure S4. XRD patterns of a) PEO and Pebax membranes as well as b) Pebax HNEs with different EO: Li ratio.

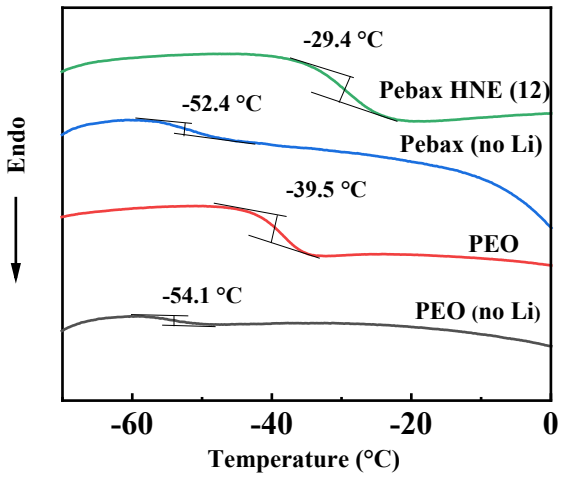

Figure S5. DSC curves of PEO and Pebax membranes at low-temperature zone (-80-0 °C).

Table S2. The physiochemical data for the phase behavior of PEO and Pebax membranes.

Sample	PEO			PA	
	T_g(°C)	T_m(°C)	X_c(%)	T_m(°C)	X_c(%)
PEO (no Li)	-54.1	65.7	98.7	-	-
PEO	-39.5	52.3	62.3	-	-
Pebax (no Li)	-52.4	16.6	49.4	206.5	65.1
Pebax HNE (12)	-29.4	-	-	123.8	34.3

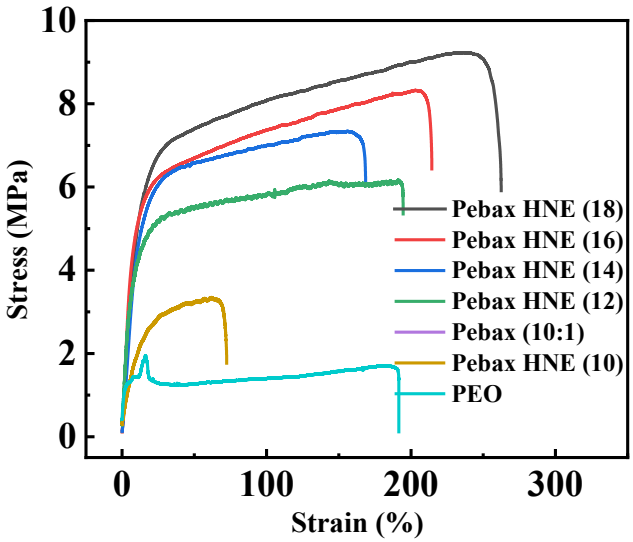

Figure S6. Mechanical properties of Pebax HNEs with different contents of LiTFSI.

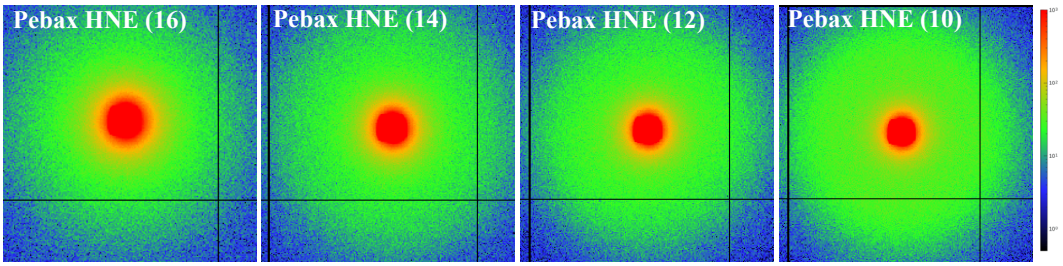

Figure S7. 2D-SAXS patterns of Pebax HNEs.

Table S3. Nanodomain of Pebax HNEs was measured and calculated by SAXS.

Smaple	q (nm^{-1})	L_o (nm)
Pebax HNE (16)	0.477	13.17
Pebax HNE (14)	0.511	12.29
Pebax HNE (12)	0.485	12.95
Pebax HNE (10)	0.499	12.59

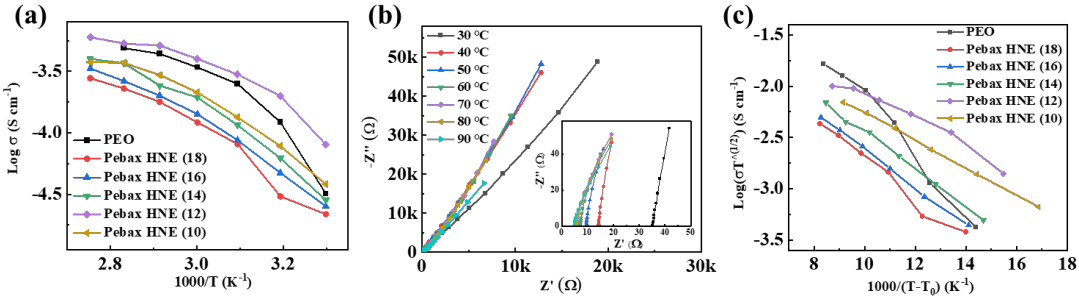

Figure S8. a) Arrhenius plots of PEO and Pebax HNEs and b) EIS spectra of Pebax HNE (12) at different temperature. c) Vogel-Tammann-Fulcher (VTF) plots of PEO and Pebax HNEs.

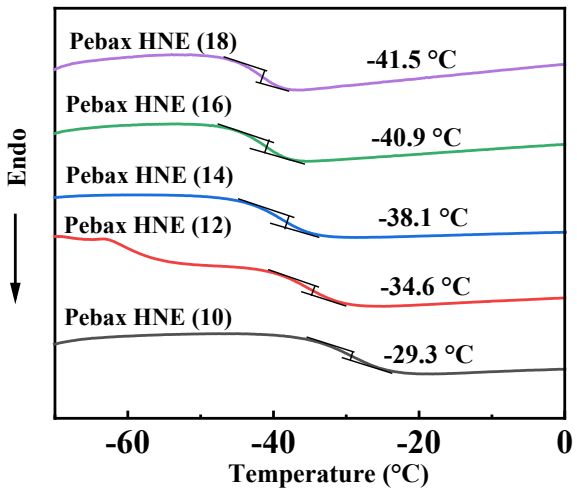

Figure S9. DSC curves of Pebax HNEs at low-temperature zone (-80-0 °C).

Table S4. Activation energies calculated by different models for PEO and Pebax HNEs.

Sample	Model	E_a/eV	Model	E_a/eV
PEO	VTF	0.279	Arrhenius	3.01
Pebax HNE (18)		0.196		2.14
Pebax HNE (16)		0.184		2.06
Pebax HNE (14)		0.182		2.11
Pebax HNE (12)		0.126		1.48
Pebax HNE (10)		0.133		1.86

The Arrhenius model ($\sigma(T) = A \exp(-E_a/RT)$) mainly reflects the mechanism of cation jumping nearest vacant sites in crystals, which is not apply to polymer electrolytes.[4] Considering that Li^+ in polymer electrolytes rely on the segmental movements of polymer chains, the Vogel-Tammann-Fulcher (VTF) model is more suitable for this study than Arrhenius model. The VTF equation is $\sigma(T) = AT^{-1/2} \exp(-E_a/R(T-T_0))$.[5] Where A, E_a and T_0 are the conductivity pre-exponential factor, activation energy and glass transition temperature, respectively. In order to compare the ion transport ability in all the electrolytes, the activation energies of these samples calculated *via* two different models are listed in Table S4.

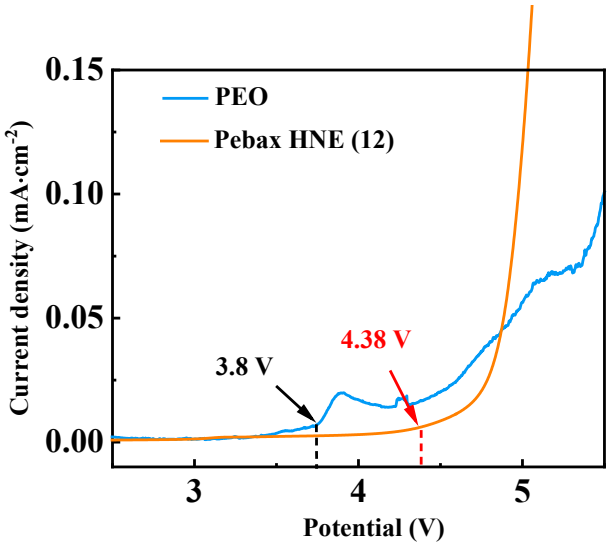

Figure S10. LSV curves of PEO and Pebax HNE (12).

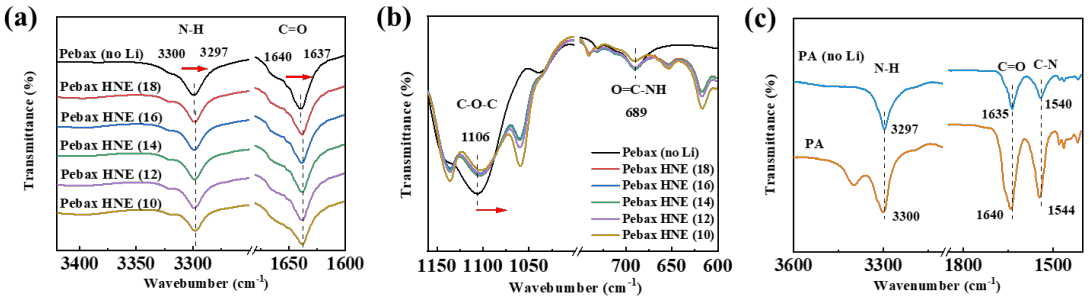

Figure S11. FT-IR spectra of Pebax HNEs, PA (no Li) and PA.

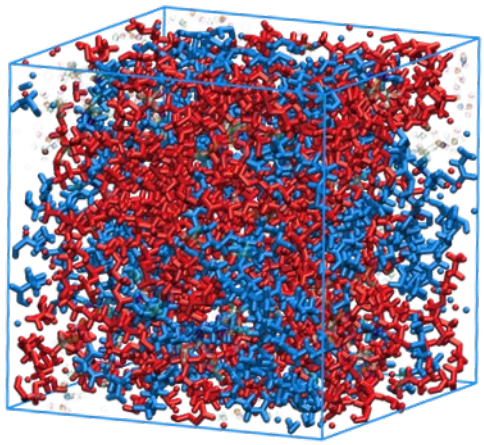

Figure S12. The agglomeration structure in Pebax HNE (12), where PEO chains, PA chains are highlighted by red and blue, respectively.

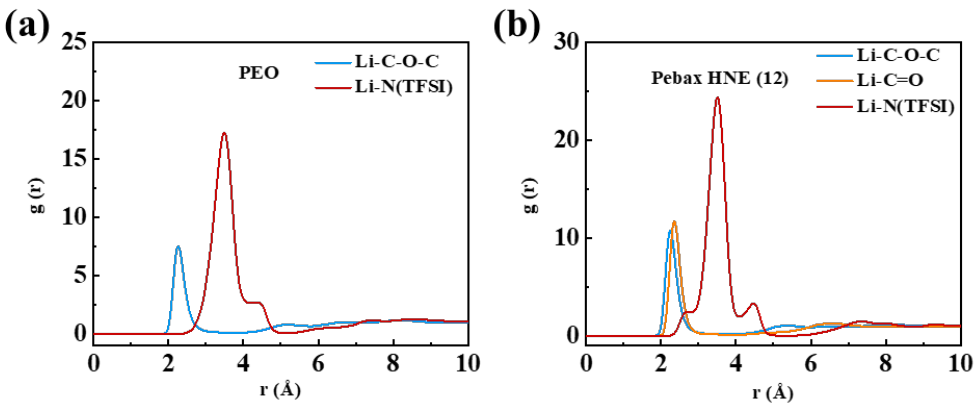

Figure S13. RDF of Li to C-O-C/N(TFSI) in a) PEO and b) Li to C-O-C/C=O/N(TFSI) in Pebax HNE (12).

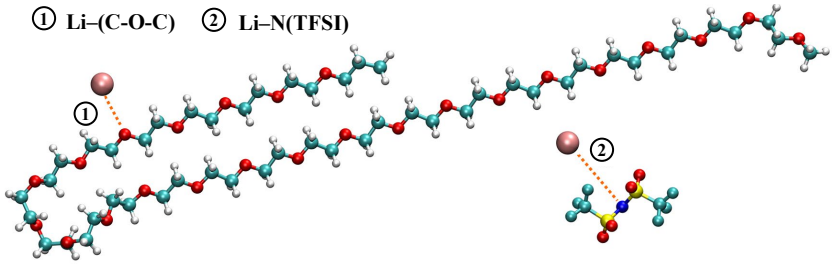

Figure S14. Schematic diagram of the interaction between the various components in PEO electrolyte.

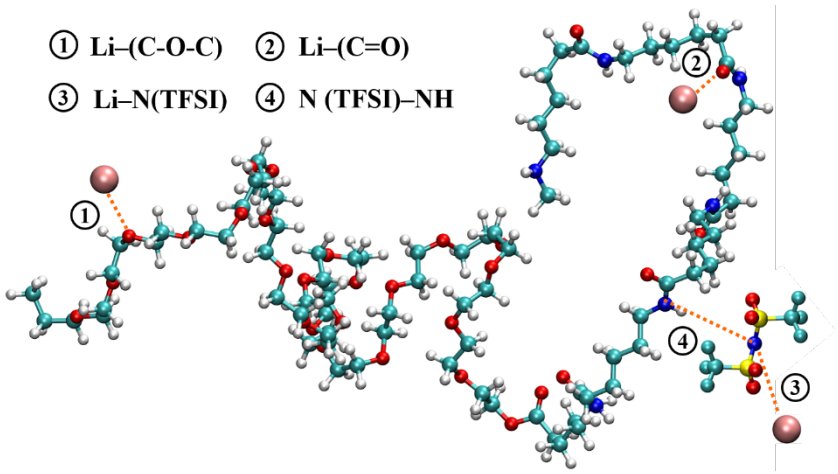

Figure S15. Schematic diagram of the interaction between the various components in Pebax HNEs.

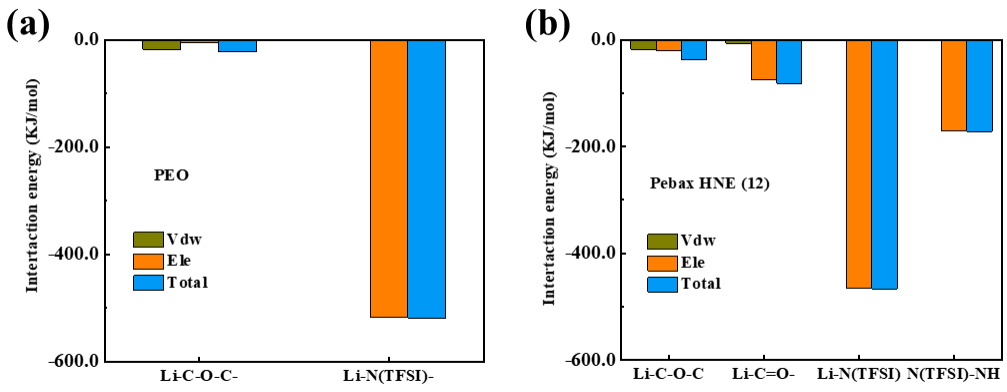

Figure S16. The total interaction energy in a) PEO and b) Pebax HNE (12).

Table S5. Results of the interaction energy between the various components in PEO and Pebax HNE (12).

System	Components		E_{vdw} (kJ/mol)	E_{ele} (kJ/mol)	E_{total} (kJ/mol)
PEO	Li^+	C-O-C	439.6	138.95	578.55
		N ($TFSI^-$)	-16.17	-12933.48	-12949.65
Pebax HNE (12)	Li^+	C-O-C	448.45	499.46	947.91
		C=O	172.82	1872.98	2045.8
		N($TFSI^-$)	-6.43	-11662.38	-11668.81
	N($TFSI^-$)	NH	-19.86	-4276.85	-4296.71

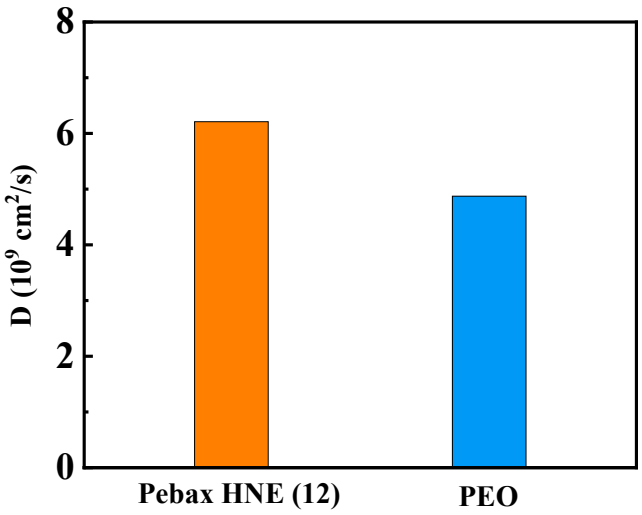

Figure S17. The diffusion coefficients of Li^+ in PEO and Pebax HNE (12).

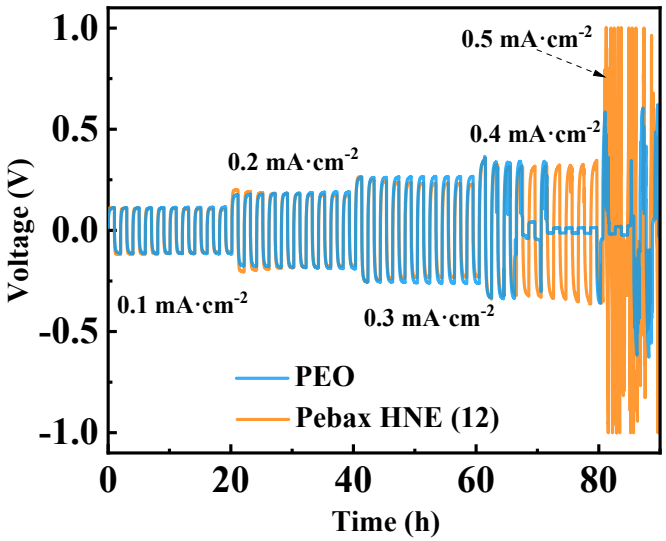

Figure. S18. The galvanostatic cycling profile of the Li/PEO/Li and Li/Pebax HNE (12)/Li cells at various current densities measured at 60 °C. The cells were charged and discharged for 1 h at each current density.

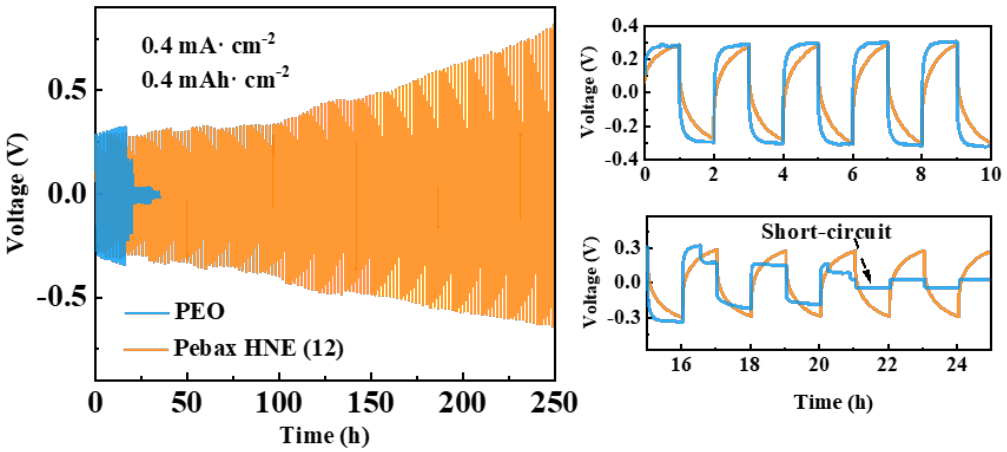

Figure. S19. The long-term cycling performance of symmetric cells at 60 °C.

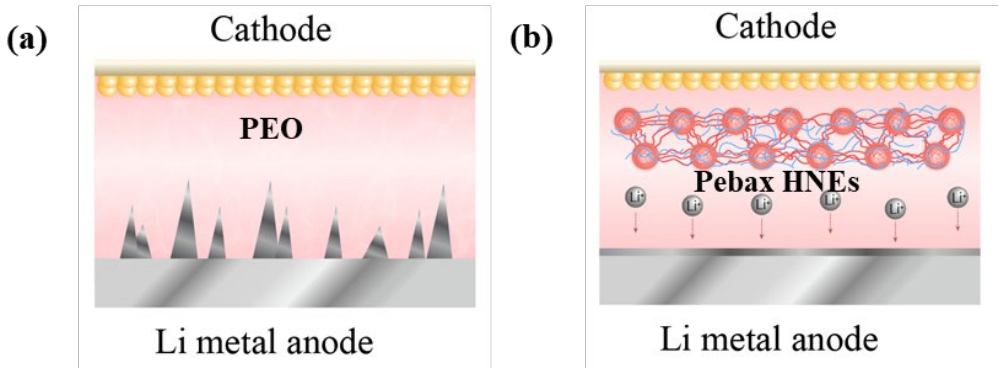

Figure S20. The schematic of Li^+ deposition on Li anode during cycle with the electrolytes of a) PEO and b) Pebax HNE (12).

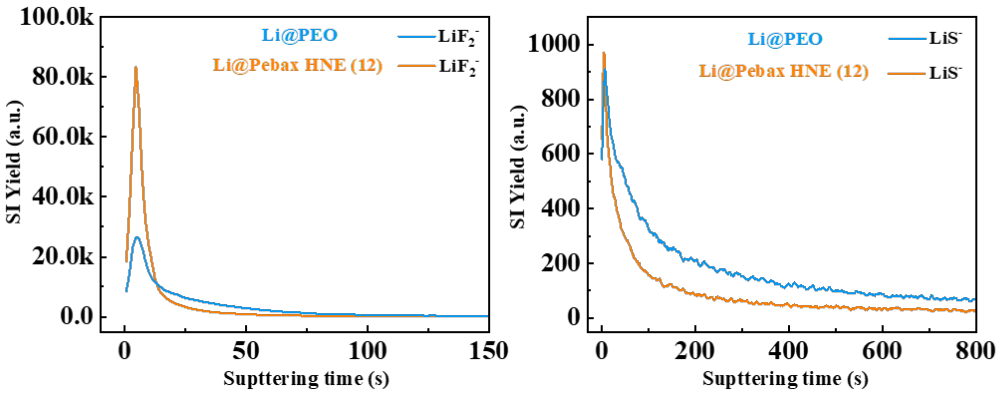

Figure S21. TOF-SIMS depth profiles of the representative species of SEI formed at the Li@PEO and Li@Pebax HNE (12).

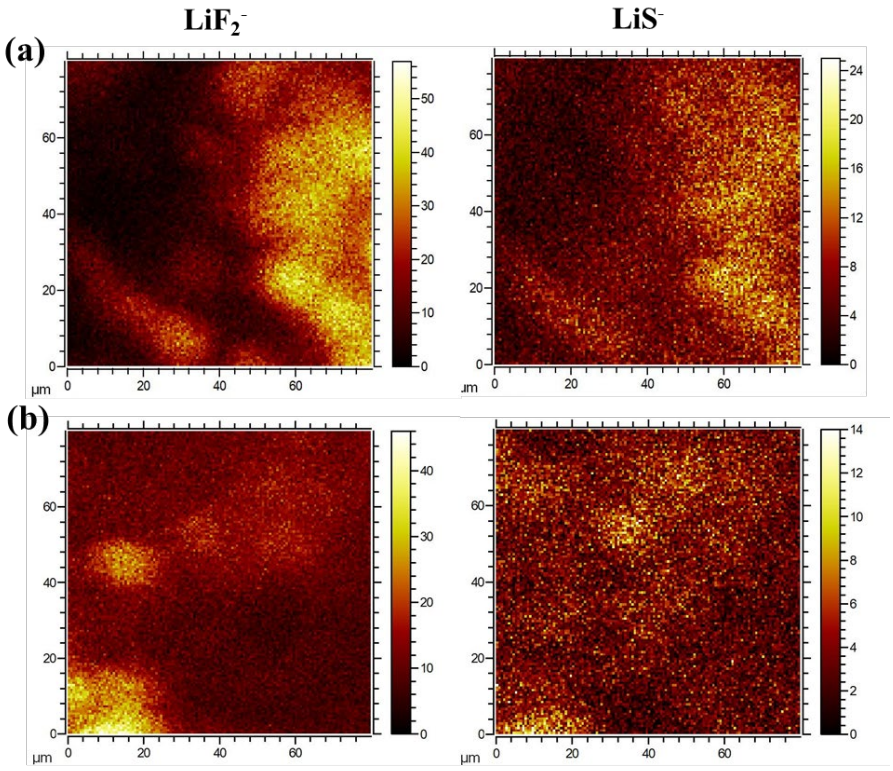

Figure S22. The TOF-SIMS overlays of LiF_2^- and LiS^- at the a) Li@PEO and b) Li@Pebax HNE (12) surface.

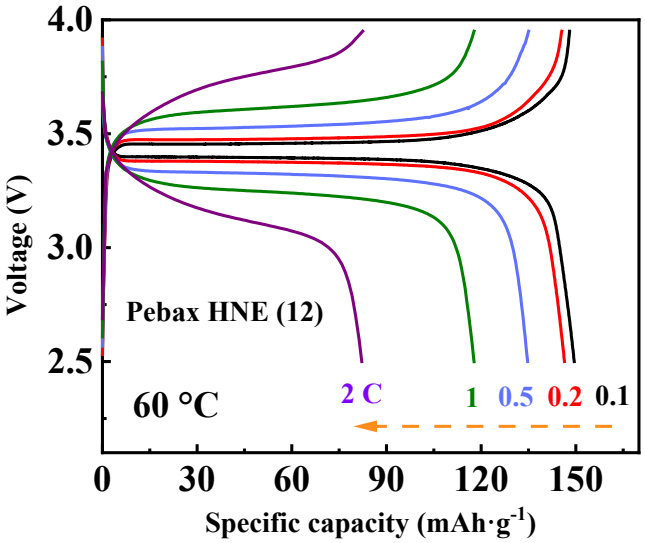

Figure S23. Charge–discharge curves of the Li/Pebax HNE (12)/LFP cell at different rates, cycled at 60 °C.

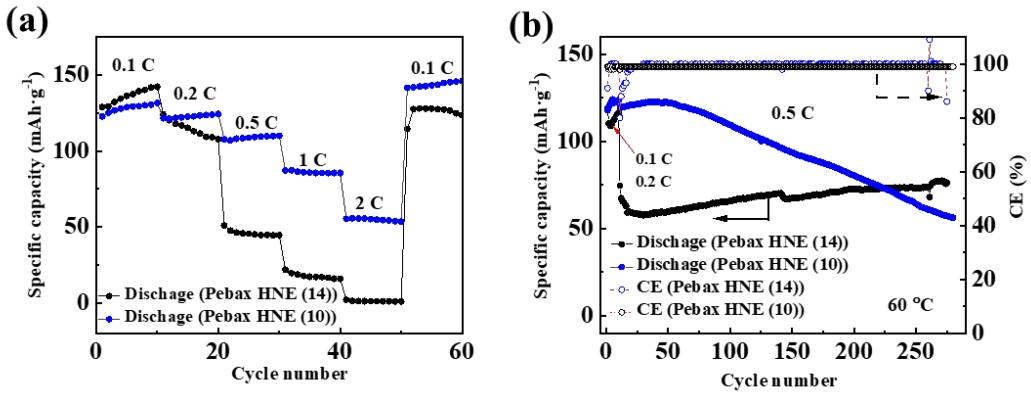

Figure S24. The control cells (Li/Pebax HNE (14/10)/LFP) performance of a) rate and b) long-term cycling, at 0.5 C and 60 °C.

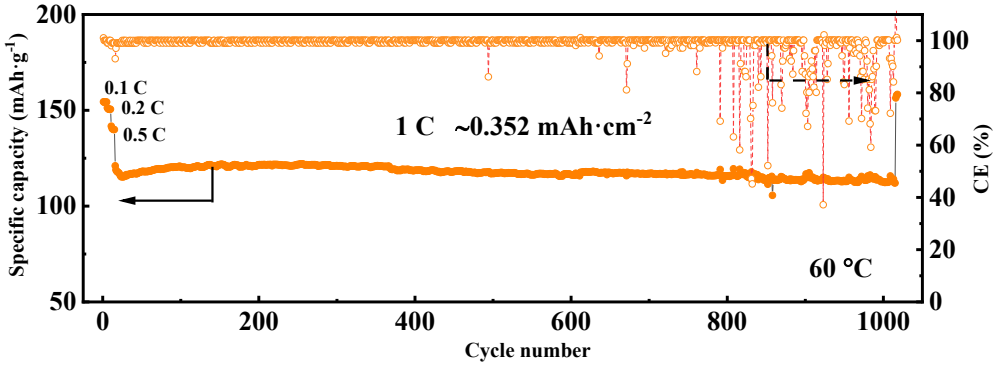

Figure S25. Discharge specific capacity and CE of the Li/Pebax HNE (12)/LFP cell at 1 C, under 60 °C.

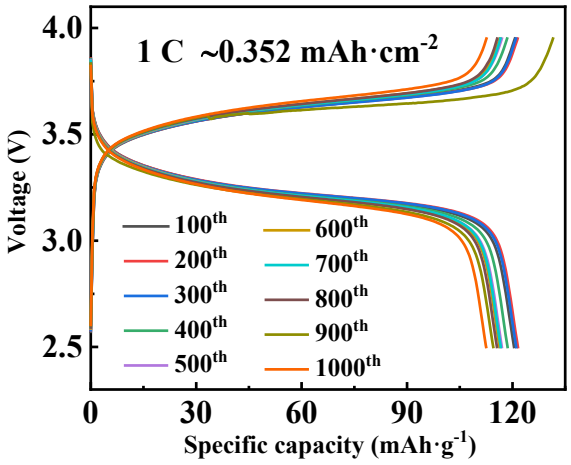

Figure S26. Charge-discharge curves of the Li/Pebax HNE (12)/LFP cell at 1 C, under 60 °C.

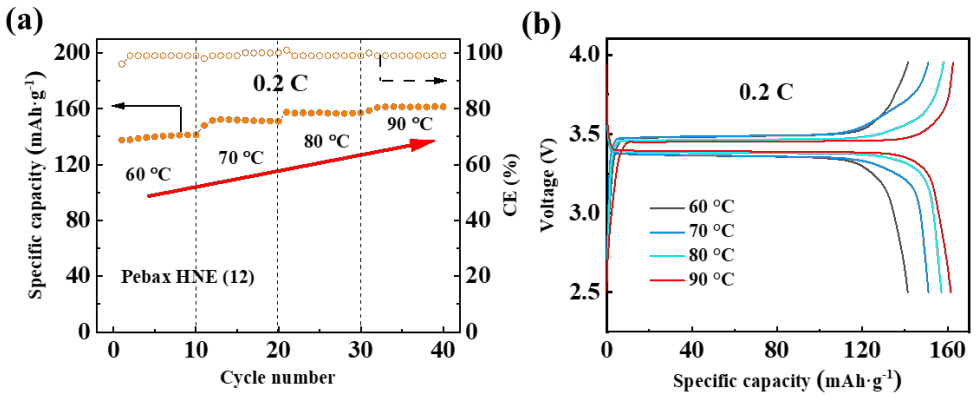

Figure S27. a) Discharge specific capacity and CE as well as b) charge-discharge curves of the Li/Pebax HNE (12)/LFP cell at different temperature.

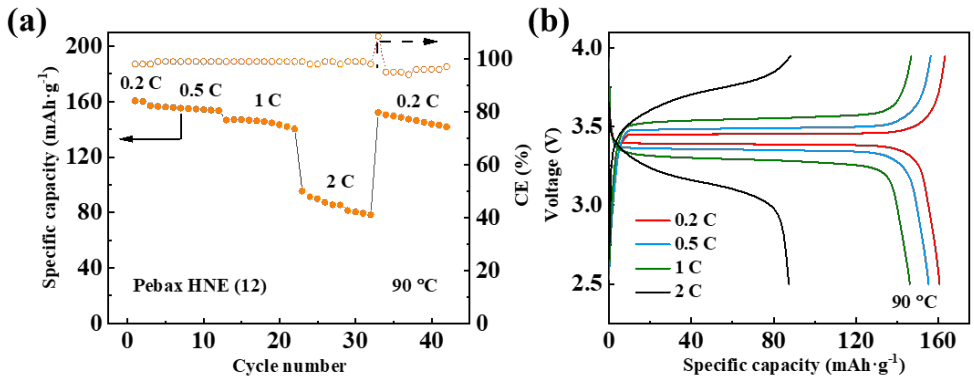

Figure S28. a) Rate performance and b) corresponding charge-discharge curves of the Li/Pebax HNE (12)/LFP cell at 90 ℃.

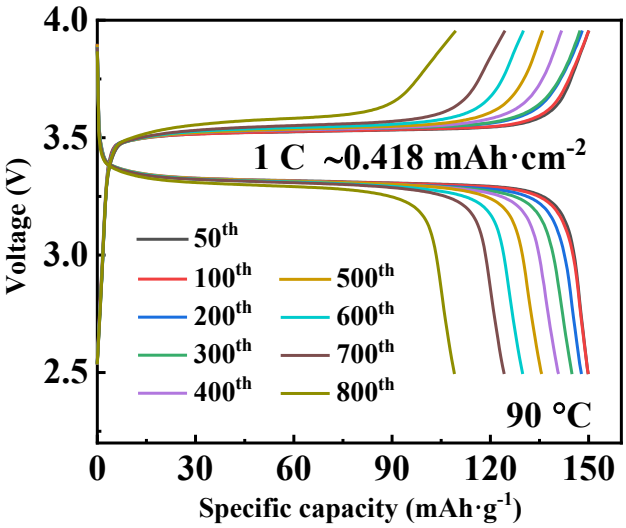

Figure S29. Charge-discharge curves of the Li/Pebax HNE (12)/LFP cell at 1 C, under 90 °C.

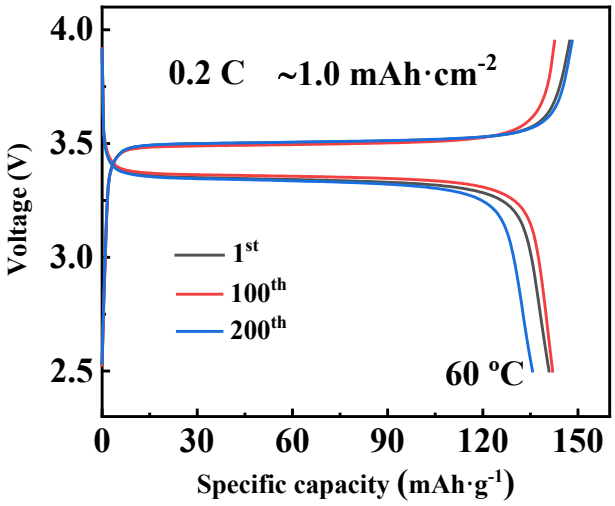

Figure S30. Charge-discharge curves of the Li/Pebax HNE (12)/LFP cell at 0.2 C, under 60 °C.

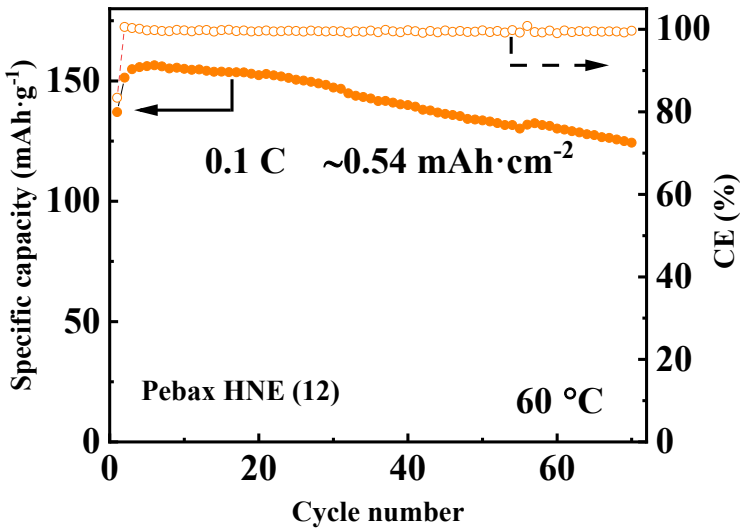

Figure S31. Discharge specific capacity and CE of the Li/Pebax HNE (12)/NCM 811 cells at 0.1 C, under 60 °C.

Type	Component	Cathod/loading ($mg \cdot cm^{-2}$)	Capacity ($Ah \cdot cm^{-2}$)	Cycle number	Rate and capacity retention (%)	References
Polymer	PEO/PFSILi	LFP/-	-	100	0.2C, 82%	[6]
Polymer	P(MPEGA-AMPSLi)/PVDF-HFP	LFP/-	-	100	0.5C, 86.4%	[7]
Polymer	PEO/EG-P[SSPSILi-alt-MA]	LFP/~2.5	0.31	100	0.1C, 97%	[8]
Polymer	PLSSCQD/PEO	LFP/-	-	100	0.2C,94.3%	[9]
Polymer-inorgainc	PEO/LLZTO/LiTFSI	LFP/~4.7	0.71	100	0.1C, 87%	[10]
Polymer-inorgainc	PEO/LLZO nanowire/ LiTFSI	LFP/~1.68	0.27	120	0.1C, 91.7%	[11]
Polymer-organic	DMA@LiTFSI mediated COF	LFP/~2.5	0.3	130	0.1C, 90.2%	[12]
Polymer-inorgainc	PEO/h-BN/LiTFSI	LFP/~1.25	0.18	140	0.2C, 93%	[13]
Polymer-inorgainc	PEO-PEG/LGPS/LiTFSI	LFP/-	-	150	0.5C, 91%	[14]
Polymer-inorgainc	PEO/LAGP/LiTFSI	LFP/-	0.92	150	0.3C, 93.3%	[15]
Polymer-inorgainc	PEO/LLZTO-HT/LiTFSI	LFP/~6	0.75	200	0.1C, 86.1%	[16]
Polymer-inorgainc	PEO/VAVS/LiTFSI	LFP/~0.8	0.13	200	0.5C, 82%	[17]
Polymer-inorgainc	PEO/Ca–CeO2/LiTFSI	LFP/-	-	200	1C, 76.9%	[18]
Polymer-	PEO/MnO2-	LFP/~1.3	0.19	300	0.5C,	[19]

inorgainc	nanosheet /LiTFSI				86.7%	
Polymer-inorgainc	PEO/LAGP-nanosheet/LiTFSI	LFP/~4	0.56	300	0.5C, 92%	[20]
Polymer-inorgainc	PEO/LLTO/LiTFSI	LFP/~2	0.23	300	2C, 79%	[21]
Polymer-inorgainc	PEO/LLZO/LiTFSI	LFP/-	-	450	0.2C, 84%	[22]
Polymer-inorgainc	PEO/Li2S6/LiTFSI	LFP/-	0.11	700	0.18C, 89.2%	[23]
Polymer	PEGMEA/PE/LiTDSI	LFP/-	-	1000	1C, 76.4	[24]
Polymer	Pebax/LiTFSI	LFP/~7.1	1.00	200	0.2C, 93%	This work
		LFP/~3	0.42	800	1C, 74.2%	
		LFP/~3.6	0.52	1560	0.5C 80%	

LFP, $LiFePO_4$

Table S6. Comparison of electrochemical performance of the PEO-based all solid-state electrolytes reported in recent publications.

[1] L. Martinez, R. Andrade, E. G. Birgin, J. M. Martinez, *J. Comput. Chem.* **2009**, *30*, 2157-2164.

[2] N. Schmid, A. P. Eichenberger, A. Choutko, S. Riniker, M. Winger, A. E. Mark, W. F. van Gunsteren, *Eur. Biophys. J.* **2011**, *40*, 843-856.

[3] Szil´ard P´all, Mark James Abraham, Carsten Kutzner, Berk Hess, E. Lindahl, *Solving Software Challenges for Exascale*, **2015**.

[4] S. B. Aziz, T. J. Woo, M. F. Z. Kadir, H. M. Ahmed, *J. Sci.: Adv. Mater. Devices* **2018**, *3*, 1-17.

[5] a) J. Lopez, Y. Sun, D. G. Mackanic, M. Lee, A. M. Foudeh, M. S. Song, Y. Cui, Z. Bao, *Adv. Mater.* **2018**, *30*, e1804142; b) K. He, S. H. Cheng, J. Hu, Y. Zhang, H. Yang, Y. Liu, W. Liao, D. Chen, C. Liao, X. Cheng, Z. Lu, J. He, J. Tang, R. K. Y. Li, C. Liu, *Angew. Chem. Int. Ed.* **2021**, *60*, 12116-12123.

[6] Q. Shi, L. Xue, D. Qin, B. Du, J. Wang, L. Chen, *J. Mater. Chem. A* **2014**, *2*, 15952-15957.

[7] X. Shen, H. Hua, H. Li, R. Li, T. Hu, D. Wu, P. Zhang, J. Zhao, *Polymer* **2020**, *201*, 122568.

[8] C. Cao, Y. Li, S. Chen, C. Peng, Z. Li, L. Tang, Y. Feng, W. Feng, *ACS Appl. Mater. Interfaces* **2019**, *11*, 35683-35692.

[9] C. Z. Zhao, X. Q. Zhang, X. B. Cheng, R. Zhang, R. Xu, P. Y. Chen, H. J. Peng, J. Q. Huang, Q. Zhang, *Proc. Natl. Acad. Sci.* **2017**, *114*, 11069-11074.

[10] Z. Li, F. Liu, S. Chen, F. Zhai, Y. Li, Y. Feng, W. Feng, *Nano Energy* **2021**, *82*, 105698.

[11] Z. Wan, D. Lei, W. Yang, C. Liu, K. Shi, X. Hao, L. Shen, W. Lv, B. Li, Q. Yang, F. Kang, Y. He, *Adv. Funct. Mater.* **2019**, *29*, 1805301.

[12] D. Guo, D. B. Shinde, W. Shin, E. Abou-Hamad, A. H. Emwas, Z. Lai, A. Manthiram, *Adv Mater* **2022**, e2201410.

[13] Y. Li, L. Zhang, Z. Sun, G. Gao, S. Lu, M. Zhu, Y. Zhang, Z. Jia, C. Xiao, H. Bu, K. Xi, S. Ding, *J. Mater. Chem. A* **2020**, *8*, 9579-9589.

[14] K. Pan, L. Zhang, W. Qian, X. Wu, K. Dong, H. Zhang, S. Zhang, *Adv. Mater.* **2020**, *32*, e2000399.

[15] X. Wang, H. Zhai, B. Qie, Q. Cheng, A. Li, J. Borovilas, B. Xu, C. Shi, T. Jin, X. Liao, Y. Li, X. He, S. Du, Y. Fu, M. Dontigny, K. Zaghib, Y. Yang, *Nano Energy* **2019**, *60*, 205-212.

[16] H. Huo, X. Li, Y. Sun, X. Lin, K. Doyle Davis, J. Liang, X. Gao, R. Li, H. Huang, X. Guo, X. Sun, *Nano Energy* **2020**, *73*, 104836.

[17] W. Tang, S. Tang, X. Guan, X. Zhang, Q. Xiang, J. Luo, *Adv. Funct. Mater.* **2019**, *29*, 1900648.

[18] H. Chen, D. Adekoya, L. Hencz, J. Ma, S. Chen, C. Yan, H. Zhao, G. Cui, S. Zhang, *Adv. Energy Mater.* **2020**, *10*, 2000049.

[19] Y. Li, Z. Sun, D. Liu, Y. Gao, Y. Wang, H. Bu, M. Li, Y. Zhang, G. Gao, S. Ding, *J. Mater. Chem. A* **2020**, *8*, 2021-2032.

[20] A. Li, X. Liao, H. Zhang, L. Shi, P. Wang, Q. Cheng, J. Borovilas, Z. Li, W. Huang, Z. Fu, M. Dontigny, K. Zaghib, K. Myers, X. Chuan, X. Chen, Y. Yang, *Adv. Mater.* **2020**, *32*, e1905517.

[21] K. Liu, R. Zhang, J. Sun, M. Wu, T. Zhao, *ACS Appl. Mater. Interfaces* **2019**, *11*, 46930-46937.

[22] Z. Guo, Y. Pang, S. Xia, F. Xu, J. Yang, L. Sun, S. Zheng, *Adv. Sci.* **2021**, *8*, e2100899.

[23] R. Fang, B. Xu, N. S. Grundish, Y. Xia, Y. Li, C. Lu, Y. Liu, N. Wu, J. B. Goodenough, *Angew. Chem. Int. Ed.* **2021**, *60*, 17701-17706.

[24] Z. Wang, L. Shen, S. Deng, P. Cui, X. Yao, *Adv. Mater.* **2021**, *33*, e2100353.